UNIVERSITY OF OKLAHOMA

GRADUATE COLLEGE

AN ULTRAVIOLET SURVEY OF THE DA WHITE DWARF POPULATION OF THE GALAXY

A DISSERTATION

SUBMITTED TO THE GRADUATE FACULTY

in partial fulfillment of the requirements for the

Degree of

DOCTOR OF PHILOSOPHY

By

RENAE E. WALL
Norman, Oklahoma
2023

AN ULTRAVIOLET SURVEY OF THE DA WHITE DWARF POPULATION OF THE GALAXY

A DISSERTATION APPROVED FOR THE
HOMER L. DODGE DEPARTMENT OF PHYSICS AND ASTRONOMY

BY THE COMMITTEE CONSISTING OF

Dr. Mukremin Kilic, Chair

Dr. Nathan Kaib

Dr. Xinyu Dai

Dr. Michael G Strauss

Dr. Kerry Magruder

To my father, Eric Wall, who was always willing to listen and ask questions until he understood.

To my mother, Sandra Wall, who talked me through all my tears and wrote ”The Very Best”, which got her youngest daughter through qualifying exams, many years before she was born.

To my brother, Aaron Wall, who endured many rants over Skype.

To my sister, Audrey Wall, who began blazing this trail. For you I now complete the journey.

Acknowledgements

Just as no man is an island, no dissertation can be created alone. I would like to take this time to thank all of the people who have made this work possible.

To my advisor, Dr. Mukremin Kilic, I thank you for all your guidance, encouragement, patience, and understanding. Without your support, I would not have been able to complete my doctorate, nor would I have half the skills and confidence I have now.

Thank you to Dr. Timothy Miller, Dr. Jenna Nugent, Dr. Hora Mishra, Dr. Alekzander Kosakowski, Dr. Kyra Dame, and all of the wonderful, crazy friends I made throughout my journey through grad school. Words cannot adequately express just how much your friendships mean to me. I will never forget all of the late night conversations we had when we'd lost our minds from too much studying. I still have pictures of our glorious black/whiteboard murals.

I thank my family for all their support and prayers. Thank you for having faith in me when I had no faith in myself.

I would particularly like to thank Dr. Michael G. Strauss. You have been an incredible example of what a Christian scientist should look like. All of the discussions we had during "Dr. Strauss Book Club" meetings had an immense impact on my life and my time in graduate school.

I would finally like to acknowledge the contributions of my committee members, Dr. Nathan Kaib, Dr. Kerry Magruder, and Dr. Xinyu Dai. Thank you for sticking with me through this journey.

Table of Contents

Abstract

DA white dwarfs are the most common type of white dwarf in our Galaxy. Hence, it is important to study the DA white dwarf population as thoroughly as possible. In this dissertation, I present our work using the Galaxy Evolution Explorer (GALEX) data to study the DA white dwarf population in the ultraviolet.

I begin by presenting our use of 1837 DA white dwarfs with high signal-to-noise ratio spectra and *Gaia* parallaxes to verify the absolute calibration and extinction coefficients for GALEX. We use white dwarfs within 100 pc to verify the linearity correction to the GALEX data. We find that the linearity correction is valid for magnitudes brighter than 15.95 and 16.95 for the far-ultraviolet (FUV) and near-ultraviolet (NUV) bands, respectively. We also use DA white dwarfs beyond 250 pc to calculate extinction coefficients in the FUV and NUV bands: $R_{\rm FUV} = 8.01 \pm 0.07$ and $R_{\rm NUV} = 6.79 \pm 0.04$. These are consistent with the predicted extinction coefficients for Milky Way-type dust in the FUV, but smaller than predictions in the NUV. With well understood optical spectra and state-of-the-art model atmosphere analysis, these white dwarfs currently provide the best constraints on the extinction coefficients for the GALEX data.

I then present our detailed model atmosphere analysis of 14001 DA white dwarfs from the Montreal White Dwarf Database with ultraviolet photometry from the GALEX mission. We use the 100 pc sample, where the extinction is negligible, to demonstrate that there are no major systematic differences between the best-fit parameters derived from optical only data and the optical + UV photometry. GALEX FUV and NUV data improve the statistical errors in the model fits, especially for the hotter white dwarfs with spectral energy distributions that peak in the UV. Fitting the UV to optical spectral energy distributions also reveals UV-excess or UV-deficit objects. We use two different methods to identify outliers in our model fits. Known outliers include objects with unusual atmospheric compositions, strongly magnetic white dwarfs, and binary white dwarfs, including double degenerates and white dwarf + main-sequence systems. We present a list of 89 newly identified outliers based on GALEX UV data; follow-up observations of these objects will be required to constrain their nature.

I then conclude by discussing future work in UV observations of white dwarfs. Several current and upcoming large scale spectroscopic surveys are targeting $> 10^5$ white dwarfs. In addition, the ULTRASAT mission is planning an all-sky survey in the NUV band. A combination of the UV data from GALEX and ULTRASAT and optical data on these large samples of spectroscopically

confirmed DA white dwarfs will provide an excellent opportunity to identify unusual white dwarfs in the solar neighborhood.

CHAPTER 1

Introduction

It is human nature to be endlessly curious. Just ask any parent of a small child and they will regale you with tales of all the strange and dangerous things their child has tried to put in its mouth. From the moment we are born, we are driven to explore and understand our surroundings. It is this spirit of curiosity that drives astronomers to understand objects that are so far removed from the daily lives of the majority of Earth's over 7 billion inhabitants as to be considered inconsequential to most.

The objects studied within this dissertation are so faint that, although they are within our own galaxy, they cannot be seen with the naked eye. The objects we seek to understand are white dwarf stars. Let us begin with a definition.

1.1. White Dwarf Stars

White dwarfs are the end stage of life for the majority of all stars. Stars with masses $\leq 8 - 10$ $M_\odot$ ($\approx$97% of all stars) will evolve into white dwarfs (Fontaine, Brassard, & Bergeron, 2001). White dwarfs typically have a mass around 0.6 $M_\odot$ and radii comparable to Earth's (≈ 0.01 $R_\odot$).

During a star's main sequence lifetime, it burns through the hydrogen in the core. Once all the hydrogen has been burned inside the core, all that is left is a thin shell of hydrogen burning around a core of helium ash all surrounded by an envelope of inert hydrogen. Once there is no burning in the core, the core will begin to collapse due to gravity until it reaches the temperature and pressure required to burn helium. While the core is collapsing, the hydrogen burning shell must maintain the same temperature in order to sustain hydrogen burning. In order to maintain the temperature of the hydrogen burning shell, the envelope's temperature must decrease as the core's temperature increases. The same principle holds for the envelope's pressure. As the core's pressure increases, the envelope's pressure must decrease to maintain the proper pressure for hydrogen burning in the shell. This is called the mirror principle. Whatever temperature and pressure changes happen in the core, the opposite changes must happen in the envelope so that the temperature and pressure can be maintained in the hydrogen shell between the core and envelope. So as the core contracts and heats, the envelope cools and expands.

Once the central temperature reaches $\approx 10^8$K, helium burning will begin in the core. Once helium has been exhausted in the core, we are left with a core of carbon and oxygen ash surrounded by first a helium burning shell, then a hydrogen burning shell, all within an inert hydrogen envelope.

When helium is exhausted in the core, it again begins to collapse under the affects of gravity causing the envelope to expand again due to the mirror principle. Depending on the star's mass, the core may or may not be able to begin carbon burning. After the final core burning stage, whether that be helium or carbon, the core begins to contract one last time. As the density of the core increases, the electrons are no longer bound to individual atoms, but are instead shared equally among nearly all the atoms in the core. This makes the core analogous to a single molecule. The Pauli exclusion principle states that no two electrons can share the same energy state. Electrons are therefore forced into higher and higher energy states, greatly increasing their momentum. The highest energy electrons move near the speed of light and carry enough momentum to support the core against the force of gravity. This is called electron degeneracy pressure. During the final core contraction, the energy created by the hydrogen, helium, and (in some cases) carbon burning shells will cause the envelope to rapidly expand, leading to mass loss. What is left is a degenerate core composed of either carbon and oxygen (if only helium was burned) or oxygen and neon (if carbon was burned). This core is surrounded by a thin atmosphere of hydrogen and/or helium.

Now that you know what a white dwarf is, the next logical question is why we study them. What can a dead star possibly teach us?

1.2. What Can a White Dwarf Tell Us?

So far you know a little about the state of matter that comprises the majority of a white dwarf. Extremely high temperatures and pressure create an electron degenerate plasma. Now that we know that such a state of matter exists, we naturally want to know how it works. However, the extreme conditions that occur naturally inside a white dwarf cannot be reproduced here on Earth. The only way to further understand this extreme state of matter is by observing white dwarfs.

Since white dwarfs are no longer producing energy via nuclear fusion and can no longer collapse via gravity due to electron degeneracy pressure, the only thing a white dwarf will do after its formation is cool. Thanks to white dwarf cooling models, we can determine how long a white dwarf has been around (Bergeron, Leggett, & Ruiz, 2001). Using the initial - final mass ratio, we can determine what the main sequence mass of a white dwarf originally was, allowing us to determine how long it took the star to become a white dwarf. Add the cooling age to the main sequence age and you have the total age of the white dwarf. We can use the ages of white dwarfs to estimate the ages of different galactic populations (Mestel, 1952; Winget et al., 1987; Liebert, Dahn, & Monet, 1988).

White dwarfs are thought to be the progenitors of type Ia supernovae (SN Ia). SN Ia occur when a white dwarf nears the Chandrasekhar mass limit ($1.4M_{\odot}$) (Chandrasekhar, 1931). Above this mass, electron degeneracy pressure can no longer support the star against gravity. As a white dwarf approaches this mass limit (for example by accreting matter from a binary companion), the

density in the core will become sufficient to begin carbon burning. The energy produced by carbon burning causes the temperature of the white dwarf to increase, increasing the speed of the carbon burning until it reaches thermonuclear runaway. The resulting explosion completely destroys the white dwarf (Wheeler, 2000). SN Ia are used as standard candles. A standard candle is an object whose absolute magnitude is thought to be well known. If we know an object's absolute magnitude, we can use its apparent magnitude to measure the distance to that object. Since SN Ia are critical in measuring extragalactic distances, a better understanding of the white dwarf population can improve our understanding of SN Ia.

In addition to being a possible progenitor of SN Ia, close white dwarf binary systems are also an important source of gravitational waves. Over time these white dwarfs will spiral closer and closer to each other as they lose energy due to the emission of gravitational waves. Eventually these double degenerate systems will merge. The merger of these binaries will be the dominant source of the gravitational wave foreground for the upcoming *Laser Interferometer Space Antenna* (*LISA*) mission (Nelemans, Yungelson, & Portegies Zwart, 2001; Korol, Rossi, & Barausse, 2019; Nissanke et al., 2012; Korol et al., 2017; Lamberts et al., 2019).

Now that you have a broad idea of the type of information that can be gained by studying white dwarfs, let us move into more of the specifics of this dissertation. In particular we need to discuss the study of white dwarfs in the ultraviolet.

1.3. Why Ultraviolet?

Luckily for us Earth's atmosphere blocks most ultraviolet (UV) wavelengths; but, while they are extremely harmful to humans, UV is a critical component for the understanding of white dwarfs. For the hottest white dwarfs, the peak wavelength of their black body radiation is in the UV. To obtain the most accurate measurement of the effective temperature ($T_{\rm eff}$) of hot white dwarfs, UV data must be obtained.

UV data can also reveal interesting features in a white dwarfs' atmosphere that are not seen in optical bands. $25-50\%$ of white dwarfs are contaminated by metals (Koester, Gänsicke, & Farihi, 2014). Since most metal lines are in the UV, astronomers can gain a better understanding of the atmospheric abundances of different metals using UV data. White dwarfs with strong magnetic fields can be revealed by studying UV data. Strong magnetic fields shift the absorption features and wash them out, greatly affecting the UV output of the white dwarf. For example, the magnetic white dwarf PG 1031+234 has a very flat spectral energy distribution (SED) in the UV but a very steep slope in the optical and infrared (IR) (Schmidt et al., 1986). Schmidt et al. (1986) attempted to fit the SED using nonmagnetic white dwarf models. They found that a $T_{\rm eff} = 15000$K model fit the UV portion of the SED but failed to fit the optical/IR portion while a 25000K model fit the optical/IR but could not fit the UV. A similar principle holds true for some white dwarfs with mixed atmospheres.

While a pure hydrogen model might be able to fit a mixed hydrogen/helium atmosphere fairly well in the optical, the same model might not be able to fit the UV data.

UV data can also reveal unseen binary companions. For white dwarf + M dwarf systems, the M dwarf will dominate in redder bands while the white dwarf will dominate in the UV. It is easier to separate the two components with the addition of UV data. In the case of double degenerate systems, if there is a significant temperature difference between the two white dwarfs, one will dominate in the UV.

A good example of the use of UV data to find unusual white dwarfs is Lajoie & Bergeron (2007). In Lajoie & Bergeron (2007) they compared the effective temperatures obtained from the optical and UV spectra of 140 DA white dwarfs from the *International Ultraviolet Explorer* (*IUE*) archive. They found that the optical and UV temperatures of the majority of stars cooler than 40000 K and within 75 pc are in fairly good agreement with $\Delta T_{\rm eff}/T_{\rm optical} \leq 10\%$. They also found that the majority of the discrepancies between the two temperature measurements were caused by interstellar reddening, which affects the UV more than the optical. By restricting their analysis to white dwarfs within 75 pc, where the extinction is negligible, they were able to identify several double degenerate candidates, as well as a DA + M dwarf system, and stars with unusual atmospheric compositions.

We now see that UV data can be critical in furthering our understanding of white dwarfs. Since most UV wavelengths are blocked by Earth's atmosphere, we must go to space to observe them.

1.4. GALEX

The Galaxy Evolution Explorer (GALEX) was the first space based mission to attempt an all-sky imaging survey in the UV (Martin et al., 2005). GALEX had a Ritchey-Chretin optical design with a 50 cm diameter primary mirror[1] (see figure 1.1). It utilized large format microchannel plate detectors (MCPs). Each MCP consisted of a stack of three microchannel plates separating a photocathode and a delay line detecting anode. The MCP detector was chosen over the more typical CCD for its low background noise, high red rejection, and lack of cooling requirement. However, MCPs have lower quantum efficiency (around 8%) and poor field flatness compared to CCDs. To mitigate local flatness variations, GALEX observed in a spiral dither pattern.

The primary objective of GALEX was to study star formation and the spectral evolution of galaxies in the UV. While observing distant galaxies, many foreground UV sources were also observed. In the ten years that it was operational, GALEX surveyed 26,000 square degrees of the sky as part of the All-sky Imaging Survey (AIS) in two band passes: Far Ultraviolet (FUV) with a central wavelength of 1528 Å and Near Ultraviolet (NUV) with a central wavelength of 2271 Å (Morrissey et al., 2005).

In order to get accurate data from any instrument it is critical to first calibrate that instrument.

[1] http://www.galex.caltech.edu/researcher/techdoc-ch1.html

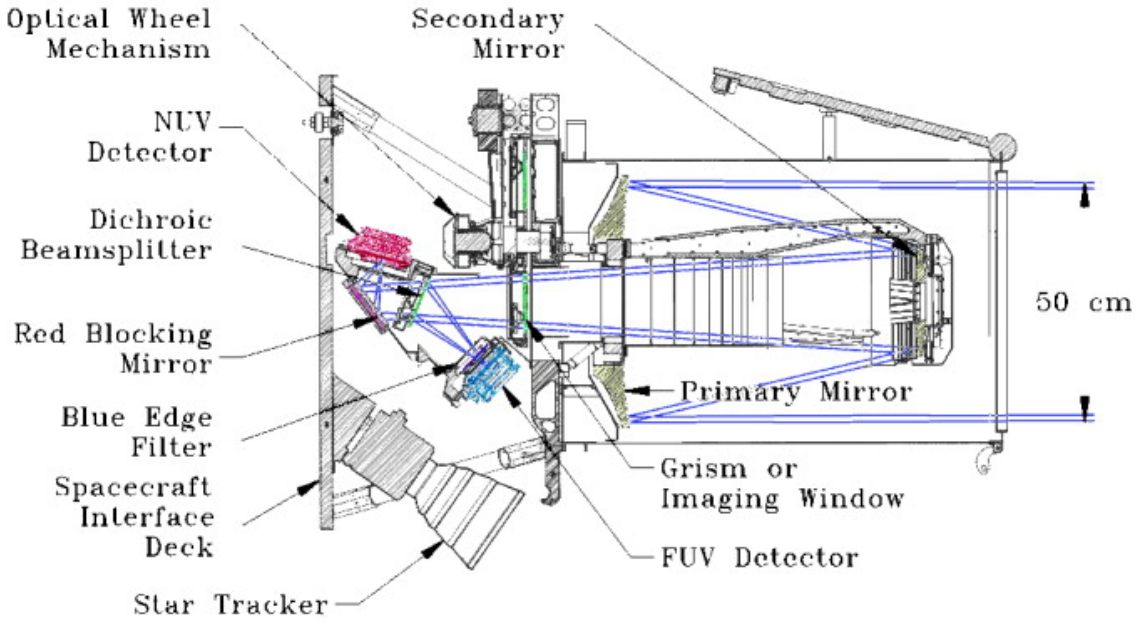

Figure 1.1: A cross section of the GALEX instrument. The double blue line indicates the light path.

Table 1.1. Inverse quadratic corrections from Camarota & Holberg (2014) for the FUV and NUV bands (see Eq 1.1.)

Property	NUV	FUV
c_0	2.634	5.371
c_1	26.316	20.000
c_2	-245.329	-210.200

As a friend of mine put it, you need to measure your ruler.

1.5. Measuring the Ruler

There are many factors that must be taken into account to calibrate an instrument such as GALEX. You must determine the instrument's resolution, any background noise caused by the instrument itself, the photometric zero point, the linearity of the instrument, and many more factors. Almost all of the calibration was done on the ground in thermal vacuum and then checked once GALEX was in space (Morrissey & GALEX Science Team, 2005). In this dissertation, we are specifically interested in one particular factor: the linearity of the GALEX instrument.

There are two sources of nonlinearity in GALEX photometry: global nonlinearity and local nonlinearity. Global nonlinearity is caused by the finite time period required for the electronics to assemble photon lists and is thus well understood and easily corrected for. Local nonlinearity occurs near bright sources, making it much more difficult to correct. Morrissey et al. (2007) demonstrate that nonlinearity becomes significant ($> 10\%$) above 109 and 311 counts per second in the FUV and NUV bands, respectively (see figure 1.2). These correspond to $m_{\rm FUV} \approx 14$ mag and $m_{\rm NUV} \approx 15$ mag. Local nonlinearity complicates the standard star measurements which were used to determine the photometric zero point of GALEX.

GALEX observed 18 white dwarfs from the *Hubble Space Telescope* CALSPEC database (Bohlin, Dickinson, & Calzetti, 2001) as standard stars. However, its photometric calibration relies primarily on the dimmest star in this sample, the DB white dwarf LDS 749b, as all of the other standard stars observed are highly saturated. In fact, after Bohlin & Koester (2008) provided a better CALSPEC spectrum for LDS 749b, the GALEX magnitudes were shifted by ≈ 0.04 mag between the GR4/5 and GR6 data releases. Hence, it is important to verify the photometric calibration using fainter stars.

Camarota & Holberg (2014) verified the GALEX photometric calibration using 99 and 107 DA white dwarfs in the FUV and NUV, respectively, with magnitudes between 10 and 17.5 from the final GR7 GALEX data release. They found that a modest linearity correction is needed in this

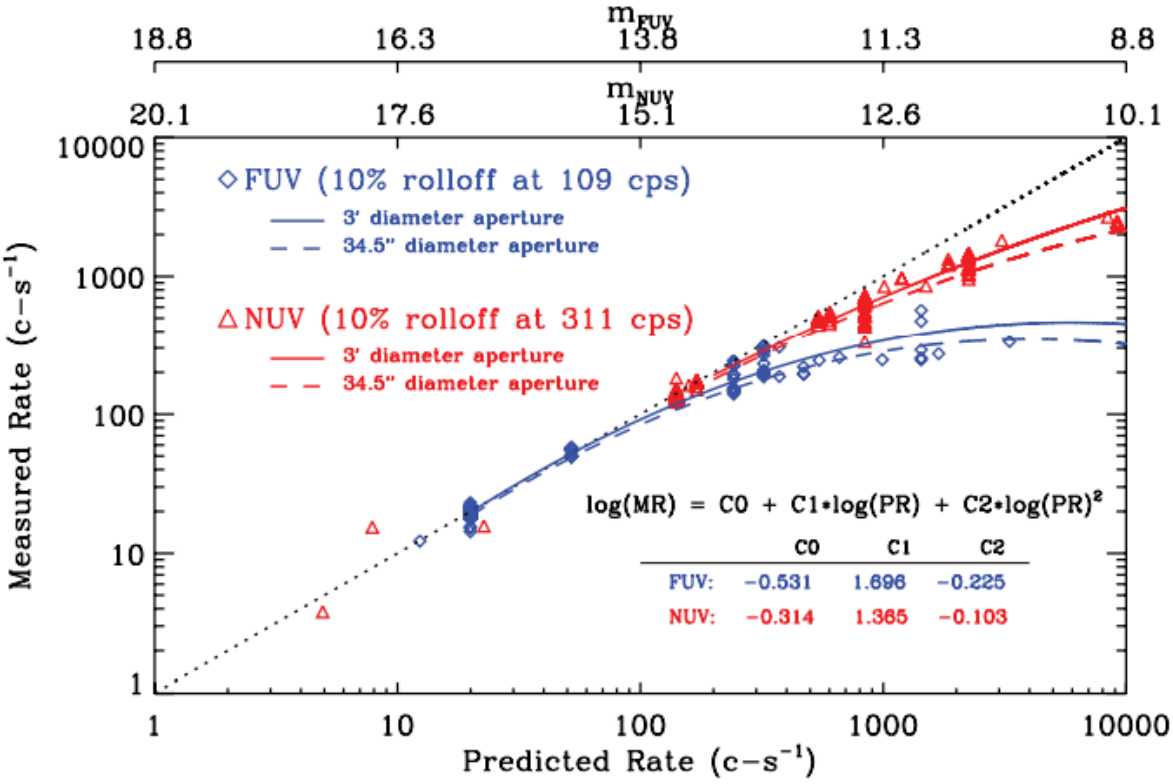

Figure 1.2: Figure 8 from Morrissey et al. (2007). The dotted black line is the 1:1 correlation, the red triangles are NUV measurements and the blue diamonds are FUV measurements. The red and blue solid lines are quadratic fits to the 3 arcminute diameter aperture NUV and FUV data, respectively. The red and blue dashed lines are quadratic fits to the 34.6 arcsecond diameter aperture NUV and FUV data, respectively.

magnitude range. Their corrections take the form

$$m_{\rm corr} = c_0 + (c_1 m_{\rm obs} + c_2)^{1/2}, \tag{1.1}$$

where $m_{\rm obs}$ and $m_{\rm corr}$ are the observed and corrected GALEX magnitudes, respectively. Their calculated constants c_0, c_1, and c_2 are given in Table 1.1. Although Camarota & Holberg (2014) postulate that their linearity correction should hold for stars as faint as 20th magnitude, they state that their corrections for stars dimmer than 16th magnitude should be treated with caution. Camarota & Holberg (2014) point out the need for a larger sample size and the characterization of extinction in the GALEX bands.

We've now discussed one factor that can affect GALEX photometry. Let us now move to another factor: extinction.

1.6. Extinction

The space between stars in our galaxy is not completely empty. Interstellar dust fills the void between stars. The size of this dust is such that it preferentially absorbs and scatters shorter wavelengths. As a result an object will appear to be both redder and dimmer than it actually is. Happily for us, we already have a good idea of the amount of reddening along any given line of sight. Schlafly & Finkbeiner (2011) give a fairly accurate reddening map of our galaxy. The affect of interstellar dust that concerns us in this dissertation is the amount of light absorbed by the dust: the extinction.

Extinction is quantified by an extinction coefficient. These coefficients are defined as

$$R_\lambda = \frac{A_\lambda}{E(B-V)}, \tag{1.2}$$

where A_λ is the total absorption along the line of sight to an object and $E(B-V)$ is the reddening. There is a broad range of GALEX extinction coefficients reported in the literature. Bianchi (2011) provided theoretical estimates of $R_{\rm FUV} = 8.06$ and $R_{\rm NUV} = 7.95$ for Milky Way type dust and $R_{\rm FUV} = 12.68$ and $R_{\rm NUV} = 8.08$ for the Small Magellanic Cloud (SMC) type dust. Although theory is useful, it is preferable to collect empirical evidence for or against that theory if possible.

Yuan, Liu, & Xiang (2013) found empirical values of $R_{\rm FUV} = 4.37 - 4.89$ and $R_{\rm NUV} = 7.06 - 7.24$. They derived these extinction coefficients by using the 'standard pair' technique (Stecher, 1965). In this technique two stars of the same spectral type, one in an area with low extinction and one in an area of high extinction, are compared. The stars with low extinction are called the control sample, and the stars with high extinction are called the target sample. The stars in the control sample are used to determine the intrinsic colors of the corresponding stars in the target

sample. Yuan, Liu, & Xiang (2013) selected their initial sample from the Sloan Digital Sky Survey (SDSS) Data Release 7 (DR7). For the control sample, they selected stars with $E(B-V) < 0.03$. For their target sample, they selected stars with $E(B-V) > 0.1$. Yuan, Liu, & Xiang (2013) examined a target sample of 1396 stars and a control sample of 16405 stars from the GALEX data release GR5. Most of these stars were classified as FG dwarfs. However, there is a great deal of scatter and uncertainty in their derivation of $R_{\rm FUV}$ and $R_{\rm NUV}$, as can be seen in figure 1.3. The majority of the stars in their target sample have $T_{\rm eff} < 7000$K, so their black body curves will peak outside of the UV wavelength range. Yuan, Liu, & Xiang (2013) caution against using their GALEX extinction coefficients and state that a much larger and hotter sample is needed to derive the GALEX extinction coefficients.

1.7. Dissertation Overview

You now know what a white dwarf is, the type of information we can learn from their study, and why UV in particular is so important. You've been introduced to GALEX and the particular calibration factor this dissertation will focus on: linearity. You also know what extinction is and why it is so important that the GALEX extinction coefficients be re-derived.

If I have done my job correctly, you should have all the background information you need to understand this dissertation. Allow me to give you a brief walk through.

In chapter 2, I revisit the linearity calibration done by Camarota & Holberg (2014) to better constrain the magnitudes over which it is applicable. I then re-derive the GALEX extinction coefficients. I will wrap up chapter 2 by discussing some interesting objects found in my sample. Chapter 2 is a reproduction of my published work in the Monthly Notices of the Royal Astronomical Society (MNRAS) and has been reproduced with permission granted to the first-author by the copyright agreement for use in a doctoral dissertation. The reference to the original work is as follows: Wall R. E., Kilic M., Bergeron P., Rolland B., Genest-Beaulieu C., Gianninas A., 2019, MNRAS, 489, 5046.

I build off of my work from chapter 2 in chapter 3 by extending my analysis to include DA white dwarfs from the Montreal White Dwarf Database (MWDD) and data from the Panoramic Survey Telescope and Rapid Response System (Pan-STARRS). Chapter 3 is a reproduction of my published work in the Monthly Notices of the Royal Astronomical Society (MNRAS) and has been reproduced with permission granted to the first-author by the copyright agreement for use in a doctoral dissertation. The reference to the original work is as follows: Wall R. E., Kilic M., Bergeron P., Leiphart N., 2023, MNRAS, 523, 4067.

I conclude in chapter 4 with the bright future of UV in the study of white dwarfs.

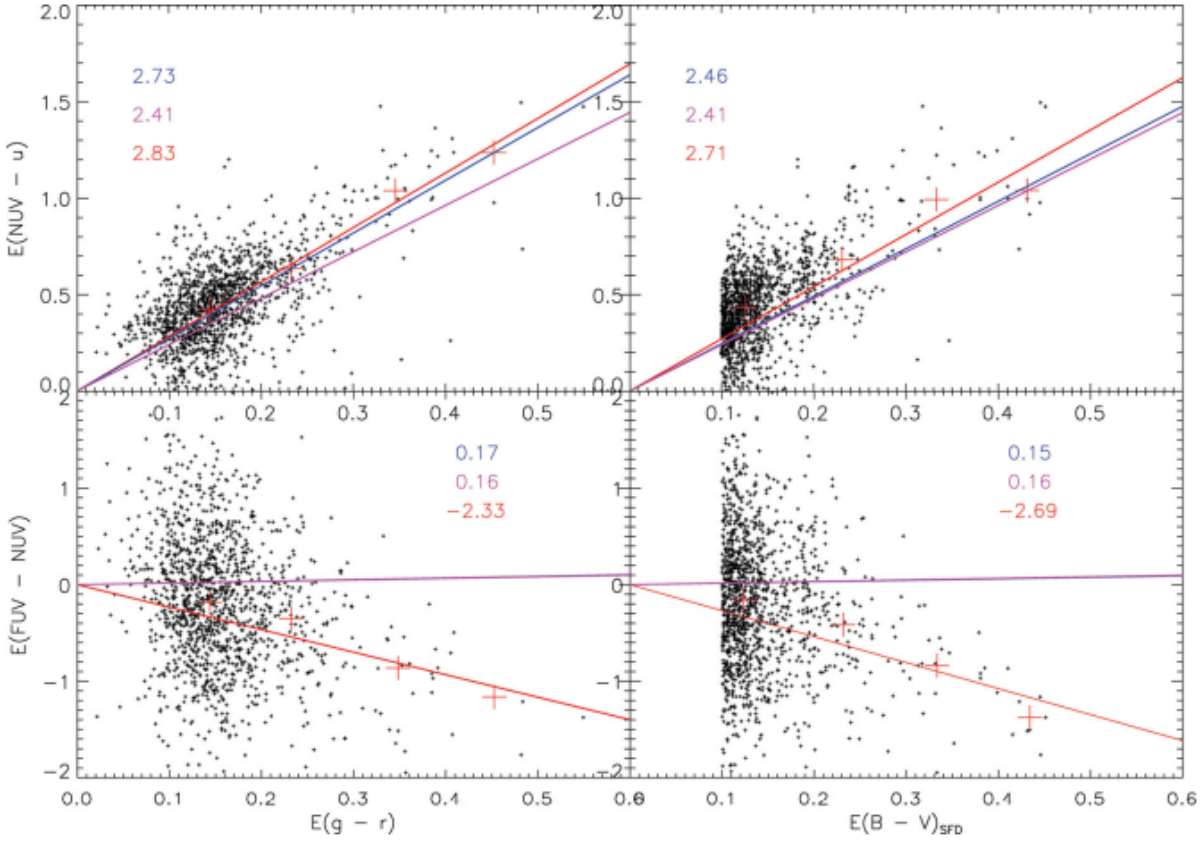

Figure 1.3: Figure 4 from Yuan, Liu, & Xiang (2013). Reddening coefficients of the $NUV - u$ and $FUV - NUV$ colours. (Left panels) Reddening of the $NUV - u$ (top panel) and $FUV - NUV$ (bottom panel) colours versus that of $g - r$. (Right panels) Reddening of the $NUV - u$ (top panel) and $FUV - NUV$ (bottom panel) colours versus $E(B - V)$ from Schlegel, Finkbeiner, & Davis (1998). Red pluses represent median values by binning the data points into eight groups with a bin size of 0.1 on the x-axis. The red lines are linear fits to the binned data. Relations predicted by the Fitzpatrick (1999), Cardelli, Clayton, & Mathis (1989), and O'Donnell (1994) reddening laws for $R(V) = 3.1$ are plotted in purple, blue, and cyan, respectively

CHAPTER 2

GALEX Absolute Calibration and Extinction Coefficients Based on White Dwarfs

2.1. Introduction

The Galaxy Evolution Explorer (GALEX) is the first space based mission to attempt an all-sky imaging survey in the ultraviolet (UV, Martin et al., 2005). In the ten years that it was operational, GALEX surveyed 26,000 square degrees of the sky as part of the All-sky Imaging Survey in two band passes: Far Ultraviolet (FUV) with a central wavelength of 1528 Å and Near Ultraviolet (NUV) with a central wavelength of 2271 Å (Morrissey et al., 2005). Although its primary goal was to study star formation and galaxy evolution, the first science goal was to determine UV calibration, particularly extinction (Martin et al., 2005).

There are two sources of nonlinearity in GALEX photometry: global nonlinearity due to the finite period required for the electronics to assemble photon lists and local nonlinearity near bright sources. Morrissey et al. (2005)(see their Fig. 8) demonstrate that nonlinearity becomes significant ($> 10\%$) above 109 and 311 counts s^{-1} in the FUV and NUV bands, respectively. These correspond to $m_{\rm FUV} \approx 14$ mag and $m_{\rm NUV} \approx 15$ mag. While the first nonlinearity is well understood, the second (local nonlinearity) complicates the standard star measurements.

For photometric calibration GALEX observed 18 white dwarfs from the *Hubble Space Telescope* CALSPEC database (Bohlin, Dickinson, & Calzetti, 2001) as standard stars. However, since all of the other standard stars observed are highly saturated, its photometric calibration relies primarily on the dimmest star in this sample, LDS 749b. After Bohlin & Koester (2008) provided a better CALSPEC spectrum for LDS 749b, the GALEX magnitudes were shifted by ≈0.04 mag between the GR4/5 and GR6 data releases. Hence, it is important to verify the photometric calibration using fainter stars.

Camarota & Holberg (2014) verified the GALEX photometric calibration using 99 and 107 DA white dwarfs in the FUV and NUV, respectively, with magnitudes between 10 and 17.5 from the final GR7 GALEX data release. They found that a modest linearity correction is needed in this magnitude range. Although Camarota & Holberg (2014) postulate that their linearity correction should hold for stars as faint as 20th magnitude, they point out the need for a larger sample size and the characterization of extinction in the GALEX bands. In this work, we investigate the validity of the Camarota & Holberg (2014) linearity correction for a large sample of DA white dwarfs from the

Sloan Digital Sky Survey (SDSS), particularly probing the fainter magnitudes.

There is a broad range of GALEX extinction coefficients reported in the literature. These coefficients are defined in equation 1.2. Most of the GALEX extinction coefficients in the literature are theoretical. Bianchi (2011) provided theoretical estimates of $R_{\rm FUV} = 8.06$ and $R_{\rm NUV} = 7.95$ for Milky Way type dust and $R_{\rm FUV} = 12.68$. Yuan, Liu, & Xiang (2013) found empirical values of $R_{\rm FUV} = 4.37 - 4.89$ and $R_{\rm NUV} = 7.06 - 7.24$. They used the 'standard pair' technique (Stecher, 1965) described in section 1.6. Yuan, Liu, & Xiang (2013) examined a target sample of 1396 stars and a control sample of 16405 stars from the GALEX fifth data release. Most of these stars were classified as FG dwarfs. There is a great deal of scatter and uncertainty in their derivation of the GALEX extinction coefficients, and Yuan, Liu, & Xiang (2013) caution against using their GALEX extinction coefficients. In this work, we re-derive the GALEX extinction coefficients using a large sample of DA white dwarf stars with high S/N SDSS spectra and Gaia parallaxes to obtain a more reliable estimate.

We present the white dwarf sample used in this study in Section 2.2 and describe our calculation of the synthetic magnitudes in Section 2.3. Our analysis of nonlinearity is presented in Section 2.4 followed by our derivation of the GALEX extinction coefficients in Section 2.5. The 3σ outliers are discussed in Section 2.6, and we conclude in Section 2.7.

2.2. Sample Selection

In order to improve calibrations for the GALEX data, we select all spectroscopically confirmed DA white dwarfs from the SDSS data releases 7, 10, and 12 with S/N ≥ 20 spectra (Kleinman et al., 2013; Kepler et al., 2015, 2016). This selection insures that the $T_{\rm eff}$ and $\log g$ measurements are precise enough to model the emergent stellar fluxes in the UV bands. We focus on DA white dwarfs due to our good understanding of their opacities and atmospheres (Holberg & Bergeron, 2006). We cross reference our initial sample of 3733 DA white dwarfs from the SDSS with Pan-STARRS, and we cross reference our sample once more with *Gaia DR*2, selecting all stars with parallax/error ≥ 5. We then cross reference our sample with the GALEX catalog of unique UV sources from the All Sky Imaging Survey (GUVcat) presented in Bianchi et al. (2017). We use a search radius of $2''$ and find a total of 1837 stars with GALEX photometry.

We break our initial sample of stars into two groups based on *Gaia* distance: stars within 100 pc and stars further than 250 pc. There are 339 (627) and 451 (628) stars with FUV and NUV photometry in the 100 ($d > 250$) pc sample, respectively. We leave the examination of stars between 100 and 250 pc for future work (see chapter 4). The local interstellar medium is relatively devoid of cold neutral gas, up to about 100 pc, the boundary of the Local Bubble (Lallement et al., 2003; Redfield, 2006). Since extinction is not an issue for the 100 pc sample, we use it to verify the GALEX photometric calibration. The $d > 250$ pc sample suffers from full extinction, and we use it

to calculate the extinction coefficients in both the FUV and NUV bands.

2.3. Synthetic Magnitudes

Genest-Beaulieu & Bergeron (2019) found a systematic offset between temperatures derived using the spectroscopic (Bergeron, Saffer, & Liebert, 1992) and photometric (Bergeron, Ruiz, & Leggett, 1997) techniques. They determine that this offset is caused by inaccuracies in the treatment of Stark broadening in their model spectra. The photometric technique is less sensitive to the input physics of the models, so we adopted it for this work. We use SDSS *u* and Pan-STARRS *grizy* photometry and *Gaia* parallaxes to derive photometric temperatures and radii for all stars in our final sample. These temperature and radius measurements are then used to calculate a model spectrum for each white dwarf in the 100 pc sample.

To estimate the average flux in a given bandpass, f_λ^m, we use the equation

$$f_\lambda^m = \frac{\int_0^\infty f_\lambda S_m(\lambda)\lambda \mathrm{d}\lambda}{\int_0^\infty S_m(\lambda)\lambda \mathrm{d}\lambda}, \tag{2.1}$$

where $S_m(\lambda)$ is the transmission function of the corresponding bandpass, and f_λ is the monochromatic flux from the star received at Earth (Bergeron, Ruiz, & Leggett, 1997; Gianninas et al., 2011). SDSS, Pan-STARRS, and GALEX use the AB magnitude system. We transform the average flux in a given bandpass to an average magnitude using the equation

$$m = -2.5 \log f_\nu^m - 48.6. \tag{2.2}$$

This procedure enables us to calculate the absolute magnitude of each star in each filter. We use the observed and dereddened SDSS magnitudes for the $d < 100$ and $d > 250$ pc samples, respectively. The full 100 and 250 pc samples can be found in this chapter's appendix.

2.4. GALEX Photometric Calibration

Our 100 pc SDSS sample contains few stars brighter than 14th magnitude. In order to constrain the fit for both faint and bright white dwarfs, we extend our sample to include the 100 pc white dwarfs from Camarota & Holberg (2014) and Gianninas et al. (2011). Figure 2.1 compares the observed and predicted synthetic magnitudes for this sample in both bands. The solid and dashed lines show a quadratic polynomial fit to the data and the 1:1 line, respectively. Stars with $T_{\rm eff}$ below 11,000 K are represented by yellow triangles. Stars below this temperature suffer from the red wing of the Lyα opacity, which affects the ultraviolet more strongly than the optical (Kowalski & Saumon, 2006). The 3σ outliers that are known double degenerates, white dwarf + main sequence binaries, and ZZ Cetis are marked by cyan triangles, green diamonds, and magenta pentagons, respectively. Previously unknown 3σ outliers in our polynomial fit are plotted as red squares. All 3σ outliers are

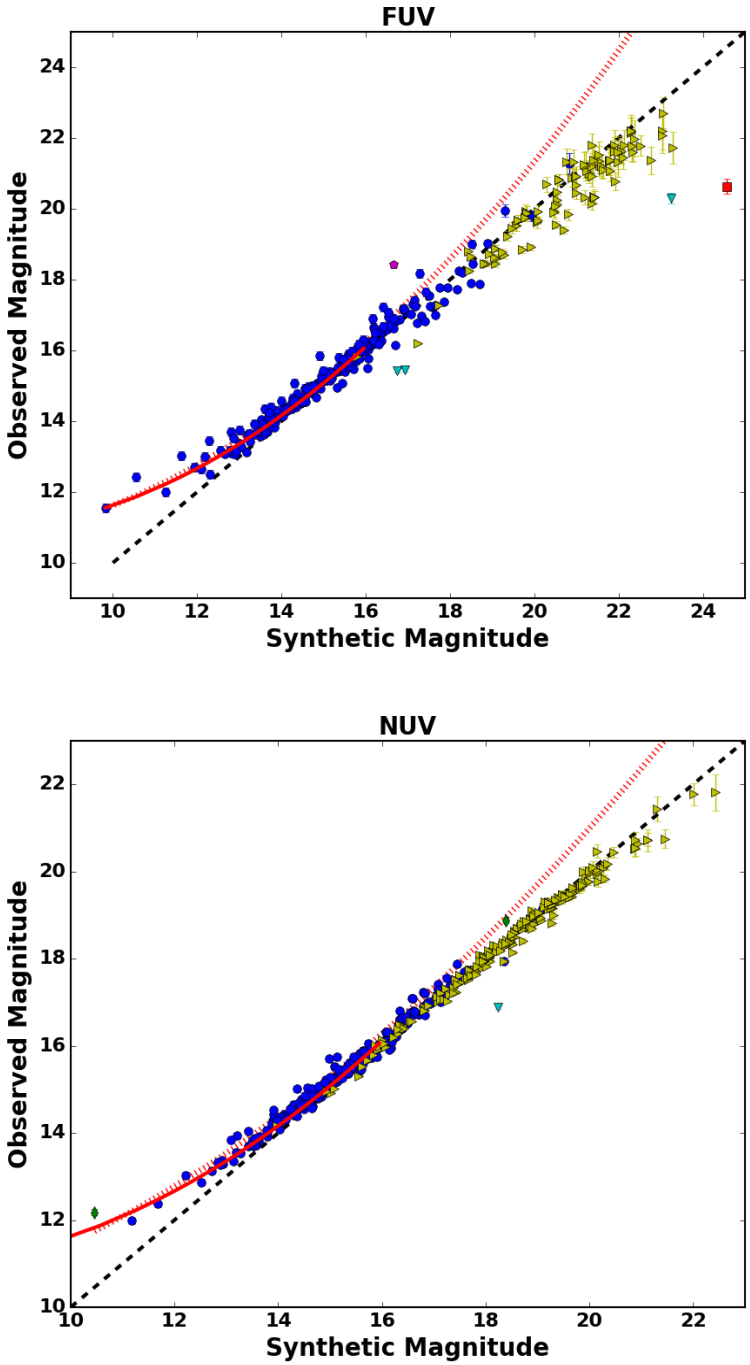

Figure 2.1: The linearity fit for stars within 100 pc in the FUV band (top) and the NUV band (bottom). The quadratic linearity fit from Camarota & Holberg (2014) is marked as the red dashed line. Our linearity fit is plotted in solid red. The black dashed line is the 1:1 correlation. Stars with $T_{\rm eff}$ below 11,000 K are plotted as yellow triangles. Cyan triangles are known double degenerate systems and green diamonds are previously known white dwarf + main sequence binaries. The magenta pentagon marks the ZZ Ceti WD1258+013. Previously unknown 3σ outliers are plotted as red squares.

Table 2.1. Fitting parameters for the linearity correction in the FUV and NUV bands (see Eq 2.3.)

Property	FUV	NUV
c_0	13.23	10.49
c_1	-0.727	-0.31
c_2	0.057	0.041
Range	$\leq$ 15.95 mag	$\leq$ 16.95 mag

excluded from this fit. We further discuss these outliers in Section 2.6.

Our quadratic fits are represented by the expression

$$m_{\rm obs} = c_2 m_{\rm synth}^2 + c_1 m_{\rm synth} + c_0, \tag{2.3}$$

where $m_{\rm obs}$ and $m_{\rm synth}$ are the observed and synthetic GALEX magnitudes, respectively. The best fit values of the fitting coefficients c_0, c_1, and c_2 are given in Table 2.1.

Camarota & Holberg (2014) found a non-linear correlation and small offset between GALEX fluxes and predicted fluxes for their sample. Their quadratic fit is shown as a dotted line in Figure 2.1 and is based on about 100 DA white dwarfs with FUV and NUV magnitudes between 10 and 17.5 mag. However, they only have 6-8 stars fainter than 17th magnitude in their sample, hence the fit is relatively unconstrained at the faint end. The dotted line significantly underpredicts the observed magnitudes in both FUV and NUV bands, and is clearly not useful below 17th magnitude.

With a significantly larger number of fainter DA white dwarfs, we are able to test for non-linearities in the data down to magnitudes fainter than 20. We note that stars with $T_{\rm eff}$ below 11,000 K have systematically fainter synthetic magnitudes in the FUV, while there is no systematic offset in the NUV. Since these stars are affected by the red wing of the Lyα opacity (Kowalski & Saumon, 2006), our results indicate that this opacity source is well handled in our models for the NUV, while the modeling of this opacity should be revisited for the FUV. To remove this systematic effect from our fit, we first fit the full sample to calculate the magnitude where the full quadratic fit crosses the 1:1 line for the FUV and NUV. Only stars brighter than these magnitudes, 15.95 mag (FUV) and 16.95 mag (NUV), will require a linearity correction. To determine the linearity correction, we then fit only stars brighter than 15.95 mag (FUV) and 16.95 mag (NUV). This is our final quadratic fit which is plotted in Figure 2.1. Our linearity corrections are not statistically different from those presented in Camarota & Holberg (2014). To convert the observed GALEX magnitudes into corrected magnitudes, we find the quadratic solutions to the linearity corrections shown in Figure 2.1. Our final corrections take the form

Table 2.2. Inverse quadratic corrections for the FUV and NUV bands (see Eq 2.4.)

Property	FUV	NUV
c_0	6.412	3.778
c_1	17.63	24.337
c_2	-192.135	-241.018

$$m_{\rm corr} = c_0 + (c_1 m_{\rm obs} + c_2)^{1/2}, \tag{2.4}$$

where $m_{\rm obs}$ and $m_{\rm corr}$ are the observed and corrected GALEX magnitudes, respectively. The calculated constants c_0, c_1, and c_2 are given in Table 2.2. These corrections are applicable to objects brighter than 15.95 mag and 16.95 mag in the FUV and NUV, respectively.

2.5. Extinction Coefficients

After revisiting the linearity corrections and determining the magnitudes they are valid over, we examine the sample of SDSS DA white dwarfs with *Gaia* distances beyond 250 pc. We apply the linearity corrections given in Table 2.2 only to those stars brighter than our cut-off magnitudes. Figure 2.2 shows the observed versus synthetic magnitudes for the 250 pc white dwarf sample. These stars experience full extinction, which leads to observed FUV and NUV photometry fainter than expected.

We calculate the R value in the NUV and FUV bands for each star using Equation 1.2, the total absorption in each filter A_λ (the difference between the synthetic and observed magnitude), and $E(B-V)$ from Schlafly & Finkbeiner (2011). We find 9 stars in the FUV and 18 stars in the NUV with negative R values. These stars, as well as the 4σ outliers, are excluded from the weighted average of the R vaules.

Figure 2.3 shows the distribution of the R values in the FUV and NUV filters. Since the R values for some stars have relatively large uncertainties, here we plot weighted histograms, where each R value only contributes its associated error towards the bin count (instead of 1). This figure reveals a relatively large spread in R for both filters, with a standard deviation ~ 3. This spread in R values indicates that we cannot characterize the interstellar extinction by a universal reddening law for all lines of sight within the SDSS footprint. However, our best estimate, the weighted mean values, are $R_{\rm FUV} = 8.01 \pm 0.07$ and $R_{\rm NUV} = 6.79 \pm 0.04$.

Bianchi (2011) estimated GALEX extinction coefficients using progressively reddened models for stars with $T_{\rm eff} = 15,000 - 30,000$ K. Since GALEX NUV band includes the strong broad

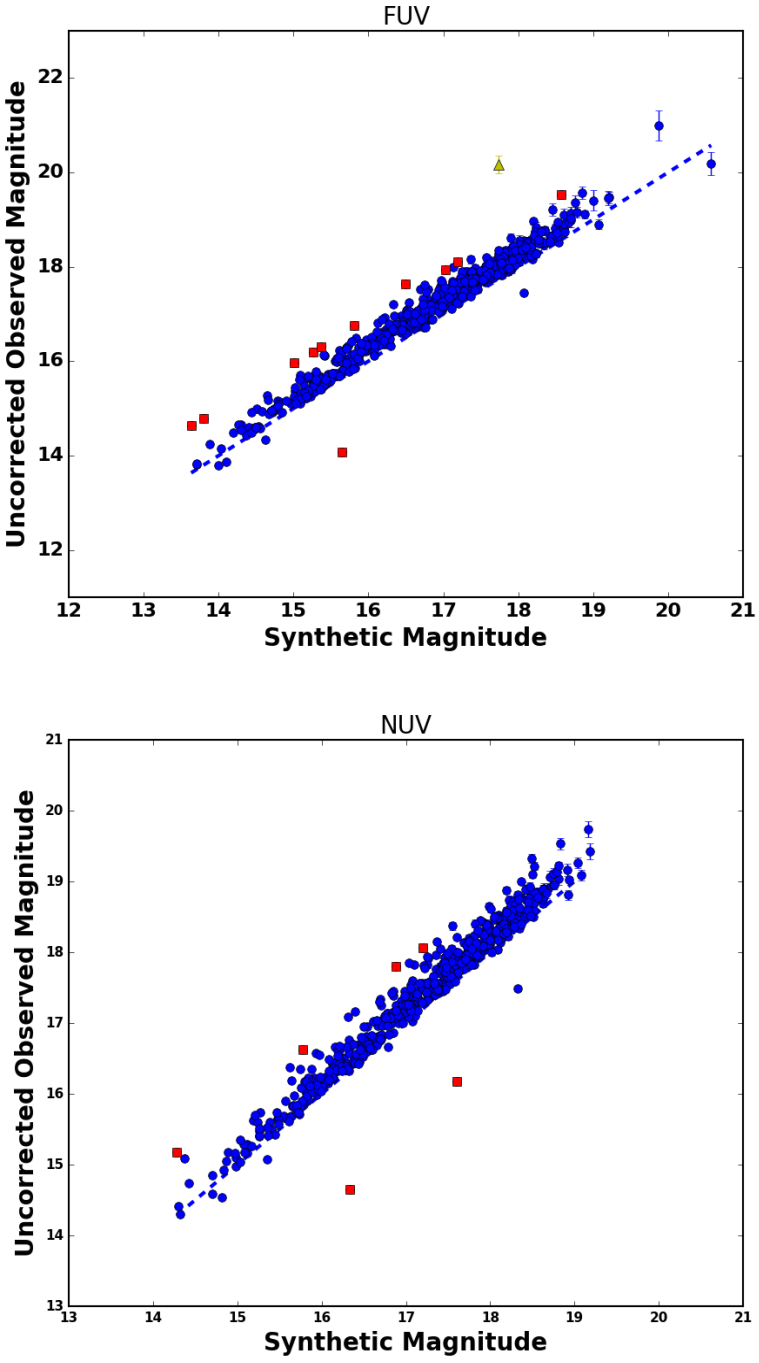

Figure 2.2: Uncorrected versus model magnitudes for stars beyond 250 pc in the FUV and NUV bands. The blue dashed line is the 1:1 correlation and 4σ outliers are plotted as red squares. The candidate double degenerate J211607.27+004503.17 is plotted as a yellow triangle.

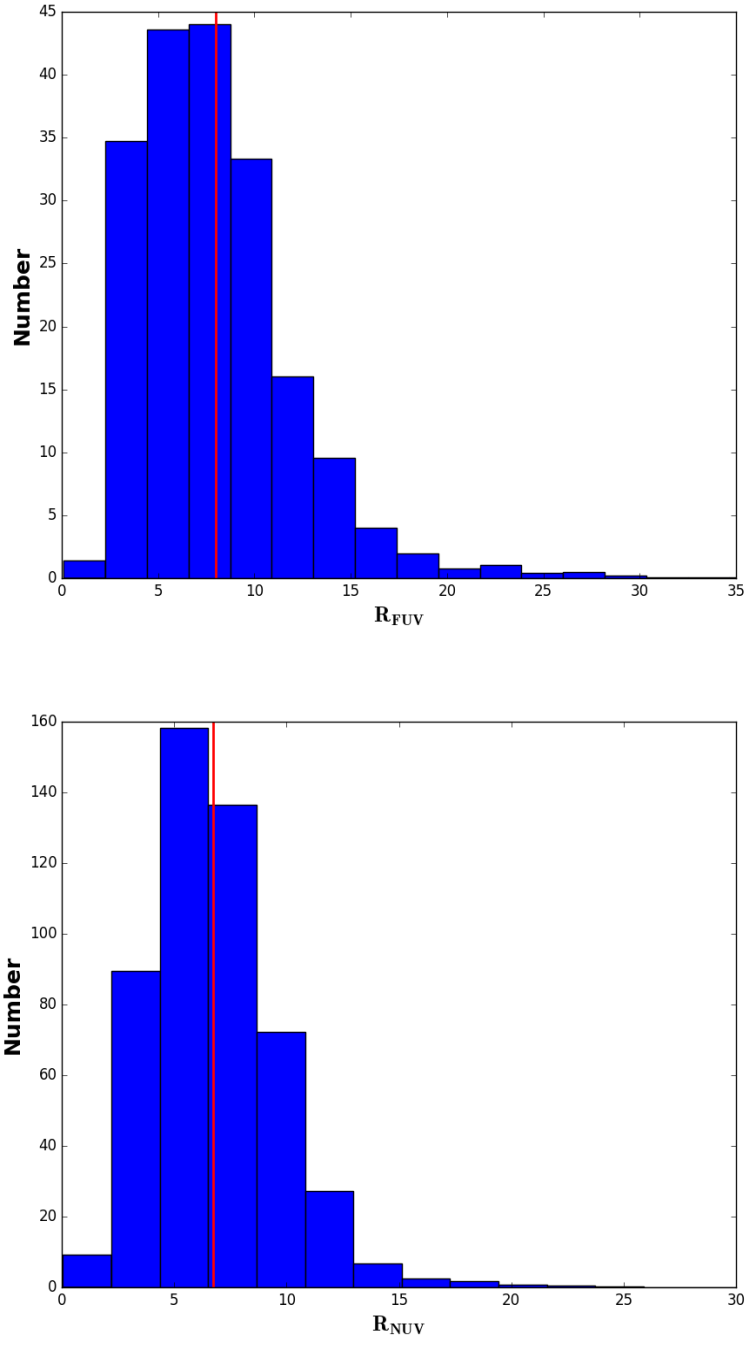

Figure 2.3: Histograms of weighted R values for FUV and NUV bands. The solid red line is the weighted average.

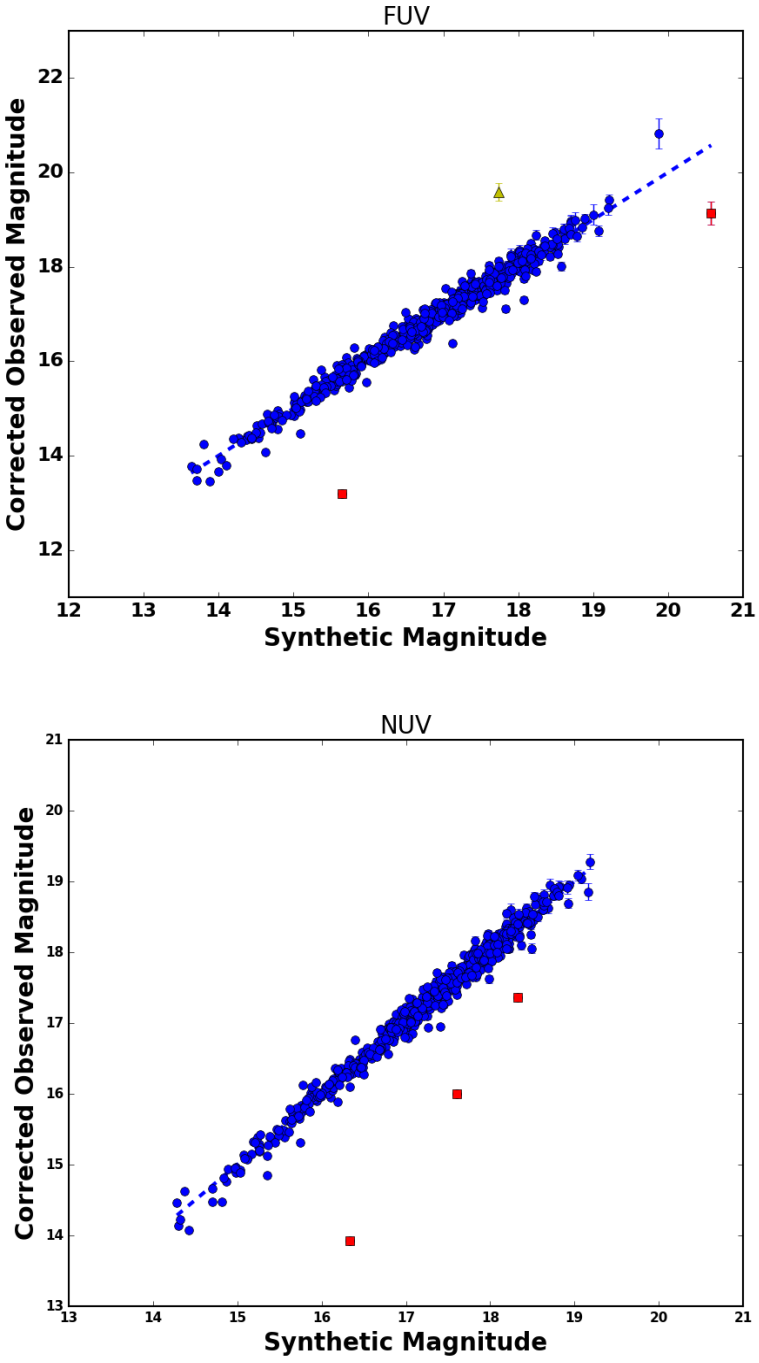

Figure 2.4: Extinction corrected versus model magnitudes for stars beyond 250 pc in the FUV and NUV bands. The blue dashed line is the 1:1 correlation and 4σ outliers are plotted as red squares. The candidate double degenerate J211607.27+004503.17 is plotted as a yellow triangle.

absorption feature at 2175 Å, they predict an overall absorption that is similar in both the FUV and NUV bands. For Milky Way type dust, they predict $R_{\rm FUV} \approx R_{\rm NUV} \approx 8.0$. However, for UV-steep extinction curves like those of the Large Magellanic Cloud (LMC) and the SMC, the increase in absorption is larger in the FUV and the 2175 Å bump is less pronounced, resulting in estimates of $R_{\rm FUV} = 8.6 - 12.7$ and $R_{\rm NUV} = 7.0 - 8.1$. Hence, some of the scatter seen in Figure 2.3 can be explained by the differences in extinction curves along different line of sights as sampled by our targets.

Empirical constraints on GALEX extinction by Yuan, Liu, & Xiang (2013) agree relatively well in the NUV but they differ significantly in the FUV. Yuan, Liu, & Xiang (2013) measure $R_{\rm NUV} = 7.24 \pm 0.08$ or 7.06 ± 0.22 and $R_{\rm FUV} = 4.89 \pm 0.60$ or 4.37 ± 0.54. Our FUV extinction coefficient is significantly larger than the Yuan, Liu, & Xiang (2013) estimate and in good agreement with the Bianchi (2011) estimate. Given the simplicity of DA white dwarf photospheres, white dwarfs are excellent spectrophotometric standard stars and our empirical results are significantly more precise than previous FUV and NUV extinction coefficient measurements.

Figure 2.4 shows a comparison between the observed FUV/NUV magnitudes corrected for non-linearity and extinction and the synthetic magnitudes for the $d > 250$ pc sample using our best-estimates of $R_{\rm FUV} = 8.01 \pm 0.07$ and $R_{\rm NUV} = 6.79 \pm 0.04$. These R values provide excellent corrections for our dataset, as the majority of the objects fall on or near the 1:1 line (shown as a blue dashed line). The red squares mark the 4σ outliers from the 1:1 line. The yellow triangle marks J211607.27+004503.17, a previously known candidate binary system (Baxter et al., 2014). We further discuss the unknown outliers in Section 2.6.

2.6. Outliers

Here we revisit the 3 and 4σ outliers identified in the 100 and 250 pc samples in Sections 2.4 and 2.5, respectively. One possible cause of a significant difference between the observed and model FUV and NUV magnitudes is the presence of an unseen companion. If two stars are sufficiently close together to be unresolved in both GALEX and the SDSS observations, one could still identify the binary nature of the system through UV-excess, like the double white dwarf SDSS J125733.63+542850.5 (Badenes et al., 2009; Kulkarni & van Kerkwijk, 2010; Marsh et al., 2011; Bours et al., 2015). Note that this method only works for systems where there is a significant temperature difference between the two white dwarfs.

Out of our twelve total outliers, seven are previously known systems. Although WD0901+140 is a visual binary (Farihi, Becklin, & Zuckerman, 2005), it was not resolved in GALEX. Of the five remaining outliers, the photometry of WD0846+335 is likely contaminated by a nearby background galaxy. In Figure 3.5.2, we plot the SEDs of the remaining four outliers. We plotted the SDSS and GUVcat fluxes as blue errorbars. Each of these objects has UV observations from other GALEX

Table 2.3. Previously known binary or variable white dwarfs that are identifed as outliers in this work.

Object	Type	Reference
WD0037−006	Double-lined double degenerate	Koester et al. (2009)
WD0232+035	DA+dM	Kawka et al. (2008)
WD0901+140	Visual double degenerate	Farihi, Becklin, & Zuckerman (2005)
WD1019+462	WD+dM	Reid (1996)
WD1022+050	Double degenerate	Bragaglia, Renzini, & Bergeron (1995)
WD1258+013	ZZ Ceti	Bergeron et al. (2004)
J211607.27+004503.17	Double degenerate candidate	Baxter et al. (2014)

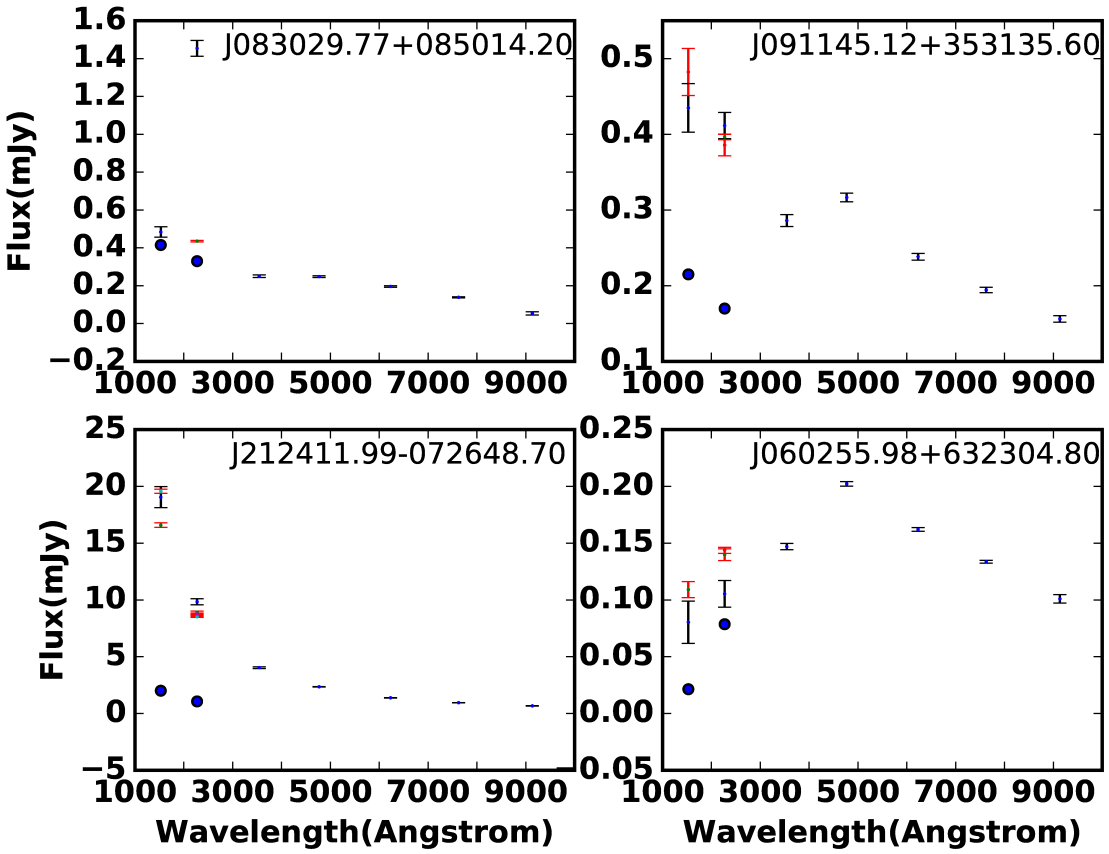

Figure 2.5: SEDs of four newly identified candidate UV-excess white dwarfs. Black errorbars represent fluxes from SDSS and GUVcat. Red errorbars represent fluxes from all other GALEX observations. Blue dots represent model fluxes. Note that two of these outliers, J0830+0850 and J2124−0726, likely have contaminated photometry or inaccurate photometric solutions.

surveys. These fluxes are represented by the red errorbars. Model fluxes are represented by blue dots. J083029.77+085014.20 is sufficiently near to a bright star that its photometry was contaminated in the shallow AIS survey. Deeper surveys removed this contamination, as can be seen in Figure 3.5.2. J212411.99−072648.70 has a spectroscopic $T_{\rm eff}$ of 76,364 K from Kleinman et al. (2013), well above 35,000 K, the $T_{\rm eff}$ above which the photometric technique becomes less reliable (Genest-Beaulieu & Bergeron, 2019). It is likely that the photometric $T_{\rm eff}$ is off, leading to the apparent UV excess. J060255.98+632304.80 has a $T_{\rm eff}$ of 11,078 K and a $\log g$ of 7.7, placing this star within the ZZ Ceti instability strip (10,500−13,000K $T_{\rm eff}$). The UV excess is greater in other GALEX surveys. ZZ Ceti pulsations are stronger in the UV, so the UV excess could be due to pulsations as with WD1258+013. Further observations are needed to confirm that J060255.98+632304.80 is a ZZ Ceti. There are no obvious explanations for the UV excess of J091145.12+353135.60. Follow-up UV spectroscopy or radial velocity observations would be helpful in understanding the nature of this object.

2.7. Conclusions

We examine a sample of 1837 DA white dwarfs that were observed by both SDSS and GALEX. By combining our SDSS sample within 100 pc and the bright white dwarf samples form Camarota & Holberg (2014) and Gianninas et al. (2011), we determine an improved linearity correction to the GALEX data. We determine that our linearity corrections are only necessary for objects brighter than 15.95 mag and 16.95 mag for the FUV and NUV bands, respectively. We present new extinction coefficients for the GALEX bands: $R_{\rm FUV} = 8.01 \pm 0.07$ and $R_{\rm NUV} = 6.79 \pm 0.04$. These white dwarfs currently provide the best constraints on the linearity corrections and extinction coefficients for GALEX data.

Here we present one application of our newly derived *R* values for identifying unusual white dwarfs. We identify seven previously known objects: three double degenerates (WD0037−006, WD0901+140, and WD1022+050), two white dwarf+main sequence binaries (WD1019+462 and WD0232+035), one ZZ Ceti (WD1258+013), and one double degenerate candidate (J211607.27+004503.17) as outliers. We find one previously unknown 3σ outlier and four previously unknown 4σ outliers. The UV-excesses of three of these objects (WD0846+335, J083029.77+085017.20, and J212411.99−072648.70) can be explained by contaminating background sources or inaccurate photometric solutions. Two outliers, J091145.12+353135.60 and J060255.98+632304.80, require follow-up spectroscopy to verify their natures. In the future, we will use our linearity corrections and our newly derived extinction coefficients to study the remainder of our SDSS sample and identify unusual objects.

2.8. Acknowledgements

This work is supported by the NASA Astrophysical Data Analysis Program grant NNX14AF65G. This work is supported in part by the NSERC Canada and by the Fund FRQ-NT (Québec). This work has made use of data from the European Space Agency (ESA) mission *Gaia* (https://www.cosmos.esa.int/gaia), processed by the *Gaia* Data Processing and Analysis Consortium (DPAC, https://www.cosmos.esa.int/web/gaia/dpac/consortium). Funding for the DPAC has been provided by national institutions, in particular the institutions participating in the *Gaia* Multilateral Agreement. We thank our referee, Jay Holberg, for his useful suggestions.

Appendix

2.A. 100 pc Sample

Table begins on the next page.

Table 2.A.1. Properties of stars within 100 pc in our sample. Stars with WD names are from Gianninas et al. (2011).

Star	Synthetic FUV mag	Synthetic NUV mag	Observed FUV mag	Observed NUV mag
J000410.42−034008.60	25.802	19.201	...	19.142 ± 0.070
J001339.11+001924.90	19.769	16.403	19.756 ± 0.103	16.449 ± 0.014
J001339.20+001924.30	19.769	16.403	19.756 ± 0.103	16.449 ± 0.014
J002049.39+004435.10	22.29	17.96	22.194 ± 0.369	17.937 ± 0.027
J002049.55+004433.94	22.29	17.96	22.194 ± 0.369	17.937 ± 0.027
WD0023−109	20.714	17.385	19.394 ± 0.093	17.203 ± 0.019
J002634.39+353337.60	23.59	19.187	...	19.132 ± 0.072
J003328.03+054039.18	26.94	20.354	...	20.167 ± 0.142
J003511.63+001150.40	20.592	17.417	20.817 ± 0.151	17.511 ± 0.022
WD0033+016	18.921	16.312	18.727 ± 0.077	16.368 ± 0.016
WD0037−006	16.92	15.548	15.456 ± 0.016	15.299 ± 0.010
J004511.19+090445.37	25.926	19.923	...	19.922 ± 0.128
WD0048+202	14.519	14.839	14.565 ± 0.008	14.837 ± 0.005
J005438.84−095219.70	22.299	18.077	22.158 ± 0.497	17.942 ± 0.043
WD0058−044	14.933	15.139	14.934 ± 0.016	15.182 ± 0.011
WD0100−036	22.062	17.91	21.635 ± 0.369	17.885 ± 0.039
WD0101+059	16.318	16.138	16.219 ± 0.021	16.132 ± 0.012
WD0101+048	20.513	15.622	19.545 ± 0.103	15.528 ± 0.011
WD0102+095	13.163	13.626	13.130 ± 0.007	13.801 ± 0.006
J010543.14−092054.60	24.111	18.849	...	18.729 ± 0.046
WD0104+015	23.286	18.723	21.735 ± 0.448	18.408 ± 0.063
WD0107+267	15.156	15.181	15.144 ± 0.008	15.231 ± 0.005
J011055.07+143922.30	21.774	17.99	21.338 ± 0.387	18.041 ± 0.033
J011055.16+143921.70	21.774	17.99	21.338 ± 0.387	18.041 ± 0.033
J011104.31+220429.75	23.03	18.747	...	18.853 ± 0.070
WD0126+101	20.094	15.831	19.666 ± 0.087	15.789 ± 0.007
WD0126+422	13.673	14.124	13.788 ± 0.009	14.278 ± 0.008
WD0129−205	14.441	14.772	14.488 ± 0.011	14.799 ± 0.007
WD0135−052	21.535	15.075	21.523 ± 0.374	15.013 ± 0.010
J014342.45+131013.60	24.421	19.252	...	19.302 ± 0.093
WD0142+312	19.931	16.073	18.921 ± 0.085	15.977 ± 0.014
WD0143+216	20.092	16.218	19.933 ± 0.155	16.200 ± 0.015
WD0145+234	14.826	14.358	14.663 ± 0.014	14.383 ± 0.008
J015259.19+010018.50	18.711	17.122	17.879 ± 0.030	17.017 ± 0.014
WD0151+017	15.793	15.327	15.920 ± 0.017	15.390 ± 0.009
WD0155+069	14.041	14.474	14.141 ± 0.017	14.648 ± 0.009

Table 2.A.1 (cont'd)

Star	Synthetic FUV mag	Synthetic NUV mag	Observed FUV mag	Observed NUV mag
WD0220+222	15.467	15.608	15.682 ± 0.019	15.468 ± 0.010
WD0231−054	15.437	14.645	15.085 ± 0.015	14.568 ± 0.008
WD0235+064	15.885	15.713	15.996 ± 0.018	15.767 ± 0.011
WD0242−174	14.478	14.828	14.514 ± 0.015	14.918 ± 0.010
J030335.09+000221.90	23.714	19.203	...	19.289 ± 0.041
J030632.08−063854.40	25.438	19.678	...	19.626 ± 0.066
WD0308+188	13.526	13.794	14.041 ± 0.012	14.031 ± 0.007
J031813.26−010711.70	15.066	15.003	15.149 ± 0.011	15.014 ± 0.006
J032755.79−063605.80	25.644	19.523	...	19.416 ± 0.098
J040457.98−052324.20	22.967	18.793	...	18.853 ± 0.053
J041458.25+064008.20	16.699	15.801	16.162 ± 0.023	15.718 ± 0.011
J053345.36+605750.10	17.412	16.278	16.824 ± 0.028	16.215 ± 0.013
WD0706+294	15.501	15.533	15.615 ± 0.016	15.548 ± 0.010
J073237.88+420454.30	16.064	16.242	16.028 ± 0.020	16.185 ± 0.010
J073708.00+411227.50	17.938	16.412	17.762 ± 0.050	16.457 ± 0.011
J074640.29+355748.10	27.783	20.932	...	20.639 ± 0.134
J075026.29+174029.80	26.348	19.684	...	19.601 ± 0.079
J075443.28+161425.20	24.803	19.4	...	19.403 ± 0.080
J075929.74+473509.50	21.551	17.459	21.221 ± 0.210	17.419 ± 0.010
J080347.31+082914.20	20.548	18.017	20.246 ± 0.125	17.999 ± 0.031
J080418.83+353859.30	22.542	18.552	...	18.495 ± 0.034
J080429.35+421312.70	21.561	17.961	...	17.939 ± 0.033
J080951.09+225054.10	27.755	20.87	...	20.516 ± 0.179
WD0808+423	17.746	17.652	17.768 ± 0.046	17.738 ± 0.031
WD0810+234	15.781	15.927	15.860 ± 0.030	15.946 ± 0.017
WD0816+297	15.318	15.532	15.392 ± 0.014	15.603 ± 0.008
J082001.31+383435.00	24.484	18.481	...	18.379 ± 0.059
J082036.99+431005.20	26.769	19.976	...	19.776 ± 0.084
J082733.10+260703.10	26.577	20.302	...	20.128 ± 0.102
WD0826+455	18.455	15.961	18.237 ± 0.055	15.988 ± 0.009
WD0826+418	20.998	18.077	20.930 ± 0.264	18.092 ± 0.043
J083124.87+164158.60	26.305	19.655	...	19.422 ± 0.041
J083132.75+132243.90	15.792	15.928	15.957 ± 0.020	16.016 ± 0.013
J083723.49+510058.40	25.646	19.474	...	19.461 ± 0.095
WD0836+404	17.173	16.115	17.254 ± 0.048	16.219 ± 0.020
J084252.28+342422.30	16.057	16.168	15.785 ± 0.027	15.941 ± 0.019

Table 2.A.1 (cont'd)

Star	Synthetic FUV mag	Synthetic NUV mag	Observed FUV mag	Observed NUV mag
WD0839+231	12.908	13.416	13.141 ± 0.007	13.698 ± 0.005
J084457.81+453632.80	21.363	17.301	20.153 ± 0.178	17.176 ± 0.027
WD0842+382	23.068	17.709	22.705 ± 0.439	17.619 ± 0.029
J084909.45+342947.70	23.726	17.66	...	17.522 ± 0.030
J084948.62+331925.10	24.561	18.516	20.631 ± 0.211	18.142 ± 0.039
J084949.62+092353.40	22.815	18.896	...	19.104 ± 0.081
J085458.63+275225.60	26.885	20.145	...	20.469 ± 0.159
WD0854+404	13.594	14.025	13.693 ± 0.009	14.118 ± 0.005
J085749.63+180802.50	27.091	20.164	...	19.775 ± 0.128
J085757.63+254207.62	29.396	22.437	...	21.820 ± 0.415
J090318.55+201245.80	25.643	19.205	...	19.306 ± 0.093
WD0901+140	23.242	18.232	20.293 ± 0.155	16.878 ± 0.021
J090638.59+070059.70	14.839	15.069	15.001 ± 0.014	15.203 ± 0.009
J090712.37+364318.40	22.54	18.027	...	18.036 ± 0.046
J091356.83+404734.70	27.32	20.305	...	19.836 ± 0.082
J091635.07+385546.20	18.211	17.087	18.238 ± 0.081	17.219 ± 0.023
WD0915+526	15.512	15.568	15.400 ± 0.026	15.423 ± 0.010
J092252.13+524446.40	16.406	16.362	16.528 ± 0.035	16.409 ± 0.015
WD0921+354	17.22	16.069	16.778 ± 0.033	16.044 ± 0.010
J092551.68+354000.30	26.944	20.274	...	20.070 ± 0.139
J092734.28+094711.15	21.408	18.551	20.355 ± 0.204	18.630 ± 0.050
J092840.28+184113.70	24.412	18.522	...	18.335 ± 0.035
J093610.81+074702.20	22.864	18.671	...	18.742 ± 0.059
J093842.01+541258.40	23.043	19.147	22.189 ± 0.510	19.305 ± 0.080
J094104.43+282224.60	15.383	15.485	15.480 ± 0.015	15.565 ± 0.010
WD0938+550	14.264	14.5	14.477 ± 0.013	14.559 ± 0.006
J094621.44+325128.70	26.971	20.145	...	19.949 ± 0.094
J094631.59+134736.17	15.859	16.09	16.066 ± 0.031	16.176 ± 0.020
WD0943+441	13.503	13.504	13.575 ± 0.009	13.788 ± 0.006
J094850.13+131926.90	26.773	20.017	...	19.982 ± 0.129
J094901.28−001909.60	19.082	17.227	18.881 ± 0.087	17.307 ± 0.030
WD0947+325	14.245	14.67	14.353 ± 0.009	14.747 ± 0.005
J095257.92+480704.60	25.132	19.552	...	19.450 ± 0.098
J095259.11+073106.38	15.683	15.805	15.860 ± 0.021	15.875 ± 0.014
WD0955+247	20.542	16.333	20.482 ± 0.283	16.478 ± 0.027
J095850.56+014724.11	15.319	15.493	15.435 ± 0.014	15.512 ± 0.008

Table 2.A.1 (cont'd)

Star	Synthetic FUV mag	Synthetic NUV mag	Observed FUV mag	Observed NUV mag
WD1001+333	21.176	17.887	21.246 ± 0.359	17.934 ± 0.042
J100356.26+540104.50	21.524	18.263	21.343 ± 0.422	18.231 ± 0.057
J100521.06+535408.40	27.609	20.879	...	20.543 ± 0.178
WD1003−023	14.374	14.712	14.654 ± 0.017	14.824 ± 0.011
J100623.08+071212.60	20.47	17.071	19.923 ± 0.198	17.017 ± 0.016
J100704.45+322947.00	22.134	18.73	21.795 ± 0.422	18.748 ± 0.066
J100720.94+154133.70	26.133	19.785	...	19.623 ± 0.107
J100900.77+362156.30	28.547	21.464	...	20.754 ± 0.206
WD1005+642	12.792	13.144	13.099 ± 0.007	13.354 ± 0.005
WD1008+382	16.518	16.489	16.611 ± 0.032	16.528 ± 0.021
J101414.46+040137.40	25.045	18.839	...	18.721 ± 0.034
J101415.71+502742.60	26.097	19.852	...	19.663 ± 0.116
J101502.56+080636.10	26.048	19.079	...	18.886 ± 0.035
J101548.01+030648.40	17.311	16.181	16.972 ± 0.050	16.145 ± 0.019
J101803.74+155157.74	14.726	15.058	14.991 ± 0.013	15.213 ± 0.006
WD1019+129	14.825	15.13	15.024 ± 0.019	15.231 ± 0.012
J102234.92+460058.80	23.748	18.385	...	18.885 ± 0.071
J102242.46+165842.70	28.026	21.122	...	20.732 ± 0.156
WD1022+050	16.739	15.015	15.429 ± 0.015	14.909 ± 0.007
J102747.64+192824.20	26.22	19.716	...	19.595 ± 0.050
WD1026+023	15.315	14.662	14.960 ± 0.018	14.612 ± 0.005
J103743.48+485720.80	14.397	14.781	14.520 ± 0.013	14.992 ± 0.009
J103746.66+630441.20	25.888	19.818	...	19.694 ± 0.074
WD1039+412	18.502	16.823	17.903 ± 0.071	16.708 ± 0.026
J104411.38+021436.70	26.734	20.174	...	20.015 ± 0.059
J104709.17+345346.50	22.336	17.928	21.591 ± 0.239	17.800 ± 0.023
J104928.88+275422.50	15.997	15.696	16.136 ± 0.029	15.781 ± 0.016
J105500.28+350625.20	16.947	16.926	17.065 ± 0.052	16.977 ± 0.022
J110136.86+174155.90	16.096	16.362	16.221 ± 0.039	16.332 ± 0.021
WD1101+364	14.657	14.701	14.836 ± 0.015	14.846 ± 0.008
J110515.32+001626.10	15.812	15.491	15.850 ± 0.027	15.533 ± 0.007
J110600.59+621017.20	21.303	18.213	20.994 ± 0.259	18.206 ± 0.047
J110604.52+180231.27	18.517	17.721	19.000 ± 0.132	17.696 ± 0.038
J110616.42+451855.80	25.261	19.034	...	18.939 ± 0.073
J111047.52+005421.40	22.847	18.7	...	18.676 ± 0.036
WD1108+475	16.376	15.727	16.270 ± 0.038	15.762 ± 0.016

Table 2.A.1 (cont'd)

Star	Synthetic FUV mag	Synthetic NUV mag	Observed FUV mag	Observed NUV mag
J111425.32+380821.00	18.885	17.114	19.022 ± 0.110	17.244 ± 0.030
WD1116+026	15.774	15.035	15.694 ± 0.028	15.085 ± 0.007
J112146.02+155325.80	26.157	19.868	...	19.746 ± 0.104
WD1120+439	13.754	14.29	13.859 ± 0.011	14.401 ± 0.008
J112518.85+541936.00	15.386	15.439	15.429 ± 0.020	15.457 ± 0.009
J112541.71+422334.80	20.817	17.429	19.848 ± 0.162	17.231 ± 0.031
J112652.44+591917.00	18.869	15.919	18.451 ± 0.087	15.915 ± 0.019
J112731.56+062305.20	23.044	18.481	22.078 ± 0.513	18.469 ± 0.052
J112808.00+415012.70	22.316	18.434	21.784 ± 0.471	18.347 ± 0.057
WD1126+384	13.37	13.891	13.639 ± 0.006	14.290 ± 0.004
J113109.07+064306.10	25.385	19.293	...	19.163 ± 0.081
J113205.63+363414.70	21.906	18.194	21.807 ± 0.412	18.251 ± 0.040
WD1129+155	13.557	13.785	13.680 ± 0.010	13.925 ± 0.006
J113325.69+183934.74	20.284	18.195	20.691 ± 0.209	18.284 ± 0.030
WD1131+333	21.983	17.841	21.592 ± 0.465	17.827 ± 0.038
WD1131+320	15.319	15.335	15.442 ± 0.024	15.395 ± 0.014
WD1132+470	16.045	16.141	15.511 ± 0.022	15.906 ± 0.011
WD1133+293	13.661	14.091	13.705 ± 0.009	14.302 ± 0.007
J113631.30+153044.90	26.534	20.125	...	20.024 ± 0.134
J113728.31+204109.40	25.027	19.253	...	19.163 ± 0.044
WD1137+423	18.285	17.12	18.200 ± 0.071	17.228 ± 0.022
J114012.81+232204.71	20.835	19.084	21.270 ± 0.302	19.141 ± 0.083
WD1143+321	13.37	13.526	13.614 ± 0.009	13.692 ± 0.006
WD1145+187	12.659	13.185	13.071 ± 0.008	13.545 ± 0.002
J115020.05+251832.20	19.372	16.538	19.233 ± 0.135	16.563 ± 0.025
J115052.32+683116.10	25.172	18.354	...	17.941 ± 0.031
WD1149+410	16.072	16.135	16.148 ± 0.034	16.219 ± 0.015
J115421.54+374918.40	24.639	19.31	...	19.235 ± 0.087
WD1152+371	15.596	16.129	15.766 ± 0.027	16.234 ± 0.020
WD1156+291	21.809	17.95	21.067 ± 0.296	17.934 ± 0.044
J115939.35+353803.10	26.251	19.807	...	19.616 ± 0.106
J120003.29+433541.60	23.299	17.62	...	17.529 ± 0.035
J120347.43−002310.90	14.135	14.504	14.345 ± 0.007	14.684 ± 0.005
J120733.82+395324.00	23.016	18.855	...	18.924 ± 0.075
J120843.33+542946.90	24.332	18.928	...	18.803 ± 0.047
J121101.67+365319.60	20.989	18.134	20.666 ± 0.251	18.163 ± 0.028

Table 2.A.1 (cont'd)

Star	Synthetic FUV mag	Synthetic NUV mag	Observed FUV mag	Observed NUV mag
J121135.18+205340.80	27.624	20.411	...	20.197 ± 0.157
J121314.46+114049.94	16.907	16.983	17.141 ± 0.054	17.018 ± 0.031
J121701.40+640402.90	25.357	19.307	...	19.007 ± 0.081
J121730.20+322633.60	25.912	19.833	...	19.668 ± 0.111
WD1216+036	16.157	16.124	16.186 ± 0.033	16.135 ± 0.020
J121856.18+254557.10	16.236	16.383	16.399 ± 0.031	16.422 ± 0.023
J122229.58−024332.50	18.541	17.296	18.459 ± 0.058	17.356 ± 0.023
J122724.31+315023.30	26.842	19.863	...	19.663 ± 0.088
WD1229−012	13.575	13.903	13.612 ± 0.009	14.421 ± 0.008
J123143.80+053155.40	23.48	18.879	...	18.891 ± 0.058
J123324.02+674529.60	21.238	18.041	21.077 ± 0.288	17.995 ± 0.029
J123448.90+054718.20	25.673	19.479	...	19.468 ± 0.075
WD1232+479	14.293	14.409	14.422 ± 0.014	14.582 ± 0.006
J123512.35+231829.70	24.664	19.058	...	18.939 ± 0.064
J123731.44+344822.50	22.524	18.626	21.783 ± 0.292	18.692 ± 0.048
J124009.55−031014.20	19.796	16.811	19.932 ± 0.202	16.878 ± 0.026
J124140.02−073305.70	21.005	17.823	20.438 ± 0.167	17.705 ± 0.027
J124145.51+470621.50	21.361	18.149	21.801 ± 0.329	18.309 ± 0.043
J124341.72+480534.60	17.862	17.199	17.364 ± 0.033	17.107 ± 0.012
WD1243−194	20.059	17.2	19.620 ± 0.164	17.076 ± 0.020
WD1244−125	15.201	14.958	15.212 ± 0.019	15.019 ± 0.007
J124748.90−011109.90	25.858	19.281	...	18.825 ± 0.071
WD1249+182	14.554	14.888	14.722 ± 0.016	14.931 ± 0.011
J125607.24+155115.20	23.515	19.124	...	19.172 ± 0.047
WD1253+105	16.699	16.475	16.819 ± 0.030	16.563 ± 0.014
J125804.48+501445.80	22.917	18.06	...	18.043 ± 0.034
WD1257+047	13.828	14.236	13.831 ± 0.009	14.572 ± 0.008
WD1257+032	15.069	15.316	15.239 ± 0.017	15.370 ± 0.007
J130014.78+181734.40	21.197	17.658	20.319 ± 0.203	17.570 ± 0.037
WD1258+593	15.287	15.354	15.420 ± 0.023	15.366 ± 0.006
WD1258+013	16.654	16.568	18.413 ± 0.052	17.096 ± 0.014
J130606.98+181123.10	24.654	19.477	...	19.329 ± 0.070
WD1304+227	19.712	17.27	18.845 ± 0.095	17.019 ± 0.031
J130820.81+001330.20	16.35	16.381	16.465 ± 0.016	16.476 ± 0.011
WD1310+583	17.243	14.93	16.199 ± 0.016	14.947 ± 0.005
J131420.62+070051.10	21.592	18.226	21.209 ± 0.328	18.294 ± 0.053

Table 2.A.1 (cont'd)

Star	Synthetic FUV mag	Synthetic NUV mag	Observed FUV mag	Observed NUV mag
J132011.39+471222.10	24.857	19.279	...	19.232 ± 0.060
WD1319+466	14.57	14.547	14.544 ± 0.009	14.688 ± 0.007
J132159.59+334507.10	23.218	19.027	...	19.046 ± 0.058
J132435.13+622637.70	19.821	17.062	19.879 ± 0.191	17.136 ± 0.031
J132436.89+085754.00	23.002	18.137	...	18.149 ± 0.050
J132512.98+085210.10	20.769	17.88	21.334 ± 0.363	18.077 ± 0.049
J132742.07+575506.40	26.615	19.679	...	19.496 ± 0.072
J132937.15−013430.50	25.965	19.433	...	19.368 ± 0.100
J133652.06+372720.90	24.72	18.862	...	18.906 ± 0.072
J134027.10+322823.90	22.372	18.205	21.980 ± 0.511	18.140 ± 0.050
WD1339+346	15.554	15.719	15.516 ± 0.014	15.706 ± 0.010
WD1344+572	13.584	13.568	13.712 ± 0.005	13.726 ± 0.003
J134701.30+255256.40	26.456	19.887	...	19.989 ± 0.134
WD1349+552	17.529	16.39	17.253 ± 0.039	16.407 ± 0.016
J135709.49+334802.92	16.119	16.18	16.156 ± 0.049	16.227 ± 0.012
J135925.32−003426.40	19.565	17.492	19.535 ± 0.153	17.613 ± 0.022
J140617.23+181248.20	26.072	19.604	...	19.406 ± 0.062
J140625.56+160827.90	27.384	20.466	...	20.444 ± 0.119
J140945.24+421600.70	18.441	15.863	18.803 ± 0.070	16.014 ± 0.012
WD1408+323	13.262	13.548	13.431 ± 0.009	13.717 ± 0.007
J141303.60+325646.00	20.544	17.643	20.123 ± 0.240	17.559 ± 0.040
J141306.54+075522.98	15.386	15.493	15.418 ± 0.020	15.550 ± 0.008
J141454.74+433658.10	27.878	20.884	...	20.727 ± 0.184
J141600.15+000801.25	16.218	16.17	16.204 ± 0.028	16.142 ± 0.019
J142211.13+305618.90	22.684	18.367	...	18.280 ± 0.032
J143406.76+150817.80	16.104	16.077	16.259 ± 0.034	16.141 ± 0.013
J143513.93+505224.80	21.414	17.958	21.375 ± 0.369	18.054 ± 0.043
J143624.32+475301.60	24.204	18.965	...	18.985 ± 0.079
J144111.57+451143.00	21.804	18.344	21.370 ± 0.220	18.376 ± 0.035
WD1441+323	17.508	16.899	17.559 ± 0.046	17.011 ± 0.022
J144416.16−005236.60	27.826	21.113	...	20.715 ± 0.246
J144418.26+471704.20	20.495	17.434	20.064 ± 0.169	17.514 ± 0.028
J144433.80−005958.80	17.596	16.709	17.226 ± 0.068	16.713 ± 0.030
J144433.80−005958.90	17.596	16.709	17.226 ± 0.068	16.713 ± 0.030
WD1443+295	15.71	14.955	15.470 ± 0.027	14.971 ± 0.012
WD1444+350	19.463	16.893	19.458 ± 0.164	16.916 ± 0.020

Table 2.A.1 (cont'd)

Star	Synthetic FUV mag	Synthetic NUV mag	Observed FUV mag	Observed NUV mag
J144859.19−023230.10	21.632	18.059	21.109 ± 0.267	18.178 ± 0.038
WD1448+411	16.197	16.131	16.220 ± 0.031	16.143 ± 0.018
WD1448+077	15.385	15.474	15.559 ± 0.023	15.546 ± 0.015
WD1449+513	16.236	16.422	16.276 ± 0.024	16.474 ± 0.017
WD1449+168	14.349	14.74	14.387 ± 0.014	14.818 ± 0.010
J145308.94+092502.53	20.9	18.407	20.881 ± 0.256	18.422 ± 0.048
J145756.35+282749.10	22.173	18.597	...	18.692 ± 0.049
J150141.15+343158.90	14.703	15.108	14.798 ± 0.009	15.183 ± 0.005
WD1459+305	13.007	13.491	13.365 ± 0.007	13.765 ± 0.003
WD1501+032	15.346	15.445	15.535 ± 0.018	15.598 ± 0.012
J150506.17+325959.50	21.913	18.01	21.662 ± 0.299	17.824 ± 0.033
J150617.10+293440.50	23.408	18.953	...	19.017 ± 0.081
WD1503−093	16.016	15.492	16.113 ± 0.031	15.557 ± 0.010
WD1507+220	13.996	14.351	14.227 ± 0.013	14.482 ± 0.009
WD1508+548	15.212	15.424	15.341 ± 0.017	15.510 ± 0.009
WD1507−105	19.283	16.42	18.704 ± 0.110	16.393 ± 0.017
J151109.85+404801.10	21.426	17.121	20.320 ± 0.172	17.213 ± 0.020
WD1509+536	15.953	15.992	15.966 ± 0.026	16.003 ± 0.017
J151151.36+562450.50	21.374	17.519	21.199 ± 0.368	17.449 ± 0.037
WD1515+668	19.231	16.305	18.782 ± 0.100	16.266 ± 0.019
J151912.00+123946.50	21.99	18.32	21.319 ± 0.426	18.307 ± 0.068
J152006.00+080327.30	16.264	16.244	16.263 ± 0.034	16.243 ± 0.021
WD1519+383	14.919	15.24	15.058 ± 0.015	15.253 ± 0.008
J152714.52+431302.90	17.121	16.8	17.288 ± 0.035	16.916 ± 0.018
J153332.96−020655.90	18.169	17.038	17.734 ± 0.076	17.146 ± 0.023
WD1531+184	17.069	16.619	17.012 ± 0.049	16.722 ± 0.026
WD1531−022	13.2	13.499	13.635 ± 0.007	13.847 ± 0.003
J153417.50+021848.10	22.792	17.778	...	17.745 ± 0.041
J153424.85+003756.10	23.733	18.924	...	18.977 ± 0.077
J153615.85+501350.60	20.941	17.135	21.324 ± 0.353	17.078 ± 0.032
WD1537+651	19.096	15.714	18.597 ± 0.104	15.662 ± 0.017
J153950.86+015400.20	22.777	18.687	21.368 ± 0.388	18.801 ± 0.073
WD1537−152	15.629	15.781	15.664 ± 0.022	15.851 ± 0.016
J154026.51+234334.72	16.229	16.369	16.349 ± 0.028	16.490 ± 0.018
WD1541+650	17.642	16.183	17.002 ± 0.047	16.090 ± 0.020
J154934.78+053517.10	14.551	15.021	14.627 ± 0.010	15.125 ± 0.009

Table 2.A.1 (cont'd)

Star	Synthetic FUV mag	Synthetic NUV mag	Observed FUV mag	Observed NUV mag
J155004.45+220034.45	19.312	17.308	19.951 ± 0.166	17.402 ± 0.027
WD1548+149	13.975	14.385	14.165 ± 0.009	14.580 ± 0.007
WD1550+183	14.722	14.757	14.931 ± 0.012	14.815 ± 0.007
WD1553+353	13.598	14.02	13.711 ± 0.007	14.078 ± 0.006
J155937.38+252909.00	22.677	17.974	...	18.022 ± 0.035
J160216.99+163023.56	29.077	22.018	...	21.773 ± 0.255
J160353.89+080837.60	25.903	19.624	...	19.479 ± 0.074
J160554.53−002811.20	21.228	17.716	21.217 ± 0.416	17.735 ± 0.041
J160840.92+425652.50	22.907	18.575	...	18.600 ± 0.030
J160949.60+161919.00	26.377	19.86	...	19.689 ± 0.088
J161708.73+155438.70	14.838	15.105	15.073 ± 0.015	15.283 ± 0.007
WD1619+123	14.166	14.376	14.412 ± 0.017	14.551 ± 0.005
J162436.83+321252.50	19.073	17.383	18.459 ± 0.115	17.341 ± 0.039
WD1624+477	21.929	17.816	20.782 ± 0.250	17.647 ± 0.022
J162813.26+122451.80	17.164	16.537	17.431 ± 0.039	16.767 ± 0.015
J162918.99+004551.60	21.906	18.552	21.615 ± 0.408	18.586 ± 0.059
WD1631+396	13.855	14.112	13.978 ± 0.013	14.421 ± 0.006
J163729.21+011000.90	26.625	20.005	...	20.015 ± 0.086
WD1636+160	16.179	15.922	16.285 ± 0.022	15.989 ± 0.009
J163920.30+403041.50	23.325	18.508	...	18.542 ± 0.040
WD1654+637	15.439	15.582	15.524 ± 0.015	15.608 ± 0.011
J165538.93+253346.00	19.934	17.488	19.803 ± 0.153	17.557 ± 0.028
J165559.38+123150.00	17.101	17.023	17.169 ± 0.037	17.127 ± 0.022
J165610.85+194202.12	16.214	16.227	16.270 ± 0.024	16.267 ± 0.016
J170158.82+611118.10	19.606	17.678	19.682 ± 0.137	17.741 ± 0.033
J170653.98+631659.60	20.982	18.447	20.89 ± 0.238	18.36 ± 0.043
J171210.43+562925.00	26.576	20.069	...	20.092 ± 0.152
J172229.99+264527.60	15.127	15.233	15.352 ± 0.018	15.349 ± 0.011
J180623.07+231242.10	23.488	19.336	...	19.342 ± 0.092
J181110.59+242312.90	23.916	18.893	...	18.691 ± 0.051
J204446.30+153311.90	15.383	15.57	15.507 ± 0.017	15.659 ± 0.012
J204531.21+152643.10	16.799	16.614	16.863 ± 0.031	16.714 ± 0.020
J204616.23−064426.50	22.119	18.287	21.447 ± 0.324	18.184 ± 0.042
WD2051+095	15.938	16.044	16.051 ± 0.025	16.107 ± 0.010
J211507.40−074151.60	24.24	19.025	...	19.051 ± 0.062
J212935.22+001332.10	20.448	16.824	19.911 ± 0.142	16.829 ± 0.019

Table 2.A.1 (cont'd)

Star	Synthetic FUV mag	Synthetic NUV mag	Observed FUV mag	Observed NUV mag
WD2136+229	18.503	16.009	18.653 ± 0.071	16.143 ± 0.014
J220602.42−004632.92	15.346	15.599	15.445 ± 0.014	15.681 ± 0.011
J221319.16+292538.96	27.937	21.299	...	21.438 ± 0.287
WD2220+133	14.329	14.778	14.468 ± 0.015	14.919 ± 0.006
WD2226+061	14.28	14.489	14.540 ± 0.011	14.613 ± 0.007
WD2240−017	21.367	17.446	20.920 ± 0.288	17.419 ± 0.029
J224529.48−100244.30	23.05	18.393	...	18.339 ± 0.036
WD2254+126	17.654	16.335	17.279 ± 0.036	16.376 ± 0.016
WD2303+242	17.732	16.032	17.269 ± 0.029	16.06 ± 0.012
WD2306+130	15.849	15.632	15.779 ± 0.019	15.611 ± 0.011
WD2306+124	14.143	14.511	14.294 ± 0.009	14.673 ± 0.007
WD2314+064	15.481	15.712	15.593 ± 0.024	15.818 ± 0.013
WD2318+126	16.668	16.499	16.612 ± 0.028	16.513 ± 0.017
WD2322+206	16.314	15.893	16.176 ± 0.023	15.917 ± 0.012
WD2333−049	19.056	16.568	18.629 ± 0.107	16.565 ± 0.022
WD2336−079	15.799	13.971	15.826 ± 0.026	14.173 ± 0.007
WD2347+128	18.799	16.812	18.459 ± 0.082	16.800 ± 0.017

2.B. 250 pc Sample

Table begins on the next page.

Table 2.B.1. Properties of stars beyond 250 pc in our sample. Stars with WD names are from Gianninas et al. (2011).

Star	Synthetic FUV mag	Synthetic NUV mag	Observed FUV mag	Observed NUV mag
J000302.59+240555.80	18.699	18.73	19.461 ± 0.077	19.241 ± 0.039
J000626.69+242441.70	18.196	18.372	18.964 ± 0.067	18.995 ± 0.031
J001043.55+253829.18	15.968	16.526	16.395 ± 0.020	16.890 ± 0.010
J001549.44+245604.91	15.691	16.253	16.038 ± 0.016	16.558 ± 0.009
J001712.70+250443.04	17.95	18.125	18.218 ± 0.047	18.391 ± 0.026
J002126.69−093714.20	17.688	17.946	18.049 ± 0.035	18.252 ± 0.024
WD0019+150	15.3	15.863	15.697 ± 0.018	16.160 ± 0.013
J002636.48−100330.50	17.116	17.444	17.552 ± 0.050	17.757 ± 0.024
J002806.49+010112.20	16.185	16.67	16.477 ± 0.028	16.885 ± 0.022
J003533.74+240253.17	17.293	17.688	17.683 ± 0.057	18.139 ± 0.048
J004346.36+254910.50	18.482	18.482	18.695 ± 0.120	18.647 ± 0.065
J004648.66+250915.10	17.924	18.095	18.405 ± 0.091	18.525 ± 0.043
J005547.78−084507.30	13.795	14.376	14.885 ± 0.014	15.160 ± 0.011
J010810.17+183120.46	16.957	17.351	17.586 ± 0.065	17.956 ± 0.044
J011100.64+001807.20	19.873	19.182	20.996 ± 0.320	19.425 ± 0.109
J011428.32+215310.79	16.21	16.764	16.439 ± 0.034	17.012 ± 0.027
J011541.62+310404.20	16.432	16.952	16.963 ± 0.042	17.318 ± 0.030
J012041.19+395307.20	17.423	17.683	17.671 ± 0.067	17.923 ± 0.033
J012318.14+330014.34	17.713	17.892	17.927 ± 0.043	18.12 ± 0.029
J012601.53+332523.49	16.21	16.702	16.917 ± 0.042	17.252 ± 0.022
J013250.66+234308.54	17.761	17.915	18.289 ± 0.047	18.428 ± 0.029
J013909.83+073941.58	18.603	18.685	19.107 ± 0.123	18.897 ± 0.076
J014341.57+222201.56	18.849	18.833	19.571 ± 0.137	19.533 ± 0.080
J014413.38+140719.40	18.055	18.141	18.456 ± 0.083	18.394 ± 0.055
J014557.72+130610.80	16.94	17.462	17.498 ± 0.055	17.922 ± 0.044
J014729.02+235141.11	17.182	17.444	17.652 ± 0.055	17.845 ± 0.041
J014847.62−000120.80	17.719	17.938	18.158 ± 0.055	18.305 ± 0.036
J015211.73−090502.59	17.956	18.276	18.343 ± 0.060	18.483 ± 0.040
J015525.57+064233.41	16.331	16.852	17.205 ± 0.053	17.393 ± 0.033
J020952.21+055430.90	15.615	16.154	16.228 ± 0.035	16.718 ± 0.025
J021348.57+054223.00	18.262	18.297	18.534 ± 0.088	18.545 ± 0.032
J021517.11+001440.50	16.876	17.236	17.289 ± 0.037	17.508 ± 0.021
J022446.30−074820.20	17.313	17.519	17.517 ± 0.054	17.761 ± 0.042
J023543.18−055442.07	17.218	17.469	17.420 ± 0.052	17.603 ± 0.037
J025325.82−002751.60	17.305	17.598	17.906 ± 0.077	17.995 ± 0.045
J025507.00−080852.20	16.78	17.157	17.280 ± 0.044	17.467 ± 0.026

Table 2.B.1 (cont'd)

Star	Synthetic FUV mag	Synthetic NUV mag	Observed FUV mag	Observed NUV mag
J031504.58−065727.10	16.982	17.263	17.671 ± 0.035	17.914 ± 0.027
J032215.59−054707.30	16.673	17.027	16.741 ± 0.039	17.182 ± 0.031
J032400.23+055536.70	18.568	18.493	19.524 ± 0.089	19.328 ± 0.064
J032430.71+040054.90	18.072	18.221	18.562 ± 0.075	18.743 ± 0.052
J032615.34+000221.70	17.129	17.552	18.000 ± 0.071	18.370 ± 0.056
J032726.26−071150.00	15.585	16.188	16.047 ± 0.028	16.667 ± 0.022
J033257.68−070434.90	15.557	16.124	16.012 ± 0.023	16.480 ± 0.018
J035416.31+095738.40	17.833	17.982	18.346 ± 0.072	18.653 ± 0.051
J042353.85+065353.10	17.126	17.404	17.692 ± 0.046	18.055 ± 0.036
J044424.97−053436.10	16.339	16.81	16.674 ± 0.029	17.075 ± 0.025
J060055.10+643234.50	16.77	17.251	17.342 ± 0.056	17.819 ± 0.043
J060255.98+632304.80	20.575	19.161	20.192 ± 0.246	19.737 ± 0.117
J061938.24+635656.50	13.634	14.284	14.734 ± 0.012	15.244 ± 0.008
J064924.84+273256.90	16.787	17.265	17.185 ± 0.033	17.471 ± 0.029
J070954.46+403210.20	17.839	18.017	18.102 ± 0.057	18.250 ± 0.038
J071201.60+381655.30	16.685	17.142	16.957 ± 0.041	17.356 ± 0.023
J072020.88+364706.30	15.737	16.188	15.959 ± 0.017	16.367 ± 0.014
J072308.84+370214.40	16.576	17.112	16.880 ± 0.031	17.336 ± 0.025
J072559.68+353836.30	17.328	17.568	17.600 ± 0.039	17.763 ± 0.023
J072837.66+405049.52	17.226	17.595	17.588 ± 0.040	17.813 ± 0.026
J073247.77+213346.80	18.042	18.212	18.316 ± 0.061	18.354 ± 0.043
J073511.20+265708.35	15.538	16.103	15.829 ± 0.017	16.289 ± 0.010
J073702.90+473749.20	16.543	16.886	17.248 ± 0.036	17.795 ± 0.028
J073852.47+220331.10	16.646	17.06	16.931 ± 0.029	17.208 ± 0.023
J074059.12+380810.20	15.647	16.215	16.191 ± 0.022	16.673 ± 0.015
J074206.21+265355.14	17.457	17.836	17.774 ± 0.048	17.974 ± 0.026
J074243.02+394512.38	16.571	17.109	16.975 ± 0.029	17.450 ± 0.025
J074747.06+243802.10	17.539	17.789	17.815 ± 0.045	17.998 ± 0.032
J074749.82+664949.70	18.034	18.224	18.289 ± 0.084	18.382 ± 0.058
J074803.72+300001.80	16.576	17.11	16.949 ± 0.039	17.404 ± 0.024
J075052.61+135622.56	16.751	17.18	17.052 ± 0.034	17.305 ± 0.023
J075115.11+433513.90	17.693	17.997	18.058 ± 0.054	18.181 ± 0.033
J075129.40+340128.34	16.844	17.284	17.127 ± 0.045	17.487 ± 0.026
J075144.34+243954.40	17.152	17.503	17.583 ± 0.042	17.752 ± 0.030
J075301.85+831017.10	16.641	17.1	16.755 ± 0.028	17.178 ± 0.023
J075405.35+132708.70	14.029	14.707	14.287 ± 0.009	14.935 ± 0.008

Table 2.B.1 (cont'd)

Star	Synthetic FUV mag	Synthetic NUV mag	Observed FUV mag	Observed NUV mag
J075455.50+164217.10	18.058	18.179	18.426 ± 0.067	18.335 ± 0.046
J075722.06+521043.32	17.984	18.271	18.255 ± 0.073	18.720 ± 0.062
J075821.12+274101.72	16.445	16.996	16.661 ± 0.029	17.150 ± 0.021
J075825.99+200040.32	17.443	17.765	17.728 ± 0.060	18.017 ± 0.040
J080020.33+455730.74	17.221	17.5	17.547 ± 0.049	17.896 ± 0.045
J080405.14+394436.10	17.663	17.735	18.004 ± 0.082	18.016 ± 0.042
J080624.33+395307.12	17.782	18.007	18.22 ± 0.079	18.307 ± 0.049
J080644.92+193427.70	16.611	17.106	16.912 ± 0.055	17.370 ± 0.038
J080751.70+282907.50	17.649	17.887	17.897 ± 0.050	17.967 ± 0.028
J080758.75+134419.10	16.108	16.685	16.366 ± 0.025	16.815 ± 0.022
J080808.67+063815.40	16.527	17.0	16.849 ± 0.029	17.296 ± 0.023
J080920.82+383358.10	17.717	17.971	17.820 ± 0.069	18.120 ± 0.037
J080921.89+192400.10	14.63	15.354	14.46 ± 0.016	15.142 ± 0.005
J080954.58+322315.30	16.66	17.111	16.878 ± 0.043	17.313 ± 0.024
J081035.27−063234.70	16.917	17.442	17.384 ± 0.061	17.800 ± 0.040
J081234.94+040852.10	15.575	16.075	15.825 ± 0.022	16.189 ± 0.017
J081254.33+501620.30	15.575	16.133	15.985 ± 0.022	16.482 ± 0.015
J081331.82+272203.96	14.714	15.259	15.010 ± 0.014	15.521 ± 0.010
J081540.18+081238.40	16.048	16.564	16.310 ± 0.021	16.778 ± 0.017
J081640.91+362148.71	18.092	18.369	18.427 ± 0.063	18.771 ± 0.049
J081658.25+444953.40	16.717	17.071	17.143 ± 0.032	17.387 ± 0.024
J081721.55+164710.18	16.58	17.08	16.807 ± 0.026	17.029 ± 0.014
J081806.88+121155.39	15.565	16.126	15.771 ± 0.019	16.264 ± 0.017
WD0814+569	14.441	15.037	15.005 ± 0.017	15.406 ± 0.014
J081845.58+485855.20	16.814	17.204	17.165 ± 0.049	17.520 ± 0.036
J081934.42+322412.06	16.187	16.711	16.621 ± 0.035	17.032 ± 0.018
J082010.35+454301.81	17.804	17.95	18.199 ± 0.086	18.404 ± 0.056
J082220.50+494246.37	15.946	16.45	16.347 ± 0.032	16.769 ± 0.025
J082251.66+452928.10	16.865	17.264	17.217 ± 0.045	17.551 ± 0.034
J082407.44+314210.51	17.972	18.14	18.283 ± 0.054	18.406 ± 0.040
J082437.69+474851.88	15.99	16.481	16.299 ± 0.030	16.706 ± 0.024
J082706.21+311536.00	16.047	16.595	16.341 ± 0.023	16.852 ± 0.019
J082717.14+163250.39	17.369	17.601	17.551 ± 0.063	17.747 ± 0.042
J082944.47+530101.00	16.522	17.08	17.086 ± 0.032	17.596 ± 0.026
J082954.66+485226.70	17.059	17.414	17.413 ± 0.038	17.710 ± 0.028
J083029.77+085014.20	17.355	17.605	17.397 ± 0.036	16.214 ± 0.015

Table 2.B.1 (cont'd)

Star	Synthetic FUV mag	Synthetic NUV mag	Observed FUV mag	Observed NUV mag
J083115.34−051815.90	15.009	15.565	15.250 ± 0.021	15.704 ± 0.016
J083138.31+422135.10	17.377	17.734	17.722 ± 0.045	18.035 ± 0.021
J083238.24+550532.30	16.884	17.276	17.264 ± 0.036	17.517 ± 0.025
J083330.83−044857.20	18.071	18.242	18.346 ± 0.065	18.461 ± 0.042
J083337.06+481451.50	17.458	17.655	17.665 ± 0.060	17.820 ± 0.044
J083423.17+043745.02	17.712	17.946	17.949 ± 0.052	18.107 ± 0.039
J083650.28+155326.40	14.759	15.402	15.057 ± 0.014	15.553 ± 0.006
J083838.53+065240.08	14.783	15.475	15.236 ± 0.014	15.7 ± 0.011
J084151.11+225316.20	16.114	16.667	16.477 ± 0.039	16.957 ± 0.028
J084430.27+480327.50	17.618	17.928	17.910 ± 0.065	18.162 ± 0.048
J084529.99+290718.20	17.219	17.413	17.434 ± 0.041	17.494 ± 0.027
J084607.76+544012.80	17.358	17.772	17.804 ± 0.050	18.156 ± 0.038
J084618.45+154419.93	15.708	16.334	16.291 ± 0.035	16.723 ± 0.027
J084639.28+091406.80	15.417	16.082	16.112 ± 0.020	16.538 ± 0.016
J085135.27+161837.08	16.758	17.009	16.967 ± 0.038	17.134 ± 0.028
J085209.16+841150.30	16.702	17.23	16.991 ± 0.029	17.519 ± 0.026
J085230.99+533901.80	15.817	16.398	15.948 ± 0.024	16.544 ± 0.020
J085314.76+133620.38	16.065	16.494	16.217 ± 0.019	16.578 ± 0.016
J085528.43+610211.30	15.022	15.571	15.439 ± 0.014	15.943 ± 0.011
J085634.52+502748.30	15.581	16.14	15.781 ± 0.028	16.264 ± 0.014
J085638.83+093818.06	17.359	17.705	17.597 ± 0.051	17.942 ± 0.036
J085727.50+025805.20	17.14	17.416	17.330 ± 0.043	17.567 ± 0.031
J085727.50+025805.20	17.14	17.416	17.330 ± 0.043	17.567 ± 0.031
J085804.06+531031.90	16.443	16.994	16.849 ± 0.042	17.319 ± 0.023
J085838.73+170147.93	17.32	17.634	17.629 ± 0.056	17.777 ± 0.041
J085944.19+504051.00	15.391	15.954	15.702 ± 0.022	16.191 ± 0.013
J090029.66+181941.80	15.984	16.396	16.239 ± 0.036	16.589 ± 0.024
J090059.86+062920.60	16.511	16.96	17.074 ± 0.049	17.310 ± 0.031
J090136.12+162704.20	15.025	15.673	15.523 ± 0.016	16.013 ± 0.014
J090250.50+173149.30	17.295	17.629	17.551 ± 0.042	17.867 ± 0.034
J090254.09+575821.90	17.646	17.825	17.778 ± 0.042	17.895 ± 0.031
J090348.57+083456.50	17.357	17.607	17.819 ± 0.045	17.831 ± 0.031
J090352.80+193643.60	14.53	15.115	14.724 ± 0.017	15.349 ± 0.012
J090416.45+584301.10	16.397	16.852	16.658 ± 0.032	17.017 ± 0.021
J090431.82+143747.50	16.525	17.056	17.042 ± 0.031	17.538 ± 0.027
J090525.49+394339.10	17.729	17.843	17.861 ± 0.061	18.007 ± 0.031

Table 2.B.1 (cont'd)

Star	Synthetic FUV mag	Synthetic NUV mag	Observed FUV mag	Observed NUV mag
J090611.00+414114.30	15.368	15.942	15.486 ± 0.014	16.025 ± 0.010
J090726.02+174135.88	16.811	17.258	17.164 ± 0.040	17.44 ± 0.028
J090757.30+084524.90	18.522	18.467	18.809 ± 0.066	18.858 ± 0.040
J091008.92+835535.50	18.188	18.116	18.160 ± 0.052	18.136 ± 0.035
J091109.46+165345.40	16.464	16.974	16.871 ± 0.033	17.298 ± 0.026
J091145.12+353135.60	18.069	18.325	17.452 ± 0.062	17.489 ± 0.037
J091258.85+091815.60	16.699	17.076	17.127 ± 0.034	17.431 ± 0.019
J091438.68+233127.60	15.973	16.476	16.450 ± 0.044	16.783 ± 0.014
J091601.87+200758.10	15.25	15.803	15.660 ± 0.022	16.078 ± 0.011
J091616.66+155727.50	16.607	17.077	16.811 ± 0.037	17.321 ± 0.027
J091719.14+195438.66	14.697	15.263	15.014 ± 0.016	15.456 ± 0.007
J091729.86+122727.90	16.51	16.942	16.746 ± 0.027	17.170 ± 0.024
J091841.84+061702.10	13.711	14.302	14.003 ± 0.007	14.549 ± 0.006
J092010.55+045721.10	14.512	15.188	15.077 ± 0.013	15.670 ± 0.010
WD0920+306	15.356	15.615	15.493 ± 0.016	15.656 ± 0.010
J092404.84+593128.80	16.514	16.947	16.792 ± 0.028	17.068 ± 0.010
J092415.31+563750.60	17.114	17.45	17.308 ± 0.046	17.628 ± 0.035
J092416.44+671013.20	15.836	16.337	16.492 ± 0.035	16.786 ± 0.027
J092454.58+543422.30	15.736	16.266	16.069 ± 0.030	16.557 ± 0.015
J092526.56+535312.30	17.424	17.76	17.685 ± 0.055	17.921 ± 0.029
J092553.76+540748.40	17.866	18.149	17.895 ± 0.063	18.268 ± 0.034
J092646.30+122135.68	16.548	16.971	16.831 ± 0.028	17.194 ± 0.022
J092905.46+061118.70	15.724	16.325	16.328 ± 0.022	16.836 ± 0.018
J093000.80+651412.50	16.244	16.754	16.674 ± 0.038	17.048 ± 0.027
J093047.08+160012.53	14.81	15.383	15.220 ± 0.018	15.650 ± 0.015
J093058.92+074454.40	15.348	15.91	15.785 ± 0.019	16.275 ± 0.015
J093132.67+115454.29	16.543	17.0	16.760 ± 0.032	17.225 ± 0.023
J093311.28+205250.70	16.675	17.068	17.041 ± 0.032	17.363 ± 0.023
J093410.29+553149.60	18.696	18.748	19.136 ± 0.133	18.945 ± 0.049
J093515.96+562042.11	15.58	16.219	16.056 ± 0.028	16.518 ± 0.022
WD0934+337	15.031	15.488	15.189 ± 0.013	15.617 ± 0.009
J093921.83+264401.10	15.009	15.649	15.334 ± 0.016	15.870 ± 0.012
J093957.04+644634.20	15.266	15.772	16.190 ± 0.028	16.679 ± 0.021
J094200.06+312920.20	16.276	16.595	16.442 ± 0.023	16.686 ± 0.017
J094203.19+544630.20	15.405	15.958	15.631 ± 0.023	16.112 ± 0.013
J094342.17+000923.20	16.798	17.207	17.521 ± 0.053	17.812 ± 0.040

Table 2.B.1 (cont'd)

Star	Synthetic FUV mag	Synthetic NUV mag	Observed FUV mag	Observed NUV mag
J094537.90+503038.05	18.132	18.343	18.425 ± 0.093	18.340 ± 0.053
J094658.77+471024.28	17.078	17.379	17.207 ± 0.046	17.526 ± 0.036
J094913.84+315930.10	16.534	16.916	16.719 ± 0.027	16.998 ± 0.021
J094927.59+042508.40	15.137	15.751	15.576 ± 0.016	16.131 ± 0.013
J094940.37+032425.50	14.964	15.55	15.177 ± 0.013	15.732 ± 0.011
J095005.33+495548.94	15.174	15.718	15.293 ± 0.018	15.827 ± 0.015
J095329.07+092409.60	15.26	15.866	15.692 ± 0.023	16.244 ± 0.014
J095536.62+041112.40	16.42	16.86	16.664 ± 0.027	17.076 ± 0.020
J095629.73+641430.20	17.266	17.529	17.437 ± 0.047	17.657 ± 0.035
J095951.46+355244.29	17.268	17.569	17.416 ± 0.039	17.667 ± 0.028
J100200.17+151007.39	16.803	17.272	17.083 ± 0.043	17.544 ± 0.035
J100605.29+450404.19	15.226	15.787	15.337 ± 0.020	15.893 ± 0.016
J100651.72+490053.88	17.789	17.926	17.942 ± 0.067	18.05 ± 0.043
J100756.04+180848.70	17.181	17.517	17.534 ± 0.042	17.811 ± 0.029
J100931.54+025646.07	17.388	17.719	17.683 ± 0.068	17.975 ± 0.056
J101039.45+542519.30	16.299	16.8	16.658 ± 0.034	17.040 ± 0.028
J101205.63+615651.90	15.645	16.228	16.011 ± 0.018	16.475 ± 0.012
J101328.17+061207.40	14.38	14.984	14.670 ± 0.017	15.165 ± 0.006
WD1011+335	16.979	17.34	17.170 ± 0.053	17.558 ± 0.039
J101612.78+390115.06	16.733	17.102	16.718 ± 0.034	17.169 ± 0.028
J101924.90+280748.00	15.776	16.324	16.131 ± 0.021	16.629 ± 0.017
J102010.07−014228.98	17.741	17.985	18.277 ± 0.063	18.370 ± 0.043
J102016.09+054919.16	17.325	17.649	17.752 ± 0.067	17.870 ± 0.032
J102042.68+041302.80	16.943	17.297	17.049 ± 0.048	17.422 ± 0.022
J102157.96+291931.30	17.818	18.025	18.078 ± 0.049	18.239 ± 0.036
J102443.90+121437.97	17.364	17.654	17.769 ± 0.065	17.958 ± 0.026
J102449.53+230710.13	17.615	17.892	17.786 ± 0.051	18.020 ± 0.034
J102549.72+003906.20	14.299	14.864	14.761 ± 0.020	15.128 ± 0.014
J102625.20+040534.30	16.002	16.487	16.336 ± 0.034	16.756 ± 0.028
J102632.82+621313.52	18.338	18.509	18.470 ± 0.092	18.496 ± 0.040
J102955.94+145355.28	17.024	17.217	17.931 ± 0.052	17.774 ± 0.024
J103016.66+494520.70	15.31	15.881	15.542 ± 0.021	16.097 ± 0.017
J103032.45+633317.70	15.065	15.626	15.211 ± 0.020	15.715 ± 0.015
J103158.27+012053.59	17.972	18.176	18.260 ± 0.086	18.457 ± 0.028
J103233.61+475908.96	17.201	17.525	17.325 ± 0.050	17.556 ± 0.021
J103326.58+614816.79	17.788	18.122	17.828 ± 0.048	18.189 ± 0.037

Table 2.B.1 (cont'd)

Star	Synthetic FUV mag	Synthetic NUV mag	Observed FUV mag	Observed NUV mag
J103500.15+180750.70	17.094	17.351	17.300 ± 0.058	17.562 ± 0.018
J103510.47+605546.06	17.359	17.806	17.654 ± 0.037	17.830 ± 0.032
J103906.00+654555.50	16.616	17.099	16.847 ± 0.040	17.294 ± 0.031
J103935.39+084559.20	16.431	16.817	16.598 ± 0.033	16.990 ± 0.020
J104002.57+195305.28	16.251	16.747	16.621 ± 0.035	17.015 ± 0.019
J104109.60+500945.07	16.2	16.705	16.367 ± 0.033	16.874 ± 0.028
J104216.68+123112.97	17.577	17.841	17.838 ± 0.070	18.114 ± 0.028
J104314.98+353519.64	15.847	16.301	16.182 ± 0.031	16.475 ± 0.022
J104419.01+405553.00	15.4	15.925	15.571 ± 0.022	16.072 ± 0.018
J104546.43+091825.16	16.314	16.855	16.617 ± 0.035	17.150 ± 0.015
J104650.65+533521.50	17.977	18.084	18.079 ± 0.072	18.231 ± 0.025
J104744.13+663734.30	16.985	17.32	17.071 ± 0.041	17.416 ± 0.030
J105331.07+435656.26	17.81	17.994	17.936 ± 0.052	18.107 ± 0.023
J105525.18+441608.29	16.843	17.105	16.884 ± 0.029	17.096 ± 0.014
J105549.60−010025.88	17.916	18.141	18.385 ± 0.087	18.490 ± 0.042
J105725.64+640352.10	17.827	18.069	18.048 ± 0.052	18.265 ± 0.038
J105802.33+361156.60	16.191	16.716	16.574 ± 0.039	16.964 ± 0.030
J105811.27+475752.00	15.645	16.203	15.89 ± 0.019	16.420 ± 0.013
J105827.19+172117.57	17.588	17.776	17.867 ± 0.067	18.033 ± 0.048
J105842.58+175331.52	16.669	17.071	16.881 ± 0.041	17.272 ± 0.031
J110219.76+121253.90	16.795	17.262	17.104 ± 0.048	17.544 ± 0.038
J110603.15+472253.46	15.458	15.908	15.819 ± 0.023	16.149 ± 0.012
J110606.72+514002.37	17.638	17.87	17.825 ± 0.068	17.995 ± 0.020
J110631.93+505302.00	15.955	16.477	16.212 ± 0.028	16.704 ± 0.011
J110750.61+164011.57	17.441	17.754	17.726 ± 0.052	17.961 ± 0.037
J111205.50+630148.49	17.337	17.776	17.564 ± 0.050	17.963 ± 0.039
J111353.35+595322.80	17.915	18.208	18.112 ± 0.090	18.227 ± 0.056
J111356.47+131614.59	15.256	15.828	15.532 ± 0.020	15.940 ± 0.016
J111603.78+494343.90	15.524	16.132	15.847 ± 0.014	16.313 ± 0.008
J111859.80+535725.00	17.715	18.05	17.919 ± 0.063	18.198 ± 0.038
J112002.74+442828.32	18.604	18.639	18.825 ± 0.105	18.899 ± 0.074
J112013.68+485231.02	17.422	17.66	17.640 ± 0.045	17.745 ± 0.018
J112215.99+671145.90	14.364	14.981	14.547 ± 0.016	15.049 ± 0.011
J112254.17+620606.32	16.743	17.285	16.971 ± 0.037	17.361 ± 0.027
J112311.08+425830.55	17.668	17.84	17.777 ± 0.063	17.958 ± 0.043
J112432.14+405950.25	17.004	17.335	17.332 ± 0.049	17.541 ± 0.034

Table 2.B.1 (cont'd)

Star	Synthetic FUV mag	Synthetic NUV mag	Observed FUV mag	Observed NUV mag
J112531.09+570406.11	17.468	17.65	17.793 ± 0.049	17.768 ± 0.029
J112613.52−002109.70	17.418	17.662	17.600 ± 0.053	17.859 ± 0.038
J112627.62+240903.80	16.63	17.049	17.036 ± 0.052	17.334 ± 0.033
J112729.52+672230.80	17.094	17.392	17.148 ± 0.046	17.427 ± 0.024
J112740.90−024638.80	16.346	16.752	16.777 ± 0.043	17.094 ± 0.029
J112815.61+171408.90	14.404	15.074	14.703 ± 0.018	15.345 ± 0.012
J112905.44+092327.85	17.073	17.375	17.493 ± 0.048	17.714 ± 0.034
J113027.71+450558.62	16.971	17.28	17.114 ± 0.030	17.422 ± 0.020
J113118.07+573937.39	17.643	17.808	17.986 ± 0.078	18.097 ± 0.051
J113205.55+370847.36	16.119	16.658	16.320 ± 0.022	16.753 ± 0.015
J113251.95+223356.46	17.004	17.461	17.352 ± 0.056	17.679 ± 0.041
J113254.32+460714.34	17.977	18.184	18.276 ± 0.089	18.459 ± 0.042
WD1131+315	16.701	17.125	16.893 ± 0.047	17.417 ± 0.037
J113652.75+145448.02	17.245	17.404	17.902 ± 0.069	17.802 ± 0.044
J113934.58+332515.10	16.342	16.851	16.638 ± 0.040	16.939 ± 0.029
J114033.35+453644.30	17.577	17.811	17.812 ± 0.073	18.036 ± 0.042
J114404.71+052951.40	16.273	16.671	16.534 ± 0.031	16.886 ± 0.024
J114551.39+101508.40	16.085	16.593	16.473 ± 0.033	16.899 ± 0.026
J115317.34+191152.80	14.58	15.24	15.024 ± 0.021	15.652 ± 0.014
J115446.94+265740.10	15.996	16.503	16.34 ± 0.031	16.717 ± 0.024
J115552.00+184914.66	16.89	17.359	17.235 ± 0.060	17.520 ± 0.024
J115632.07+113848.70	17.116	17.465	17.411 ± 0.051	17.652 ± 0.039
J115712.38+125239.72	17.568	17.803	17.992 ± 0.082	17.986 ± 0.041
J115804.65+595902.13	18.188	18.437	18.486 ± 0.096	18.58 ± 0.066
J120226.21+300035.10	16.64	17.139	16.996 ± 0.046	17.336 ± 0.036
J120621.23+464122.80	16.233	16.71	16.439 ± 0.033	16.914 ± 0.026
J120715.23+105338.33	17.379	17.738	17.860 ± 0.069	18.048 ± 0.047
J120924.26+095256.60	15.455	16.045	15.777 ± 0.027	16.278 ± 0.021
J121235.73+085449.25	17.908	18.145	18.152 ± 0.089	18.268 ± 0.060
J121756.20+021046.50	14.484	15.165	14.697 ± 0.013	15.319 ± 0.011
J122221.95+171539.40	16.511	16.984	16.774 ± 0.038	17.177 ± 0.031
J122452.26+435531.74	17.818	17.974	17.977 ± 0.084	18.097 ± 0.045
J122638.84+175201.45	16.378	16.788	16.716 ± 0.039	17.055 ± 0.028
J122722.85+021507.50	15.652	16.212	15.987 ± 0.031	16.417 ± 0.021
J122748.80+195548.32	17.223	17.543	17.777 ± 0.081	18.044 ± 0.049
J123004.20+085616.58	18.616	18.81	18.738 ± 0.113	19.033 ± 0.089

Table 2.B.1 (cont'd)

Star	Synthetic FUV mag	Synthetic NUV mag	Observed FUV mag	Observed NUV mag
J123531.70+643734.70	16.59	17.128	16.879 ± 0.052	17.403 ± 0.035
J123549.89+154319.30	16.744	17.009	17.042 ± 0.057	17.337 ± 0.034
J123602.42+664445.21	18.01	18.181	18.108 ± 0.076	18.333 ± 0.057
J123647.46+560438.86	17.038	17.435	17.190 ± 0.034	17.45 ± 0.025
J123723.82+051009.00	16.467	16.983	16.809 ± 0.031	17.282 ± 0.024
J123846.73+170620.80	15.647	16.207	15.853 ± 0.026	16.490 ± 0.022
J123925.55+450803.32	18.613	18.704	18.918 ± 0.118	19.057 ± 0.089
J124038.83+152859.99	16.584	17.016	16.763 ± 0.041	17.187 ± 0.029
J124337.74+302921.40	16.532	16.969	16.620 ± 0.023	16.994 ± 0.015
J124352.76+083616.52	18.026	18.127	18.318 ± 0.078	18.388 ± 0.042
J124407.67+582351.90	15.275	15.834	15.434 ± 0.020	15.961 ± 0.009
J124435.66−075304.70	17.115	17.457	17.373 ± 0.036	17.650 ± 0.028
J124506.95+601019.30	14.106	14.812	14.047 ± 0.012	14.659 ± 0.009
J124838.42+681327.48	18.043	18.22	18.244 ± 0.086	18.385 ± 0.059
J124915.21+062052.94	15.784	16.362	16.001 ± 0.033	16.479 ± 0.013
J125400.30+581948.15	15.878	16.451	16.014 ± 0.027	16.505 ± 0.011
J125706.73+613507.95	17.162	17.569	17.565 ± 0.037	17.833 ± 0.018
J125721.07+192451.70	15.193	15.781	15.372 ± 0.020	15.918 ± 0.011
J125726.90+065834.70	16.329	16.795	16.646 ± 0.043	17.114 ± 0.017
J125943.88+680400.91	15.1	15.66	15.412 ± 0.024	15.880 ± 0.019
J130033.76+661600.83	14.559	15.116	14.690 ± 0.013	15.229 ± 0.011
J130052.13+192931.70	14.672	15.265	14.974 ± 0.019	15.462 ± 0.009
J130053.20+603628.50	18.891	18.936	19.113 ± 0.089	19.024 ± 0.043
J130215.21−000111.53	18.189	18.314	18.517 ± 0.052	18.490 ± 0.030
J130548.66+462135.55	16.742	17.23	16.876 ± 0.029	17.307 ± 0.024
J130846.75+493000.80	15.995	16.552	16.247 ± 0.020	16.669 ± 0.014
J130900.74−005434.30	17.284	17.576	17.624 ± 0.034	17.830 ± 0.023
J131154.92+425451.70	17.409	17.738	17.579 ± 0.048	17.875 ± 0.028
J131201.48+394827.90	17.993	17.996	18.393 ± 0.055	18.244 ± 0.038
J131208.13+514159.52	16.657	17.09	16.800 ± 0.045	17.266 ± 0.023
J131241.62+044609.05	18.01	18.19	18.555 ± 0.113	18.584 ± 0.058
J131336.81+145910.68	18.016	18.243	18.475 ± 0.089	18.466 ± 0.062
J131447.40+022558.30	17.321	17.647	17.730 ± 0.058	17.943 ± 0.043
J131454.53+525831.04	17.082	17.491	17.271 ± 0.047	17.676 ± 0.030
J131639.94+582651.51	18.042	18.212	18.310 ± 0.093	18.402 ± 0.039
J131730.94+041752.04	16.619	17.133	16.792 ± 0.042	17.377 ± 0.036

Table 2.B.1 (cont'd)

Star	Synthetic FUV mag	Synthetic NUV mag	Observed FUV mag	Observed NUV mag
J131737.68+102346.14	17.573	17.842	17.729 ± 0.045	17.969 ± 0.032
J131926.96+425923.09	16.766	17.288	17.092 ± 0.032	17.591 ± 0.026
J131930.11+241020.46	17.167	17.485	17.483 ± 0.051	17.647 ± 0.022
J132010.48+340249.90	16.238	16.795	16.369 ± 0.031	16.912 ± 0.025
J132033.41+303522.71	17.265	17.649	17.400 ± 0.071	17.766 ± 0.040
WD1320+645	14.845	15.359	15.007 ± 0.010	15.469 ± 0.006
J132324.13+293834.28	17.762	17.944	17.847 ± 0.064	18.040 ± 0.045
J132329.25+294622.57	17.052	17.379	17.202 ± 0.048	17.564 ± 0.036
J132331.18+105742.98	17.216	17.619	17.631 ± 0.071	17.866 ± 0.044
J132336.77+373711.68	18.536	18.63	18.526 ± 0.068	18.681 ± 0.044
J132537.21+012926.30	18.122	18.325	18.322 ± 0.080	18.553 ± 0.064
J132603.42+632706.86	16.878	17.434	17.255 ± 0.049	17.751 ± 0.020
J132615.83+170017.35	17.665	17.905	17.858 ± 0.063	18.050 ± 0.029
J132709.96+385723.69	17.208	17.474	17.216 ± 0.032	17.479 ± 0.021
J132747.10+303303.01	17.738	18.06	18.211 ± 0.081	18.267 ± 0.053
J132918.24+282324.25	17.18	17.566	17.247 ± 0.041	17.644 ± 0.029
J133137.06+010632.10	15.66	16.228	15.922 ± 0.027	16.431 ± 0.021
J133137.57+184354.40	15.084	15.644	15.181 ± 0.020	15.733 ± 0.015
J133154.09+354503.85	15.293	15.875	15.666 ± 0.031	16.069 ± 0.018
J133154.14+004119.57	15.939	16.516	16.288 ± 0.031	16.773 ± 0.027
J133207.33+665453.40	15.41	15.951	15.726 ± 0.029	16.110 ± 0.021
J133507.26+432923.97	17.457	17.683	17.521 ± 0.068	17.765 ± 0.043
WD1333+510	15.169	15.726	15.334 ± 0.025	15.785 ± 0.017
J133620.80+352325.10	15.045	15.733	15.256 ± 0.021	15.755 ± 0.015
J133631.48+200422.37	15.933	16.374	16.238 ± 0.032	16.532 ± 0.018
J133739.67+455833.25	16.493	17.023	16.588 ± 0.033	17.087 ± 0.027
J133756.50+081312.00	17.131	17.527	17.580 ± 0.053	17.928 ± 0.044
J133824.21+115430.40	15.576	16.143	15.841 ± 0.032	16.408 ± 0.016
J134142.53+661707.40	17.116	17.587	17.400 ± 0.057	17.784 ± 0.044
J134259.84+022209.62	16.988	17.227	17.359 ± 0.055	17.511 ± 0.036
J134422.63+271009.80	16.005	16.546	16.339 ± 0.036	16.765 ± 0.026
J134437.93+113340.40	16.559	17.02	16.986 ± 0.053	17.276 ± 0.023
J134501.72+151008.40	16.475	16.984	16.833 ± 0.041	17.250 ± 0.022
J134540.19+165611.30	15.884	16.426	16.14 ± 0.030	16.587 ± 0.016
J134739.43+265509.80	17.179	17.579	17.415 ± 0.064	17.805 ± 0.023
J134847.01+065124.90	15.656	16.167	15.994 ± 0.022	16.385 ± 0.012

Table 2.B.1 (cont'd)

Star	Synthetic FUV mag	Synthetic NUV mag	Observed FUV mag	Observed NUV mag
J134914.30+344241.72	17.731	17.982	17.893 ± 0.085	18.202 ± 0.061
J134920.68+273508.40	15.425	15.98	15.767 ± 0.025	16.146 ± 0.010
J135425.59+253508.59	16.119	16.551	16.408 ± 0.039	16.789 ± 0.020
J135451.44+253047.92	15.495	16.053	15.685 ± 0.027	16.221 ± 0.022
J135618.81+150847.94	18.241	18.359	18.842 ± 0.102	18.584 ± 0.041
J135647.65+014448.30	17.657	17.778	17.931 ± 0.067	18.023 ± 0.047
J135733.28+060757.90	16.794	17.225	17.126 ± 0.045	17.552 ± 0.036
J135734.71+280111.35	15.267	15.817	15.569 ± 0.031	16.006 ± 0.024
J135911.25+380659.04	17.339	17.629	17.438 ± 0.046	17.755 ± 0.031
J135942.49+310255.52	16.613	16.982	16.727 ± 0.040	17.149 ± 0.022
J135955.80+041113.24	17.933	18.102	18.441 ± 0.063	18.335 ± 0.031
J140008.90+145246.99	15.181	15.748	15.408 ± 0.019	15.852 ± 0.013
J140020.94+622809.47	16.932	17.276	17.079 ± 0.046	17.488 ± 0.036
J140159.50+163551.32	18.014	18.252	18.302 ± 0.076	18.436 ± 0.038
J140308.28+113255.43	16.091	16.559	16.338 ± 0.032	16.725 ± 0.017
J140327.76+002119.60	14.799	15.488	15.165 ± 0.024	15.680 ± 0.008
J140350.78+321859.80	15.44	16.003	15.644 ± 0.026	16.140 ± 0.020
J140402.74+363916.80	17.9	18.247	18.311 ± 0.131	18.656 ± 0.082
J140542.26+241243.20	17.114	17.507	17.596 ± 0.058	17.830 ± 0.025
J140623.02+273103.32	16.143	16.701	16.345 ± 0.047	16.840 ± 0.018
J140623.68+140529.26	17.098	17.36	17.360 ± 0.053	17.534 ± 0.027
J140642.21+363755.20	15.86	16.397	16.073 ± 0.041	16.525 ± 0.015
J140857.39+415213.80	15.572	16.124	15.789 ± 0.022	16.288 ± 0.020
J140949.89+362005.20	18.696	18.761	18.986 ± 0.157	18.943 ± 0.052
J141106.09+240208.59	16.528	16.944	17.054 ± 0.053	17.309 ± 0.021
J141229.65+590112.90	15.099	15.705	15.297 ± 0.019	15.777 ± 0.011
J141335.29+373907.20	19.206	19.079	19.466 ± 0.123	19.086 ± 0.070
J141340.17+371323.00	18.071	18.254	18.239 ± 0.105	18.378 ± 0.064
J141414.09+265346.60	16.293	16.789	16.322 ± 0.039	16.726 ± 0.030
J141631.38+274815.37	17.915	18.204	17.957 ± 0.094	18.360 ± 0.071
J141941.60+032244.08	18.356	18.487	18.783 ± 0.064	18.686 ± 0.035
J142113.03+274018.34	17.683	17.926	18.008 ± 0.097	18.109 ± 0.067
J142328.99+461106.20	17.748	18.071	17.904 ± 0.067	18.264 ± 0.054
J142509.50+461348.00	18.489	18.554	18.819 ± 0.098	18.846 ± 0.069
J142621.00+040009.86	18.019	18.177	18.275 ± 0.089	18.390 ± 0.040
J142752.24+145740.40	17.391	17.614	17.691 ± 0.066	17.718 ± 0.041

Table 2.B.1 (cont'd)

Star	Synthetic FUV mag	Synthetic NUV mag	Observed FUV mag	Observed NUV mag
WD1427+410	15.516	16.087	15.834 ± 0.028	16.248 ± 0.021
J143315.92+252853.10	15.646	16.091	15.995 ± 0.043	16.370 ± 0.032
J143345.68+311609.30	16.86	17.266	16.890 ± 0.053	17.336 ± 0.035
J143616.49+465547.10	17.561	17.883	17.667 ± 0.062	17.964 ± 0.046
J143801.04+010738.30	16.298	16.773	16.660 ± 0.023	17.142 ± 0.017
J143801.04+010738.30	16.298	16.773	16.660 ± 0.023	17.142 ± 0.017
J143812.99+123252.87	17.919	18.091	18.116 ± 0.079	18.266 ± 0.055
J143831.47+292319.40	16.564	17.061	16.742 ± 0.039	17.252 ± 0.034
J143901.42+113839.40	16.527	16.953	16.904 ± 0.044	17.251 ± 0.034
J143906.08−005102.56	17.423	17.751	17.971 ± 0.077	18.199 ± 0.048
J144208.86−002737.00	16.309	16.837	16.710 ± 0.035	17.152 ± 0.028
J144307.67+605111.20	17.221	17.533	17.437 ± 0.043	17.673 ± 0.026
J144711.77+140649.10	18.676	18.427	18.949 ± 0.110	18.735 ± 0.069
J144801.75+471500.55	17.614	17.977	18.012 ± 0.061	18.365 ± 0.044
J144823.68+444344.40	16.787	17.011	17.098 ± 0.036	17.230 ± 0.024
J145024.57+123840.85	17.443	17.721	17.728 ± 0.078	17.960 ± 0.052
J145101.86+620349.40	16.286	16.778	16.469 ± 0.037	16.962 ± 0.027
J145104.16+371541.87	18.163	18.352	18.567 ± 0.071	18.424 ± 0.043
J145350.14+234928.67	17.453	17.796	17.881 ± 0.081	18.197 ± 0.056
J145420.83+223658.18	16.727	17.192	17.323 ± 0.068	17.561 ± 0.051
J145726.29+364340.60	15.197	15.764	15.460 ± 0.016	15.939 ± 0.010
J145734.43+334952.20	16.456	16.975	16.776 ± 0.039	17.185 ± 0.018
J145802.94+411723.75	17.923	18.225	18.161 ± 0.075	18.358 ± 0.047
J145913.99+041146.50	16.798	17.194	17.202 ± 0.035	17.499 ± 0.025
J150050.71+040430.00	16.369	16.882	16.801 ± 0.031	17.248 ± 0.023
J150153.77+020304.14	17.012	17.357	17.428 ± 0.049	17.767 ± 0.034
J150204.71+423729.50	17.884	18.084	17.928 ± 0.053	18.031 ± 0.033
J150445.84+111641.09	17.199	17.478	17.651 ± 0.072	17.794 ± 0.049
J150501.20+074416.40	17.215	17.667	17.638 ± 0.076	17.925 ± 0.045
J150602.91+360731.58	17.925	18.19	18.186 ± 0.063	18.380 ± 0.039
J150820.73+524159.00	18.199	18.29	18.510 ± 0.056	18.434 ± 0.037
J150918.45+340044.60	16.597	16.976	16.945 ± 0.040	17.234 ± 0.025
J150928.51+462321.10	15.86	16.405	16.178 ± 0.025	16.616 ± 0.019
J150949.52+565002.08	17.848	18.068	18.121 ± 0.098	18.297 ± 0.054
J151139.63+453631.97	17.973	18.161	18.283 ± 0.069	18.399 ± 0.042
J151234.03+165832.88	16.39	16.913	16.671 ± 0.033	17.171 ± 0.027

Table 2.B.1 (cont'd)

Star	Synthetic FUV mag	Synthetic NUV mag	Observed FUV mag	Observed NUV mag
J151343.51+443436.30	16.052	16.492	16.216 ± 0.021	16.613 ± 0.012
J151531.23+340058.00	17.61	17.817	18.141 ± 0.079	18.151 ± 0.030
J151616.34+374912.06	17.147	17.513	17.436 ± 0.042	17.667 ± 0.027
J151622.01+355945.17	18.119	18.292	18.541 ± 0.081	18.537 ± 0.039
J151638.14+341201.20	16.894	17.394	17.365 ± 0.048	17.713 ± 0.026
J151732.48+425340.49	16.341	16.805	16.765 ± 0.035	17.071 ± 0.025
J151817.26+581923.20	16.733	17.105	16.907 ± 0.024	17.201 ± 0.021
J151949.00+190504.60	17.903	18.188	18.616 ± 0.081	18.874 ± 0.055
J152001.71+423855.00	16.952	17.428	17.416 ± 0.042	17.784 ± 0.034
J152035.38+235036.96	16.797	17.23	17.052 ± 0.057	17.564 ± 0.039
J152138.67+053333.98	16.903	17.257	17.152 ± 0.039	17.565 ± 0.033
J152139.00+103015.80	14.261	14.887	14.756 ± 0.011	15.236 ± 0.009
J152354.80+053941.30	16.566	16.968	16.988 ± 0.040	17.261 ± 0.027
J152408.24+550048.99	16.557	17.077	16.826 ± 0.052	17.206 ± 0.032
J152421.85+391952.40	17.122	17.506	17.446 ± 0.051	17.749 ± 0.028
J152447.44+493448.00	17.684	17.928	18.025 ± 0.075	18.090 ± 0.046
J152643.13+063149.94	16.571	17.046	16.934 ± 0.054	17.259 ± 0.033
J152724.61+070128.56	16.656	17.165	17.073 ± 0.054	17.561 ± 0.037
J152759.13+012406.19	14.903	15.464	15.236 ± 0.024	15.782 ± 0.017
J152800.53+361510.81	17.535	17.806	17.709 ± 0.057	17.984 ± 0.035
J152907.43+445330.66	16.832	17.243	17.169 ± 0.039	17.431 ± 0.029
J152957.97+573200.08	16.991	17.387	17.207 ± 0.050	17.467 ± 0.037
J153103.51+505133.00	17.038	17.499	17.322 ± 0.032	17.650 ± 0.025
J153331.97+383824.38	17.962	18.165	18.055 ± 0.051	18.258 ± 0.038
J153437.70−004719.30	15.775	16.315	16.419 ± 0.034	17.090 ± 0.019
J153647.76+081826.57	18.116	18.293	18.438 ± 0.078	18.679 ± 0.066
J153716.29+584802.73	18.234	18.368	18.288 ± 0.063	18.486 ± 0.044
J153931.54+000118.40	16.34	16.853	16.968 ± 0.032	17.448 ± 0.026
J154113.97+560843.54	17.608	17.962	18.034 ± 0.074	18.323 ± 0.054
J154254.21+061228.60	16.03	16.499	16.355 ± 0.023	16.836 ± 0.019
J154318.28+492240.70	15.368	15.943	15.714 ± 0.023	16.168 ± 0.012
J154406.51+384757.65	17.77	17.966	18.069 ± 0.055	18.176 ± 0.037
J154448.26+455039.10	15.399	15.99	15.576 ± 0.017	16.084 ± 0.012
J154456.80+451522.00	13.998	14.706	13.993 ± 0.011	14.708 ± 0.009
J154456.81+422620.70	16.813	17.297	17.042 ± 0.050	17.445 ± 0.035
J154601.39+021050.92	16.686	17.205	17.533 ± 0.055	18.066 ± 0.047

Table 2.B.1 (cont'd)

Star	Synthetic FUV mag	Synthetic NUV mag	Observed FUV mag	Observed NUV mag
J154640.62+334644.47	18.295	18.531	18.5 ± 0.051	18.841 ± 0.048
J154724.19+065522.80	17.237	17.637	17.673 ± 0.042	17.918 ± 0.033
J154746.78+245055.30	16.037	16.544	16.515 ± 0.030	16.952 ± 0.022
J154912.51+292338.80	18.229	18.46	18.542 ± 0.094	18.766 ± 0.033
J154922.17+334601.10	16.236	16.804	16.569 ± 0.033	17.088 ± 0.027
J154950.00+205043.40	15.273	15.836	15.781 ± 0.020	16.275 ± 0.012
J154950.06+215753.57	17.565	17.809	18.004 ± 0.068	18.233 ± 0.040
J155035.21+402558.60	13.712	14.326	14.015 ± 0.010	14.454 ± 0.008
J155108.25+454313.22	15.702	16.298	15.959 ± 0.022	16.436 ± 0.010
J155512.50+074554.22	17.245	17.586	17.442 ± 0.037	17.827 ± 0.022
J155552.40+172920.04	15.595	16.194	16.088 ± 0.020	16.597 ± 0.017
J155559.89+172008.23	17.201	17.547	17.655 ± 0.045	17.858 ± 0.031
J155920.38+264454.10	18.756	18.749	19.353 ± 0.162	19.113 ± 0.070
J160135.34+361439.80	16.976	17.325	17.264 ± 0.047	17.658 ± 0.036
J160215.04+491314.00	16.048	16.547	16.381 ± 0.025	16.757 ± 0.020
J160317.78+413308.96	16.74	17.252	16.955 ± 0.037	17.328 ± 0.017
J160442.26+032827.10	17.814	18.008	18.306 ± 0.080	18.607 ± 0.042
J160515.39+503137.96	17.112	17.35	17.114 ± 0.041	17.400 ± 0.023
J160550.54+060738.10	14.65	15.271	15.346 ± 0.020	15.780 ± 0.016
J160614.05+204253.80	16.77	17.1	17.466 ± 0.051	17.830 ± 0.024
J160631.60+250651.10	16.172	16.609	16.497 ± 0.028	17.030 ± 0.014
J160647.63+050605.00	17.379	17.756	17.905 ± 0.069	18.158 ± 0.051
J160647.64+050605.00	17.379	17.756	17.905 ± 0.069	18.158 ± 0.051
J160710.27+511829.20	16.826	17.331	17.179 ± 0.040	17.547 ± 0.025
J160905.16+285104.75	18.124	18.278	18.504 ± 0.095	18.581 ± 0.069
J161018.32+054237.60	18.698	18.788	19.033 ± 0.084	19.135 ± 0.059
J161117.52+401703.26	17.43	17.573	17.742 ± 0.081	17.608 ± 0.019
J161205.78+543455.85	15.152	15.704	15.407 ± 0.017	15.880 ± 0.008
J161226.56+425111.45	15.741	16.324	15.875 ± 0.021	16.373 ± 0.011
J161239.12+091548.90	16.554	16.996	16.776 ± 0.034	17.263 ± 0.024
J161333.44+103605.40	18.03	18.102	18.249 ± 0.071	18.484 ± 0.046
J161409.82+425226.22	16.756	17.14	16.725 ± 0.033	17.170 ± 0.016
J161432.10+185458.75	15.866	16.379	16.284 ± 0.041	16.758 ± 0.016
J161441.99+370548.20	14.745	15.45	15.082 ± 0.017	15.474 ± 0.013
J161500.81+034457.90	17.955	18.081	18.349 ± 0.060	18.507 ± 0.034
J161505.25+295512.94	17.404	17.817	17.733 ± 0.064	18.130 ± 0.029

Table 2.B.1 (cont'd)

Star	Synthetic FUV mag	Synthetic NUV mag	Observed FUV mag	Observed NUV mag
J161528.68+535152.54	18.101	18.362	18.374 ± 0.091	18.581 ± 0.031
J161547.53+361121.52	17.872	18.195	18.104 ± 0.061	18.337 ± 0.049
J161554.03+433840.42	17.994	18.247	18.171 ± 0.062	18.328 ± 0.029
J161613.10+252012.70	15.808	16.398	16.765 ± 0.038	17.161 ± 0.016
J161710.37+215413.50	18.454	18.525	19.215 ± 0.135	19.218 ± 0.062
J161722.83+252756.70	16.753	17.248	17.620 ± 0.051	17.937 ± 0.024
J161725.34+071838.27	17.791	18.044	18.214 ± 0.060	18.457 ± 0.042
J161756.73+532254.41	17.517	17.794	17.801 ± 0.048	18.073 ± 0.039
J161905.60+083333.40	16.551	16.986	17.055 ± 0.038	17.453 ± 0.020
J161928.28+365403.20	18.324	18.524	18.510 ± 0.056	18.583 ± 0.038
J161940.02+222958.30	14.661	15.212	15.251 ± 0.020	15.738 ± 0.015
J162005.04+114943.40	15.279	15.844	15.727 ± 0.025	16.224 ± 0.012
J162020.89+214542.98	15.808	16.291	16.163 ± 0.036	16.722 ± 0.025
J162024.41−000545.90	16.519	16.832	17.005 ± 0.024	17.424 ± 0.020
J162034.43+374347.35	17.367	17.665	17.678 ± 0.053	17.887 ± 0.023
J162106.46+434126.90	16.079	16.602	16.229 ± 0.028	16.688 ± 0.023
J162158.81+202402.09	17.021	17.489	17.556 ± 0.060	17.988 ± 0.032
J162301.57+303040.18	17.382	17.637	17.742 ± 0.060	17.867 ± 0.025
J162324.90−011123.80	17.511	17.714	17.792 ± 0.046	18.101 ± 0.036
J162746.83+631839.60	16.206	16.691	16.443 ± 0.027	16.838 ± 0.023
J162825.98+333450.60	16.321	16.822	16.702 ± 0.025	17.073 ± 0.023
J162912.30+375952.66	17.881	18.092	17.981 ± 0.063	18.175 ± 0.043
J163218.84+404618.90	16.847	17.356	17.069 ± 0.045	17.465 ± 0.024
J163328.05+233346.40	16.279	16.761	16.791 ± 0.044	17.074 ± 0.018
J163336.71+140629.30	18.222	18.415	18.744 ± 0.091	18.89 ± 0.061
J163338.87+303041.90	17.755	18.015	18.165 ± 0.089	18.003 ± 0.047
J163348.91+323616.34	18.532	18.623	18.647 ± 0.084	18.750 ± 0.047
J163351.20+294504.43	16.902	17.411	17.39 ± 0.053	17.745 ± 0.021
J163453.38+182758.90	18.783	18.814	19.158 ± 0.106	19.226 ± 0.049
J163511.64+111849.90	16.125	16.692	16.805 ± 0.030	17.332 ± 0.018
J163524.38+444349.80	17.289	17.801	17.698 ± 0.056	17.978 ± 0.043
J163559.97+464154.75	18.46	18.631	18.602 ± 0.070	18.792 ± 0.039
J163609.00+560135.00	16.753	17.247	17.094 ± 0.043	17.443 ± 0.030
J163659.28+354519.80	17.537	17.864	17.731 ± 0.058	18.078 ± 0.045
J163920.38+201638.75	17.573	17.956	18.195 ± 0.068	18.386 ± 0.047
J163936.15+474312.36	17.368	17.587	17.377 ± 0.039	17.583 ± 0.024

Table 2.B.1 (cont'd)

Star	Synthetic FUV mag	Synthetic NUV mag	Observed FUV mag	Observed NUV mag
J163939.51+480655.25	16.64	16.963	16.815 ± 0.037	17.140 ± 0.027
J163944.64+383346.84	15.857	16.391	16.057 ± 0.026	16.492 ± 0.021
J164205.63+405330.70	17.621	17.861	17.788 ± 0.060	17.953 ± 0.031
J164224.69+231359.50	15.299	15.881	15.882 ± 0.022	16.404 ± 0.014
J164250.03+303716.25	19.202	19.043	19.453 ± 0.151	19.257 ± 0.074
J164255.17+393105.20	16.074	16.571	16.335 ± 0.029	16.716 ± 0.020
J164311.10+425000.74	18.163	18.289	18.231 ± 0.090	18.356 ± 0.036
J164407.41+303143.07	16.442	16.926	16.661 ± 0.041	17.096 ± 0.025
J164418.87+384230.70	17.274	17.532	17.483 ± 0.052	17.661 ± 0.038
J164424.24+382830.61	14.439	15.032	14.600 ± 0.013	15.108 ± 0.011
J164448.07+293059.36	18.422	18.621	18.651 ± 0.099	18.893 ± 0.054
J164631.11+445315.18	18.166	18.414	18.366 ± 0.078	18.518 ± 0.054
J164741.53+195746.94	18.088	18.329	18.440 ± 0.067	18.814 ± 0.052
J164812.58+331154.17	17.92	18.189	18.134 ± 0.075	18.284 ± 0.053
J164936.08+263016.70	17.194	17.605	18.106 ± 0.069	18.214 ± 0.036
J164936.63+450941.76	17.418	17.776	17.509 ± 0.075	17.828 ± 0.046
J164947.18+262409.50	15.011	15.627	15.965 ± 0.017	16.421 ± 0.016
J164950.07+312421.64	18.335	18.523	18.514 ± 0.082	18.703 ± 0.056
J164952.57+222334.12	18.269	18.454	18.504 ± 0.075	18.711 ± 0.031
J165128.84+633438.30	18.445	18.431	18.645 ± 0.072	18.546 ± 0.044
J165148.75+261531.00	15.372	15.935	16.302 ± 0.021	16.626 ± 0.018
J165228.26+232735.00	17.17	17.618	17.526 ± 0.061	18.000 ± 0.026
J165249.28+384123.18	14.496	15.084	14.698 ± 0.014	15.242 ± 0.008
J165337.76+181322.26	18.212	18.467	18.667 ± 0.093	18.926 ± 0.055
J165424.17+171539.02	17.571	17.879	18.031 ± 0.055	18.445 ± 0.046
J165449.68+402325.10	18.515	18.662	18.734 ± 0.106	18.834 ± 0.069
J165534.64+123347.20	17.489	17.747	17.918 ± 0.052	18.154 ± 0.036
J165657.05+403828.30	15.801	16.305	15.934 ± 0.026	16.401 ± 0.021
WD1655+210	14.705	15.265	15.037 ± 0.018	15.558 ± 0.012
J165812.62+382042.60	17.003	17.373	17.163 ± 0.048	17.472 ± 0.026
J165817.76+291024.80	18.999	18.919	19.404 ± 0.213	19.167 ± 0.088
J165818.04+404139.00	19.075	18.923	18.900 ± 0.108	18.808 ± 0.068
J165826.66+363341.17	17.423	17.83	17.741 ± 0.058	18.079 ± 0.045
J165828.47+445314.78	16.94	17.194	17.055 ± 0.056	17.293 ± 0.034
J165851.11+341853.30	14.197	14.834	14.600 ± 0.011	15.006 ± 0.006
J165929.07+263539.00	16.561	16.898	16.843 ± 0.033	17.118 ± 0.023

Table 2.B.1 (cont'd)

Star	Synthetic FUV mag	Synthetic NUV mag	Observed FUV mag	Observed NUV mag
J165944.10+454557.74	15.612	16.242	15.782 ± 0.025	16.372 ± 0.023
J170057.08+260359.80	17.564	17.898	17.943 ± 0.049	18.265 ± 0.038
J170130.92+283028.30	17.756	17.979	18.055 ± 0.072	18.110 ± 0.049
J170330.99+272850.80	16.106	16.65	16.616 ± 0.041	17.043 ± 0.031
J170356.56+281323.20	17.134	17.442	17.664 ± 0.074	17.843 ± 0.042
J170447.08+400458.80	17.624	17.992	17.823 ± 0.065	18.174 ± 0.034
J170510.23+385357.40	16.989	17.441	17.267 ± 0.048	17.759 ± 0.042
J170530.82+271523.30	15.168	15.793	15.746 ± 0.028	16.215 ± 0.017
J170537.75+423346.48	16.073	16.437	16.118 ± 0.031	16.477 ± 0.018
J170843.51+274921.00	16.497	17.039	17.638 ± 0.056	17.854 ± 0.039
J170927.83+231020.70	17.774	17.844	18.092 ± 0.063	17.958 ± 0.041
J171118.78+371021.70	17.25	17.651	17.371 ± 0.045	17.854 ± 0.041
J171125.53+272405.15	15.198	15.814	15.776 ± 0.024	16.221 ± 0.020
J171306.73+565525.60	17.118	17.465	17.410 ± 0.061	17.727 ± 0.045
J171438.40+394539.40	18.05	18.337	18.377 ± 0.105	18.752 ± 0.068
J171536.37+363040.32	17.715	17.911	17.850 ± 0.050	18.088 ± 0.039
J172645.53+264227.30	17.388	17.712	17.674 ± 0.052	17.894 ± 0.037
J173117.84+312302.04	18.357	18.564	18.765 ± 0.085	18.774 ± 0.061
J173133.30+330804.30	18.271	18.44	18.566 ± 0.083	18.605 ± 0.037
J173217.07+640716.90	16.573	17.056	16.808 ± 0.035	17.177 ± 0.025
J173455.32+650823.50	16.318	16.877	16.679 ± 0.031	17.169 ± 0.025
J173842.24+645534.30	15.902	16.453	16.208 ± 0.022	16.688 ± 0.018
J181424.14+785403.00	14.787	15.35	15.127 ± 0.012	15.570 ± 0.011
J192808.84+623438.10	18.241	18.368	18.269 ± 0.072	18.400 ± 0.053
J193659.11+624921.40	17.623	17.929	17.875 ± 0.059	18.244 ± 0.047
J202253.35+141153.10	15.084	15.745	15.801 ± 0.019	16.395 ± 0.016
J204331.23+001119.90	17.112	17.461	17.506 ± 0.050	17.845 ± 0.037
J204410.84+004515.30	17.077	17.484	17.346 ± 0.036	17.789 ± 0.029
J204421.19−051856.00	18.424	18.482	18.537 ± 0.077	18.512 ± 0.048
J204533.11+153307.70	16.731	17.06	17.210 ± 0.036	17.506 ± 0.030
J205059.51+012146.90	15.973	16.495	16.348 ± 0.022	16.950 ± 0.016
J205440.40+154816.50	15.903	16.468	16.389 ± 0.026	16.871 ± 0.023
J210928.33−053843.20	15.403	15.97	16.145 ± 0.014	16.605 ± 0.012
J211229.48−064051.80	15.699	16.208	16.262 ± 0.020	16.732 ± 0.017
J211607.27+004503.17	17.735	18.082	20.175 ± 0.188	18.491 ± 0.055
J212411.99−072648.70	15.644	16.331	14.224 ± 0.012	14.764 ± 0.008

Table 2.B.1 (cont'd)

Star	Synthetic FUV mag	Synthetic NUV mag	Observed FUV mag	Observed NUV mag
J213225.88+005428.91	17.577	17.827	17.832 ± 0.051	18.125 ± 0.037
J214903.12+054704.81	16.965	17.369	17.703 ± 0.039	18.150 ± 0.033
J223405.82+232510.99	15.421	15.982	15.702 ± 0.020	16.277 ± 0.015
J223558.35+133140.60	18.305	18.348	18.739 ± 0.110	18.618 ± 0.065
J225247.41+270433.79	17.523	17.776	17.725 ± 0.043	18.052 ± 0.031
J230255.02−084005.70	14.303	14.97	14.654 ± 0.011	15.233 ± 0.010
J231340.86+063527.41	18.524	18.503	18.947 ± 0.057	19.094 ± 0.042
J231640.19−010951.62	17.361	17.817	18.154 ± 0.077	18.405 ± 0.058
J232230.96+152258.95	17.735	18.049	18.341 ± 0.060	18.505 ± 0.042
J233157.66+144345.75	17.607	17.856	18.063 ± 0.047	18.308 ± 0.030
WD2331+290	13.881	14.42	14.370 ± 0.012	14.837 ± 0.004
J234528.67+394643.80	15.079	15.643	15.695 ± 0.013	16.236 ± 0.013
J234733.92+440241.50	16.615	17.026	16.835 ± 0.030	17.267 ± 0.023
J234738.64+423620.80	16.182	16.685	16.892 ± 0.029	17.302 ± 0.023
J235148.35+362011.10	16.624	16.986	17.007 ± 0.032	17.391 ± 0.026
J235315.25+153640.40	18.167	18.24	18.423 ± 0.049	18.510 ± 0.025
J235353.61+355725.40	18.1	18.19	18.415 ± 0.076	18.558 ± 0.047

CHAPTER 3

A GALEX view of the DA White Dwarf Population

3.1. Introduction

Prior to *Gaia*, the majority of the white dwarfs in the solar neighborhood were identified through Sloan Digital Sky Survey spectroscopy, which specifically targeted hot and blue white dwarfs as flux standards (e.g., Kleinman et al., 2013). Many of the SDSS white dwarfs have spectral energy distributions that peak in the UV. Hence, GALEX FUV and NUV data can help constrain the physical parameters of these white dwarfs. GALEX data will also be useful for cooler white dwarfs; UV photometry will be used to confirm the temperature derived from the optical data, or to constrain the far red wing of the Lyman α line that dominates the opacity in the blue part of the spectral energy distribution of cool hydrogen atmosphere white dwarfs (Kowalski & Saumon, 2006). Yet, GALEX data are under-utilized in the analysis of white dwarfs in the literature, perhaps due to the relatively strong extinction observed in the UV.

Wall et al. (2019) used 1837 DA white dwarfs with high signal to noise ratio spectra and *Gaia* parallaxes to verify the absolute calibration of the FUV and NUV data, and refined the linearity corrections derived by Camarota & Holberg (2014). They also empirically derived extinction coefficients for both bands, finding $R_{\rm FUV} = 8.01$ and $R_{\rm NUV} = 6.72$, where R is the ratio of the total absorption A_λ to reddening $E(B-V)$ along the line of sight to an object. Wall et al. (2019) highlighted the utility of their newly derived extinction coefficients for identifying white dwarfs with unusual UV photometry. By comparing the observed GALEX magnitudes to predictions from the model atmosphere calculations, they found 12 outliers in the UV, seven of which were previously known, including three double degenerates, two white dwarf + main-sequence star binaries, one ZZ Ceti, and one double degenerate candidate (see chapter 2).

Lajoie & Bergeron (2007) compared the effective temperatures obtained from the optical and UV spectra of 140 DA white dwarfs from the *IUE* archive. They found that the optical and UV temperatures of the majority of stars cooler than 40000 K and within 75 pc are in fairly good agreement with $\Delta T_{\rm eff}/T_{\rm optical} \leq 10\%$. They also found that the majority of the discrepancies between the two temperature measurements were caused by interstellar reddening, which affects the UV more than the optical. By restricting their analysis to white dwarfs within 75 pc, where the extinction is negligible, they were able to identify several double degenerate candidates, as well as a DA + M dwarf system, and stars with unusual atmospheric compositions. Lajoie & Bergeron (2007) thus demonstrated that unusual white dwarfs can be identified by comparing temperatures

derived solely from optical data and UV data.

In this work, we expand the analysis of optical and UV temperature measurements to the DA white dwarfs in the Montreal White Dwarf Database (MWDD) aided by GALEX UV data and *Gaia* Data Release 3 astrometry. To identify unusual white dwarfs, we use two methods. First, we compare the UV and optical temperatures in a manner similar to Lajoie & Bergeron (2007). We refer to this as the temperature comparison method. Our second method follows the analysis of Wall et al. (2019) and compares the observed and predicted GALEX magnitudes. We refer to this as the magnitude comparison method.

We provide the details of our sample selection in Section 3.2, the model atmosphere fitting procedure in Section 3.3, and the results from the temperature comparison method for the 100 pc sample and the entire MWDD sample in Section 3.4. Section 3.5 presents the results from the magnitude comparison method. We conclude in Section 3.6.

3.2. Sample Selection

We started with all spectroscopically confirmed DA white dwarfs from the Montreal White Dwarf Database (Dufour et al., 2017) using the September 2022 version of the database. This sample includes over 30000 stars. We removed known white dwarf + main-sequence binaries and variables from the sample. We then collected the SDSS and Pan-STARRS1 photometry using the cross-match tables provided by *Gaia* DR3. We found 25840 DA white dwarfs with *Gaia* astrometry and Pan-STARRS1 photometry, 20898 of which are also detected in the SDSS.

Gaia DR3 does not provide a cross-matched catalog with GALEX, which performed its all-sky imaging survey between 2003 and 2009. The reference epoch for the *Gaia* DR3 positions is 2016. Assuming a 10 year baseline between the GALEX mission and *Gaia* DR3, we propagated the *Gaia* DR3 positions to the GALEX epoch using *Gaia* proper motions. We then cross-referenced our sample with the GALEX catalogue of unique UV sources from the all-sky imaging survey (GUVcat) presented in Bianchi et al. (2017). We used a cross-match radius of 3 arcseconds with GUVcat. We found 18456 DA white dwarfs with GALEX data.

Some of the DA white dwarfs in our sample are bright enough to be saturated in Pan-STARRS, SDSS, or GALEX. The saturation occurs at $g, r, i \sim 13.5$, $z \sim 13$, and $y \sim 12$ mag in Pan-STARRS (Magnier et al., 2013). We remove objects brighter than these limits. To make sure that there are at least three optical filters available for our model fits, we limit our sample to objects with at least Pan-STARRS g, r, i photometry available.

We apply the linearity corrections for the GALEX FUV and NUV bands as measured by Wall et al. (2019). These corrections are ≥ 0.5 mag for FUV and NUV magnitudes brighter than 13th mag. To avoid issues with saturation and large linearity corrections in the GALEX bands, we further remove objects with FUV and NUV magnitudes brighter than that limit. We further limit our sample

to objects with a 3σ significant distance measurement (Bailer-Jones et al., 2021) so that we can reliably constrain the radii (and therefore mass and surface gravity) of the stars in our sample. Our final sample contains 14001 DA white dwarfs with photometry in at least one of the GALEX filters and the Pan-STARRS gri filters. However, more than half of the stars in our final selection, 7574 of them, have GALEX FUV, NUV, SDSS u, and Pan-STARRS $gri(zy)$ photometry available.

3.3. The Fitting Procedure

We use the photometric technique as detailed in Bergeron et al. (2019), and perform two sets of fits; 1) using only the optical data, and 2) using both the optical and the UV data. In the first set of fits we use the SDSS u (if available) along with the Pan-STARRS $grizy$ photometry to model the spectral energy distribution of each DA white dwarf, and in the second set of fits we add the GALEX FUV (if available) and NUV data.

We correct the SDSS u magnitude to the AB magnitude system using the corrections provided by Eisenstein et al. (2006). For the reasons outlined in Bergeron et al. (2019), we adopt a lower limit of 0.03 mag uncertainty in all bandpasses, and use the de-reddening procedure outlined in Harris et al. (2006) where the extinction is assumed to be zero for stars within 100 pc, to be maximum for those located at distances 250 pc away from the Galactic plane, and to vary linearly along the line of sight between these two regimes.

We convert the observed magnitudes into average fluxes using the appropriate zero points, and compare with the average synthetic fluxes calculated from pure hydrogen atmosphere models. We define a χ^2 value in terms of the difference between observed and model fluxes over all bandpasses, properly weighted by the photometric uncertainties, which is then minimized using the nonlinear least-squares method of Levenberg-Marquardt (Press et al., 1986) to obtain the best fitting parameters. We obtain the uncertainties of each fitted parameter directly from the covariance matrix of the fitting algorithm, while we calculate the uncertainties for all other quantities derived from these parameters by propagating in quadrature the appropriate measurement errors.

We fit for the effective temperature and the solid angle, $\pi(R/D)^2$, where R is the radius of the star and D is its distance. Since the distance is known from *Gaia* parallaxes, we constrain the radius of the star directly, and therefore the mass based on the evolutionary models for white dwarfs. The details of our fitting method, including the model grids used are further discussed in Bergeron et al. (2019) and Genest-Beaulieu & Bergeron (2019).

3.4. Results from Temperature Comparison

3.4.1. The 100 pc SDSS Sample

We use the 100 pc white dwarf sample in the SDSS footprint to test if the temperatures obtained from the optical and the UV data agree, and also to test the feasibility of identifying UV-excess or

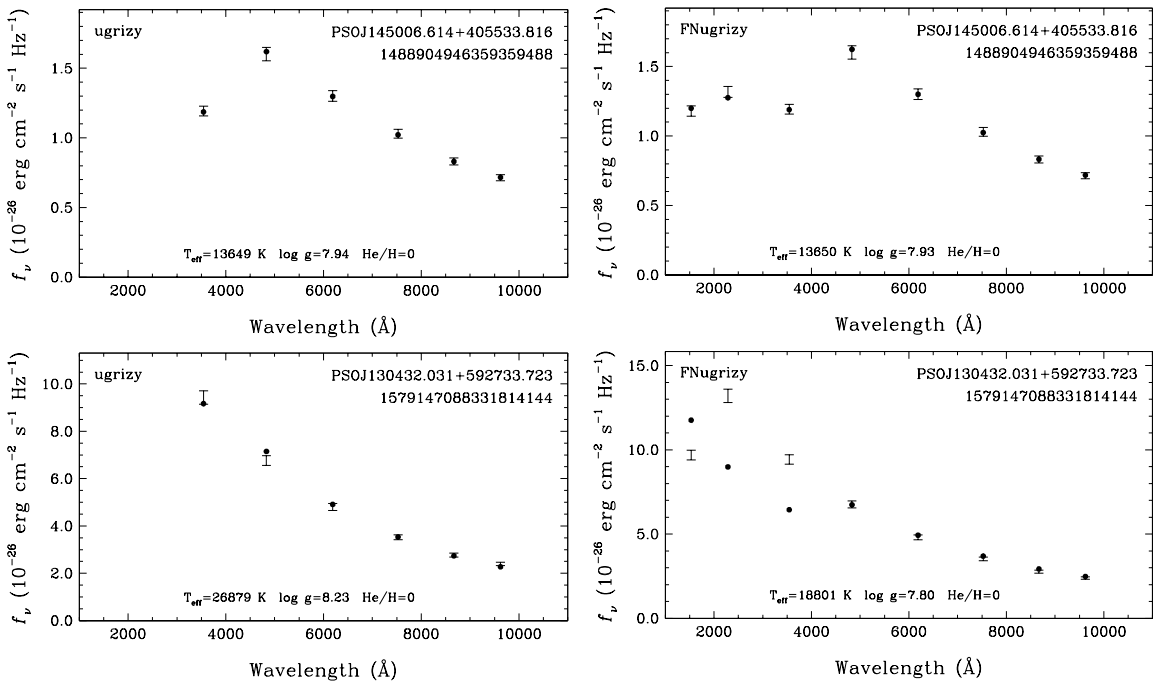

Figure 3.4.1: *Top:* Model fits to WD 1448+411, a spectroscopically confirmed DA white dwarf in the 100 pc SDSS sample. Each panel shows the best-fitting pure hydrogen atmosphere white dwarf model (filled dots) to the photometry (error bars). The labels in each panel include the Pan-STARRS coordinates, the *Gaia* DR3 Source ID, and the photometry used in the fitting: $FNugrizy$ means GALEX FUV + NUV + SDSS u + Pan-STARRS $grizy$. The left panel shows the model fits based on the optical data only, whereas the right panel shows the fit using both optical and the UV data. The best-fitting model parameters are given in each panel. *Bottom:* Model fits to GD 323 (WD 1302+597), a spectroscopically confirmed DAB white dwarf, assuming a pure H atmosphere.

UV-deficit objects. Kilic et al. (2020) presented a detailed model atmosphere analysis of the 100 pc white dwarf sample in the SDSS footprint and identified 1508 DA white dwarfs. Cross-matching this sample with GUVcat (Bianchi et al., 2017), we find 847 DA white dwarfs with GALEX data; 377 have both FUV and NUV photometry available, while 470 have only NUV data available.

The top panels in Figure 3.4.1 show our fits for WD 1448+411, a spectroscopically confirmed DA white dwarf (Gianninas et al., 2011) in the 100 pc SDSS sample. The top left panel shows the SDSS u and Pan-STARRS $grizy$ photometry (error bars) along with the predicted fluxes from the best-fitting pure hydrogen atmosphere model (filled dots). The labels in the same panel give the Pan-STARRS coordinates, *Gaia* DR3 Source ID, and the photometry used in the fitting. The top right panel shows the same model fits, but with the addition of the GALEX FUV and NUV photometry. The temperature and surface gravity estimates from both sets of fits, based on either the optical data only (left panel) or a combination of the optical and UV data (right panel), agree remarkably well for this star. Hence, the spectral energy distribution of WD 1448+411 in the 0.1-1 μm range is consistent with an isolated pure hydrogen atmosphere white dwarf.

The bottom panels in Figure 3.4.1 show the model fits for another white dwarf in the 100 pc SDSS sample. GD 323 (WD 1302+597) is a spectroscopically confirmed DAB white dwarf (Wesemael et al., 1993). The use of pure hydrogen atmosphere models to fit its spectral energy distribution is obviously inappropriate. However, we use GD 323 to demonstrate how fitting the UV to optical spectral energy distribution can reveal object with unusual atmospheric composition. The bottom left panel in Figure 3.4.1 shows our model fits using only the optical data from the SDSS and Pan-STARRS. Assuming a pure hydrogen composition, GD 323 would have the best-fitting $T_{\rm eff} = 26879 \pm 1310$ K and $\log g = 8.230 \pm 0.047$. This solution provides an excellent match to the optical photometry. The bottom right panel shows the same model fits with the addition of the GALEX FUV and NUV data. The best-fitting model parameters are significantly different, and clearly the pure hydrogen atmosphere models cannot match the UV portion of the spectral energy distribution of GD 323. Hence, a comparison between the two sets of model fits based on optical and/or UV data has the potential to identify DAB or other types of unusual objects among the DA white dwarf population in the solar neighborhood.

Figure 3.4.2 shows a comparison between the model fits using optical data only versus a combination of the optical + UV data for the DA white dwarfs in the 100 pc SDSS sample. Blue dots and red triangles mark the magnetic and DAB white dwarfs, respectively. The majority of the objects in this figure fall very close to the 1:1 line, shown in red, confirming that they are consistent with pure hydrogen atmosphere white dwarfs.

Excluding the five significant outliers labeled in the figure, the effective temperature and $\log g$ derived from the GALEX+optical data are slightly higher than the values obtained from the optical data only by 50^{+215}_{-71} K and $0.01^{+0.04}_{-0.01}$ dex, respectively. Hence, there are no major systematic

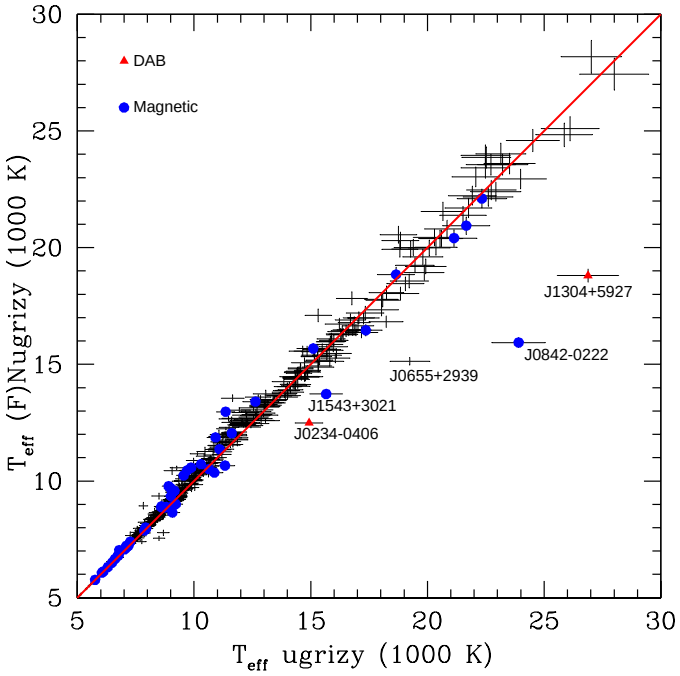

Figure 3.4.2: A comparison between the effective temperature derived from optical only data versus a combination of the UV and optical data for the DA white dwarfs in the 100 pc SDSS ∩ GALEX sample. Unusual objects, magnetic DAH and mixed composition DAB white dwarfs, are labeled with blue dots and red triangles, respectively.

differences between the best-fit parameters derived from optical only data and the optical + UV photometry. However, the addition of the GALEX FUV and NUV data helps improve the statistical errors in the model fits, especially for the hotter white dwarfs where the spectral energy distribution peaks in the UV. For example, for white dwarfs with $T_{\rm eff} < 10000$ K, the statistical errors in optical + UV temperature estimates are on average better by a factor of 1.3 compared to the errors based on the optical data only, but they are better by a factor of 2.5 for $T_{\rm eff} > 15000$ K.

The five significant outliers in Figure 3.4.2 all appear to be fainter than expected in the UV, and that is why their best-fitting temperatures based on the optical + UV model fits are cooler than those based on the optical data. These outliers include two DA white dwarfs with unusual atmospheric composition. J1304+5927 (GD 323, see Figure 3.4.1) and J0234−0406 (PSO J038.5646−04.1025). The latter was originally classified as a DA white dwarf based on a low-resolution spectrum obtained by Kilic et al. (2020). Higher signal-to-noise ratio follow-up spectroscopy by Gentile Fusillo et al. (2021) demonstrated that J0234−0406 is in fact a DABZ white dwarf that hosts a gaseous debris disk. Even though its spectral appearance is visually dominated by broad Balmer absorption lines, the atmosphere of J0234−0406 is actually dominated by helium, and that is why it is an outlier in Figure 3.4.2.

J0842−0222 (PSO J130.5623−02.3741) and J1543+3021 (PSO J235.8127+30.3595) are both

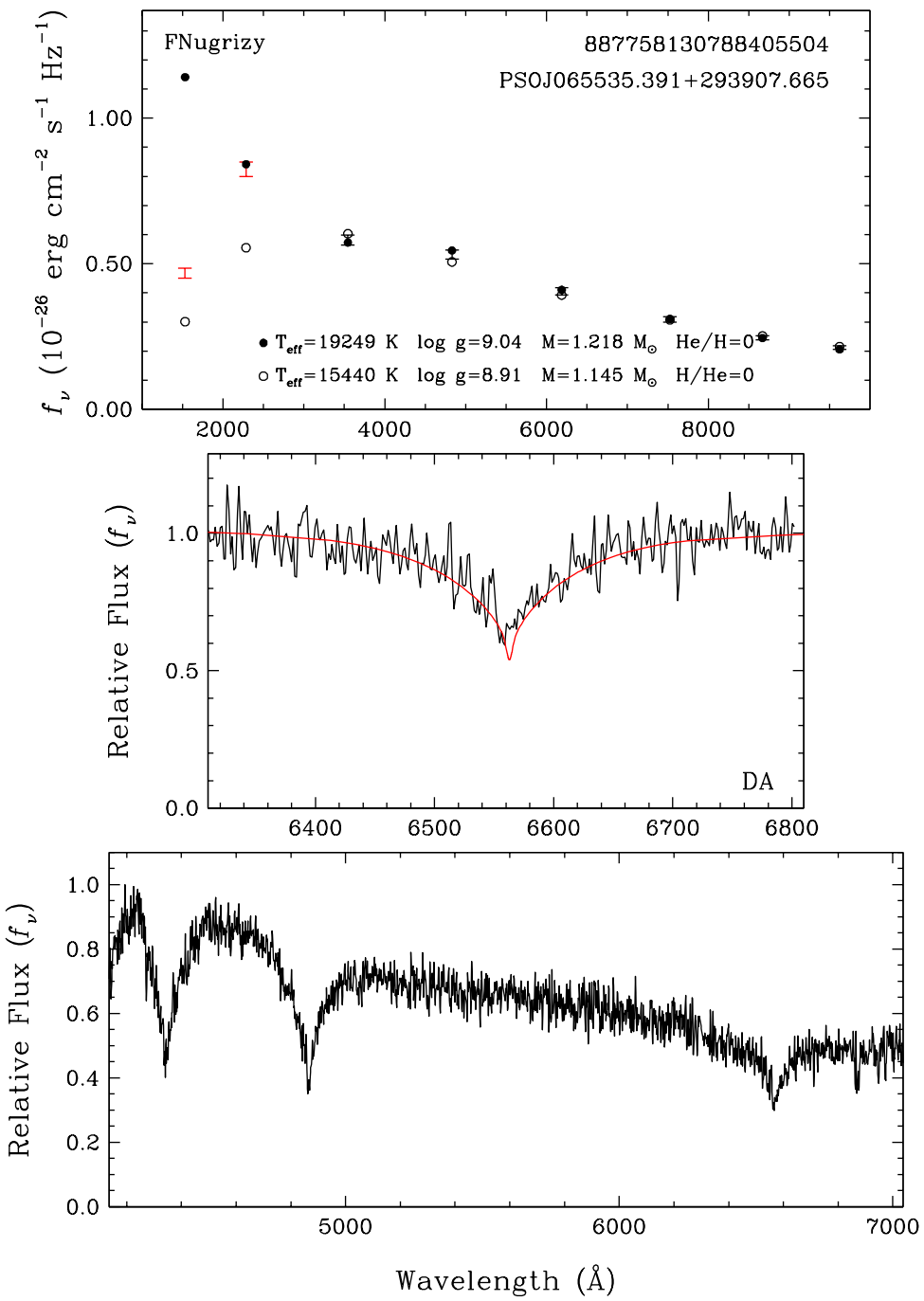

Figure 3.4.3: Model atmosphere fits to the DA white dwarf J0655+2939. The top panel shows the best-fitting H (filled dots) and He (open circles) atmosphere white dwarf models to the optical photometry (black error bars). The middle panel shows the observed spectrum (black line) along with the predicted spectrum (red line) based on the pure H atmosphere solution. The bottom panel shows a broader wavelength range.

strongly magnetic and massive white dwarfs with $M > 1.1\ M_{\odot}$ and unusual optical spectra. Schmidt et al. (1986) noted problems with fitting the UV and optical spectral energy distribution of the strongly magnetic white dwarf PG 1031+234 with a field stronger than 200 MG. They found that the IUE and optical/infrared fits cannot be reconciled and that there is no Balmer discontinuity in the spectrum of this object. They attribute this to the blanketing due to hydrogen lines being grossly different, and the addition of a strong opacity source (cyclotron absorption). GD 229 is another example of a magnetic white dwarf with inconsistent UV and optical temperature estimates (Green & Liebert, 1981). Out of the 51 magnetic white dwarfs shown in Figure 3.4.2, only J0842−0222 and J1543+3021 have significantly discrepant UV and optical temperatures. Hence, such inconsistencies seem to impact a fraction of the magnetic white dwarfs in the solar neighborhood.

Another outlier, J0655+2939 (PSO J103.8966+29.6527), is also a massive white dwarf with $M \sim 1.2\ M_{\odot}$. We obtained follow-up optical spectroscopy of J0655+2939 using the KOSMOS spectrograph on the APO 3.5m telescope on UT 2023 Jan 28. We used the blue grism in the high slit position with a $2.05''$ slit, providing wavelength coverage from 4150 Å to 7050 Å and a resolution of 1.42 Å per pixel in the 2×2 binned mode.

Figure 3.4.3 shows our model fits for J0655+2939. The top panel shows the best-fitting H (filled dots) and He (open circles) atmosphere white dwarf models to the optical photometry (black error bars). Note that the GALEX photometry (red error bars) are not used in these fits. The middle panel shows the observed spectrum (black line) along with the predicted spectrum (red line) based on the pure H atmosphere solution. The bottom panel shows the entire KOSMOS spectrum. We confirm J0655+2939 as a DA white dwarf. Even though its Balmer lines and the optical + NUV photometry agree with the pure H atmosphere solution, J0655+2939 is significantly fainter than expected in the GALEX FUV band. The source of this discrepancy is unclear, but the observed Hα line core is also slightly shallower than expected based on the pure H atmosphere model. This could indicate Zeeman splitting of the line core, but our low resolution spectrum does not permit a definitive interpretation of the source of discrepancy for this object.

3.4.2. The MWDD DA sample

The 100 pc SDSS DA white dwarf sample discussed in the previous section clearly demonstrates that 1) there are no large-scale systematic differences between the model fits using optical only data ($ugriz$) and a combination of optical + UV data, and 2) GALEX FUV and NUV data can be used to identify unusual DA white dwarfs with helium-rich atmospheres or strong magnetic fields. We now expand our study to the entire Montreal White Dwarf Database DA white dwarf sample in the Pan-STARRS ∩ GALEX footprint.

Figure 3.4.4 shows a comparison between the effective temperatures derived from optical and UV data for the DA white dwarfs in the SDSS footprint. The difference from Figure 3.4.2 is that

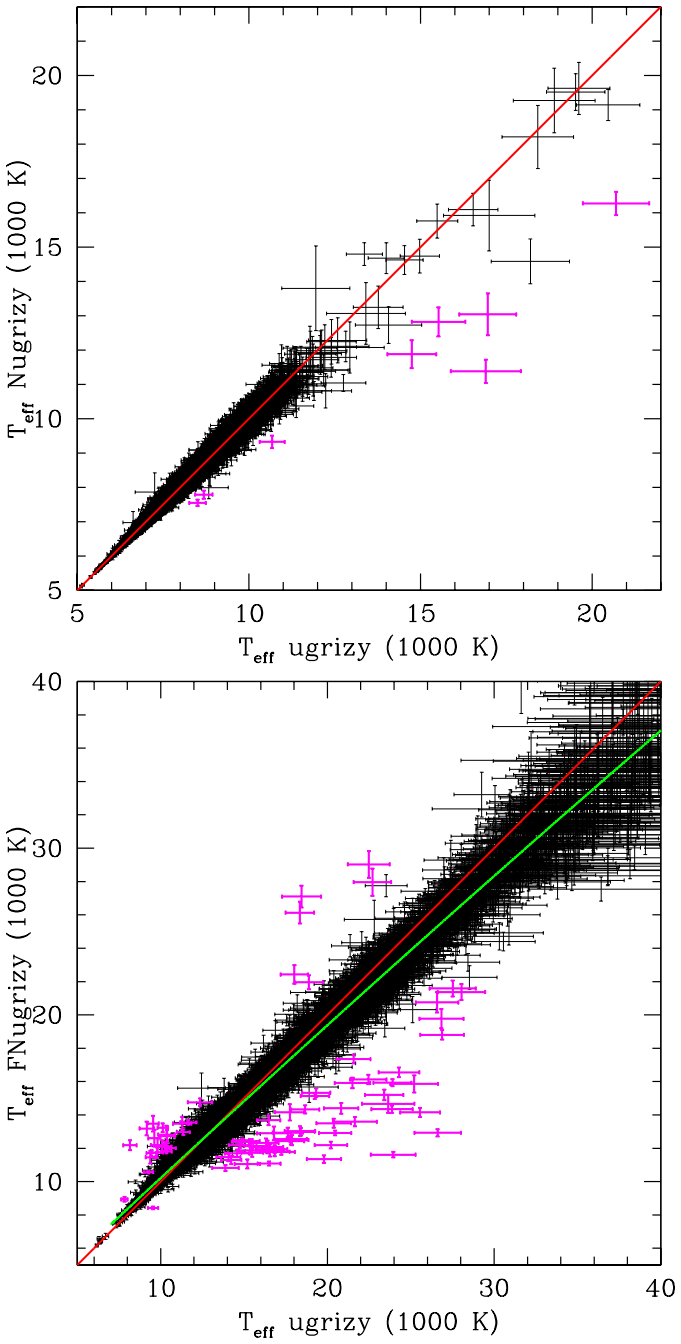

Figure 3.4.4: A comparison between the effective temperature derived from optical only data (SDSS u and Pan-STARRS $grizy$) versus the optical + UV data for the DA white dwarfs in the SDSS footprint. The top panel shows objects with only NUV data, whereas the bottom panel includes objects with both FUV and NUV data. The 1:1 line is shown in red. The green line is the best-fitting polynomial to the data. The 3σ outliers are shown in magenta.

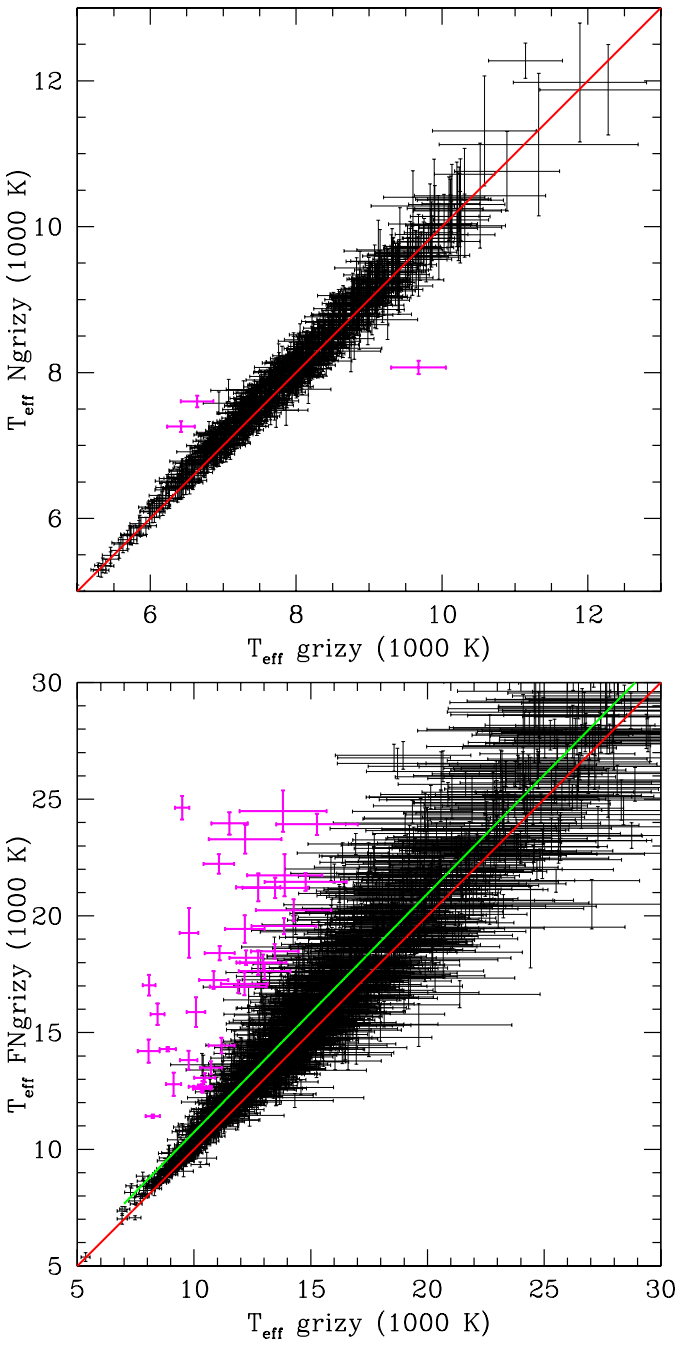

Figure 3.4.5: Same as Figure 3.4.4, but for the DA white dwarfs outside of the SDSS footprint.

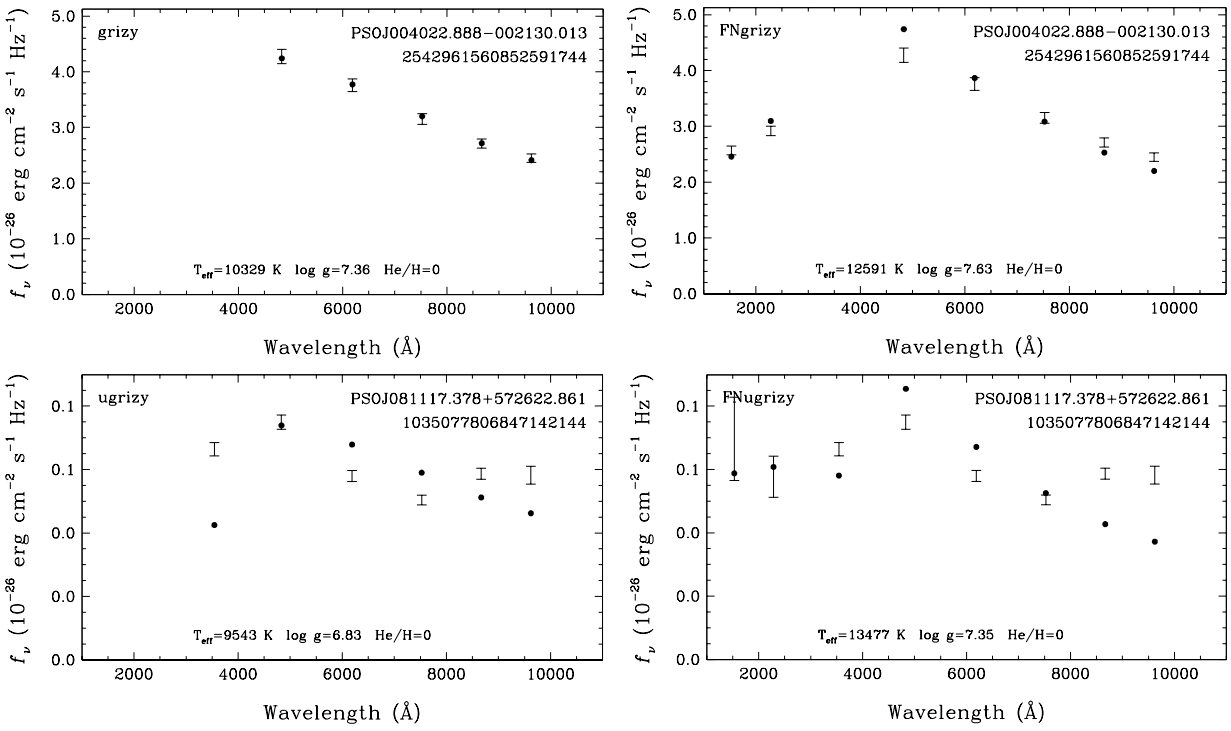

Figure 3.4.6: Fits to the optical (left) and optical + UV (right) spectral energy distributions of two of the outliers in our DA white dwarf sample. The top panels show the fits for the double-lined spectroscopic binary WD 0037−006, and the bottom panels show the fits for a previously known DA + M dwarf binary.

the sample shown here extends beyond 100 pc, and therefore is corrected for reddening using the de-reddening procedure from Harris et al. (2006) and the GALEX extinction coefficients from Wall et al. (2019). The top panel includes objects with only NUV data, whereas the bottom panel includes objects with both FUV and NUV data. The red line shows the 1:1 line, and the green line is the best-fitting polynomial to the data. The magenta points mark the outliers that are 3σ away from both lines. The best-fitting polynomial takes the form

$$y = c_2 x^2 + c_1 x + c_0, \tag{3.1}$$

where y is the $T_{\rm eff} FNugrizy/1000$ and x is $T_{\rm eff} ugrizy/1000$. The coefficients are given in table 3.4.1. The sample with the NUV data only (top panel) is limited mostly to white dwarfs with temperatures between 5000 and 12000 K. This is simply an observational bias; hotter white dwarfs would be brighter in the FUV, and therefore they would have been detected in both NUV and FUV bands.

A comparison between the model parameters obtained from $ugrizy$ and $Nugrizy$ (top panel) shows that there are no systematic differences between the two sets of fits. We find eight 3σ outliers based on this analysis, all very similar to the outliers shown in Figure 3.4.2 with UV flux deficits.

On the other hand, we do find a systematic trend in the temperature measurements from the fits using the GALEX FUV, NUV, SDSS u, and Pan-STARRS $grizy$ filters shown in the bottom panel. Here the best-fitting polynomial shows that the temperatures based on the optical + UV data are slightly underestimated compared to the temperatures obtained from the optical data only. The difference is -180 K at 15000 K, -620 K at 20000 K, and -1670 K at 30000 K. Note that the average temperature errors based on the optical data are 670, 970, and 1850 K at 15000, 20000, and 30000 K, respectively. Hence, the observed systematic shift in this figure is consistent with the optical constraints on the same systems within 1σ. We identify 83 outliers 3σ away from both the 1:1 line and the best-fitting polynomial (red and green lines in the figure) including a number of UV-excess objects.

Figure 3.4.5 shows a similar comparison for the DA white dwarfs outside of the SDSS footprint. These do not have SDSS u-band measurements, hence our model fits are based on the Pan-STARRS $grizy$ and GALEX FUV and NUV bands. The top panel shows the model fits for the DA sample with only NUV data available. Here the 1:1 line provides an excellent match to the parameters obtained from both the optical and the optical + UV analysis. We identify only 3 outliers based on this subsample.

The bottom panel in Figure 3.4.5 reveals a systematic trend in the temperature measurements based on the GALEX FUV + NUV + $grizy$ data compared to the temperatures derived from the optical only data. The best-fitting polynomial takes the form of equation 3.1 where y is the

Table 3.4.1. Coefficients for the best-fitting polynomials in figures 3.4.4 and 3.4.5.

Coefficient	Figure 3.4.4	Figure 3.4.5
c_0	0.82743420	0.48395959
c_1	0.94949536	1.02740975
c_2	-0.00109481	-0.00021316

$T_{\rm eff}FNgrizy/1000$ and x is $T_{\rm eff}grizy/1000$. The coefficients are given in table 3.4.1. This trend is similar to the one seen for the SDSS sample (bottom panel in Figure 3.4.4) but it is in the opposite direction. The optical + UV analysis leads to temperatures that are slightly over-estimated compared to the analysis using the optical data only. The difference is +850, +950, and +1090 K at 15000, 20000, and 30000 K, respectively. The average temperature errors based on the optical data are 670, 2810, and 6040 K at 15000, 20000, and 30000 K, respectively. Again, the observed systematic trend is consistent with the results from the optical only analysis within 1σ. We identify 41 outliers, all of which are UV-excess objects, based on this diagram.

In total we identify 135 outliers based on this analysis. Because the full width at half-maximum of the GALEX point spread function is about 5 arcsec (Morrissey et al., 2007), blending and contamination from background sources is an issue. We checked the Pan-STARRS stacked images for each of these outliers to identify nearby sources that could impact GALEX, SDSS, or Pan-STARRS photometry measurements. We found that 24 of these outliers were likely impacted by blending sources, reducing the final sample size to 111 outliers.

Table 3.4.2 presents the list of 52 outliers that were previously known to be unusual. This list includes four objects that are confirmed or suspected to be double white dwarfs (PSO J010.0954-00.3584, J055.6249+00.4048, J063.1211−11.5012, and J173.7025+46.8094), 20 confirmed or suspected magnetic white dwarfs, seven DA + M dwarf systems, and 21 objects with an unusual atmospheric composition (DAB etc).

Table 3.4.2. The list of outliers that were previously known to be unusual. The horizontal line separates the UV-deficit (top) and the UV-excess (bottom) objects.

Object	*Gaia* DR3 Source ID	Spectral Type	Reference
PSO J012.0395−01.4109	2530629365419780864	DA(He)	Kilic et al. (2020)
PSO J017.4701+18.0000	2785085218267094784	DA(He)	Kepler et al. (2015)
PSO J025.4732+07.7206	2571609886069150592	DAB	Kepler et al. (2015)
PSO J027.3938+24.0130	291186211300158592	DZA	Gentile Fusillo et al. (2017)
PSO J033.0221+06.7391	2521035817229538688	DA:H:	Kleinman et al. (2013)
PSO J038.5646−04.1025	2489275328645218560	DABZ	Gentile Fusillo et al. (2021)
PSO J055.6249+00.4048	3263696071424152704	DA+DB	Limoges & Bergeron (2010)
PSO J119.5813+35.7453	906772187229375104	DAH	Kleinman et al. (2013)
PSO J123.8841+21.9779	676473944873877248	DAB	Kleinman et al. (2013)
PSO J125.6983+12.0296	649304840753259520	DAH:	Kepler et al. (2015)
PSO J130.5623−02.3741	3072348715677121280	DAH?DBH?	Kilic et al. (2020)
PSO J131.8174+48.7057	1015028491488955776	DBH:	Kleinman et al. (2013)
PSO J132.3710+28.9556	705246450482748288	DAH	Kleinman et al. (2013)
PSO J132.6463+32.1345	706974637946866304	DABZ	Kong et al. (2019)
PSO J133.2881+58.7267	1037873899276147840	DABZ	Gentile Fusillo et al. (2019)
PSO J136.6362+08.1209	584319855260594560	DAH	Kleinman et al. (2013)
PSO J140.1791+04.8533	579476334742123904	DA:B:Z:	Kleinman et al. (2013)
PSO J140.7411+13.2557	594146225037566976	DABZ	Kepler et al. (2015)
PSO J143.7587+44.4946	815134799361707392	DAH:	Kepler et al. (2015)
PSO J144.9871+37.1739	799763528023185280	DAB	Kepler et al. (2015)
PSO J150.9846+05.6405	3873396705206744064	DAH	Kleinman et al. (2013)
PSO J154.6449+30.5584	742562844335742208	DAH	Kleinman et al. (2013)
PSO J179.9671+00.1309	3891115064506627840	DA(He)	Kilic et al. (2020)
PSO J182.5106+18.0931	3949977724441143552	DAB	Kepler et al. (2015)
PSO J196.1335+59.4594	1579147088331814144	DAB	Wesemael et al. (1993)
PSO J198.6769+06.5415	3729586288010410496	DA(He)	Kepler et al. (2015)
PSO J201.2108+29.5887	1462096958792720384	DA(He)	Kepler et al. (2016)
PSO J206.1217+21.0809	1249447115013660416	DABZ	Kleinman et al. (2013)
PSO J211.9610+30.1917	1453322271887656448	DA:H:	Kleinman et al. (2013)
PSO J218.8923+04.5738	3668901977825959040	DAX	Kepler et al. (2015)
PSO J223.2567+06.8724	1160931721694284416	DA:H:	Kleinman et al. (2013)

Table 3.4.2 (cont'd)

Object	*Gaia* DR3 Source ID	Spectral Type	Reference
PSO J223.9933+18.2145	1188753901361576064	DA:H:	Kleinman et al. (2013)
PSO J234.3569+51.8575	1595298501827000960	DBA	Kleinman et al. (2013)
PSO J240.2518+04.7101	4425676551115360512	DAH	Kleinman et al. (2013)
PSO J261.1339+32.5709	1333808965722096000	DAH	Kepler et al. (2015)
PSO J341.2484+33.1715	1890785517284104960	DAH/DQ	Kepler et al. (2016)
PSO J356.5226+38.8938	1919346461391649152	DAH	Kleinman et al. (2013)
PSO J010.0954−00.3584	2542961560852591744	DA+DA	Napiwotzki et al. (2020)
PSO J042.5074−04.6175	5184589747536175104	DAH:	Kepler et al. (2016)
PSO J051.5805+13.5189	17709047809907584	DAH	Kilic et al. (2020)
PSO J063.1211−11.5012	3189613692364776576	DA+DA	Napiwotzki et al. (2020)
PSO J065.0980+47.5929	257933852944165120	DAB	Verbeek et al. (2012)
PSO J094.8914+55.6121	997854527884948992	DAO	Gianninas et al. (2011)
PSO J109.2922+74.0109	1112171030998592256	DAM	Marsh & Duck (1996)
PSO J122.8223+57.4396	1035077806847142144	DAM	Rebassa-Mansergas et al. (2016)
PSO J123.9537+47.6772	931238043230275968	DAM	Farihi et al. (2010)
PSO J140.2868+13.0199	594229753561550208	DAH	Kleinman et al. (2013)
PSO J173.7025+46.8094	785521450828261632	DD?	Bédard et al. (2017)
PSO J182.0967+06.1655	3895444662122848512	DAM	Rebassa-Mansergas et al. (2016)
PSO J224.1602+10.6747	1180256944222072704	DAM	Rebassa-Mansergas et al. (2016)
PSO J337.4922+30.4024	1900545847646195840	DAM?	Rebassa-Mansergas et al. (2019)
PSO J344.9451+16.4879	2828888597582293760	DAM	Farihi et al. (2010)

Figure 3.4.6 shows the spectral energy distributions for two of these outliers. The top panels show the fits to the optical and UV + optical spectral energy distributions of the previously known double-lined spectroscopy binary WD 0037−006 (Napiwotzki et al., 2020). Under the assumption of a single star, the Pan-STARRS photometry for WD 0037−006 indicates $T_{\rm eff} = 10330 \pm 380$ K and $\log g = 7.36 \pm 0.05$. Adding the GALEX FUV and NUV data, the best-fitting solution significantly changes to $T_{\rm eff} = 12590 \pm 100$ K and $\log g = 7.63 \pm 0.01$. In addition, this solution has problems matching the entire spectral energy distribution, indicating that there is likely a cooler companion contributing significant flux. This figure demonstrates that double-lined spectroscopic binaries with significant temperature differences between the primary and the secondary star could be identified based on an analysis similar to the one presented here. A similar and complementary method for identifying double-lined spectroscopic binaries was pioneered by Bédard et al. (2017), which use optical photometry and spectroscopy to identify systems with inconsistent photometric and spectroscopic solutions.

The bottom panels in Figure 3.4.6 show the fits to a previously confirmed DA + M dwarf system in our sample (Rebassa-Mansergas et al., 2016). Here the optical data is clearly at odds with a single

DA white dwarf, and GALEX FUV and NUV data reveal UV-excess from a hotter white dwarf. The analysis using $FNugrizy$ photometry confirms excess emission in the Pan-STARRS zy-bands, consistent with an M dwarf companion.

Table 3.4.3 presents the list of 59 newly identified outliers among the DA white dwarfs with GALEX data; 24 of them show flux deficits in the UV (their optical + UV temperatures are lower than the temperatures based on the optical data only), and 35 are UV-excess objects. We include the spectral types from the literature for each source.

Even though the 24 UV-deficit objects (shown in the top half of the table) are classified as DA in the literature, our analysis indicates that they are unusual. For example, re-inspecting the SDSS spectra for three of the sources classified as DAZ in the literature, we find that the Ca H and K lines are actually stronger than the Balmer lines, indicating that they are in fact DZA white dwarfs.

Similarly, re-inspecting the SDSS and LAMOST spectra for four of these sources (PSO J018.6848+35.4095, J151.1401+40.2417, J196.7725+49.1045, and J338.5445+25.1894), we find that their Balmer lines are much weaker than expected for these relatively warm white dwarfs with $T_{\rm eff} > 10,000$ K. Figure 3.4.7 shows the model fits to three of these objects based on the optical photometry. All three stars are significantly fainter than expected in the FUV and NUV bands compared to the pure H atmosphere models. The UV photometry and the weak Balmer lines indicate that these stars are likely DA(He) white dwarfs with helium dominated atmospheres.

The newly identified UV-excess sample likely includes many binaries, including white dwarf + main-sequence and double white dwarf systems. We classify 14 of these systems as likely DA + M dwarfs based on their spectral energy distributions, which are dominated by the white dwarf in the UV and by a redder source in the Pan-STARRS zy bands. Four of these DA + M dwarf systems are also resolved in the Pan-STARRS zy band stacked images, but the resolved companions are not included in the Pan-STARRS photometric catalog. However, one of these resolved systems is confirmed to be a physical binary through *Gaia* astrometry. Both components of PSO J211.4189+74.6498 are detected in *Gaia* with source IDs *Gaia* DR3 1712016196599965312 and 1712016196599171840.

Figure 3.4.8 shows the fits to the optical and optical + UV spectral energy distributions for three of the newly identified UV-excess sources that may be double white dwarfs. There are small but significant temperature discrepancies between the photometric solutions relying on optical and optical + UV data and also the optical spectroscopy. For example, for PSO J218.2047+01.7710 the model fits to the optical photometry give $T_{\rm eff} = 10341 \pm 329$ K and $\log g = 7.51 \pm 0.05$, while the fits to the optical + UV photometry give $T_{\rm eff} = 11793 \pm 98$ K and $\log g = 7.74 \pm 0.02$. Fitting the normalized Balmer line profiles, Tremblay et al. (2011) obtained $T_{\rm eff} = 11360 \pm 120$ K and $\log g = 8.19 \pm 0.06$ for the same star. The inconsistent $\log g$ estimates can be explained if the

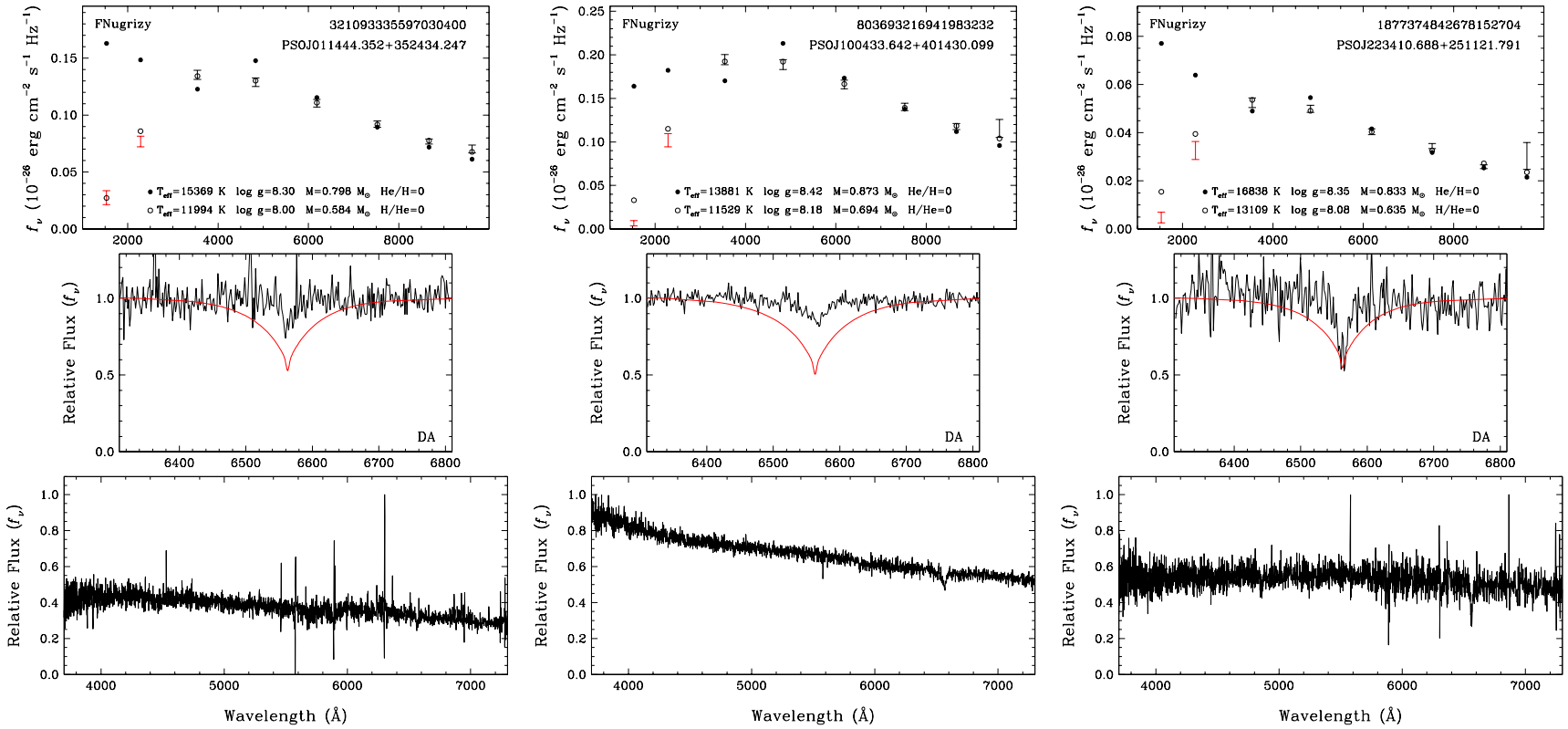

Figure 3.4.7: Model atmosphere fits to three DA white dwarfs with UV flux deficits. The top panels show the best-fitting H (filled dots) and He (open circles) atmosphere white dwarf models to the optical photometry (black error bars). The middle panels show the observed spectrum (black line) along with the predicted spectrum (red line) based on the pure H atmosphere solution. The bottom panels show a broader wavelength range. GALEX FUV and NUV data clearly favor the He-dominated atmosphere solutions, which are also confirmed by the relatively weak Balmer lines in their spectra.

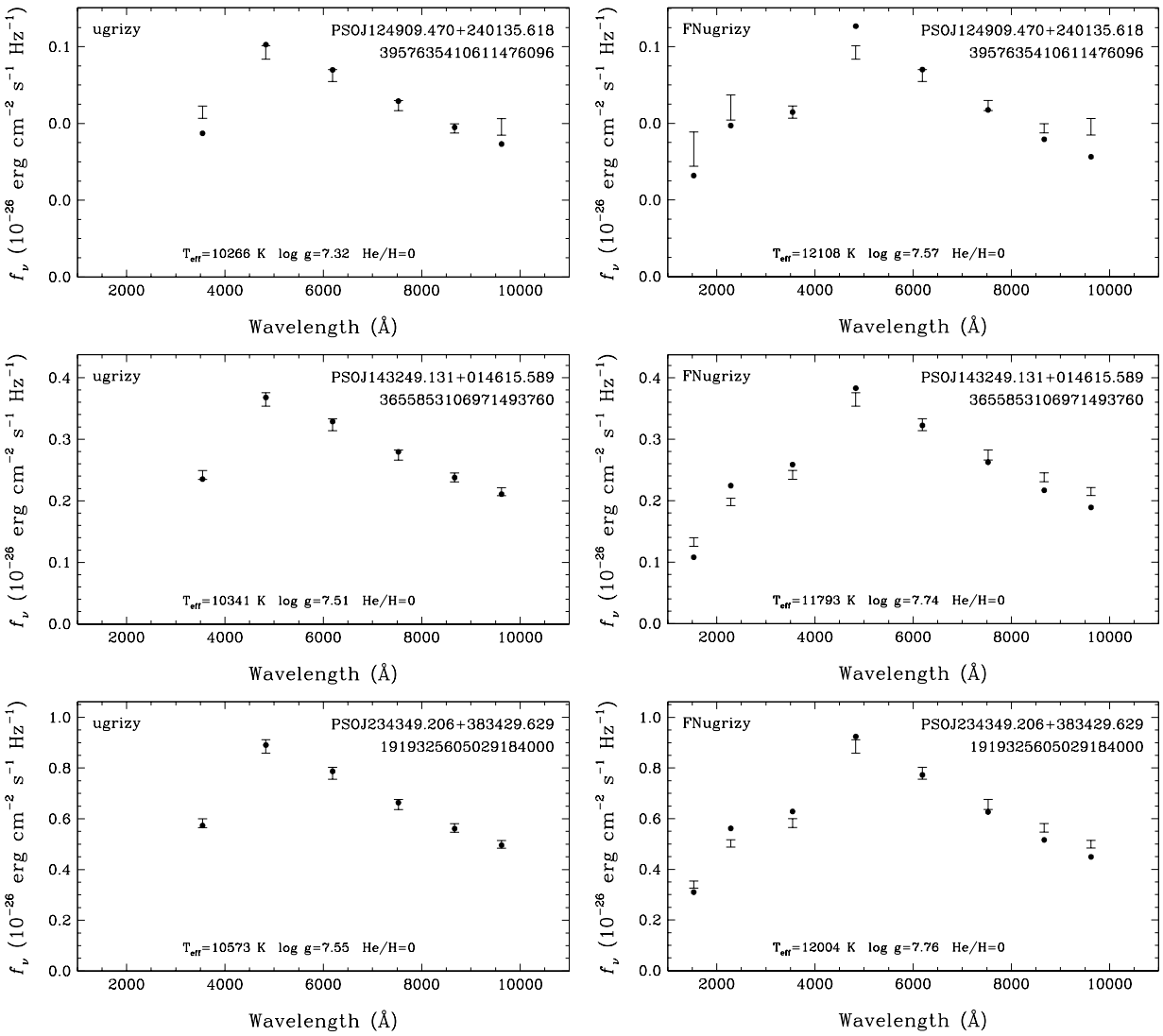

Figure 3.4.8: Fits to the optical (left) and optical + UV (right) spectral energy distributions of three of the newly identified UV-excess sources in our DA white dwarf sample. The inconsistent temperature estimates from the optical and UV photometry and optical spectroscopy indicate that they may be double white dwarfs.

Table 3.4.3. Newly identified outliers among the DA white dwarf population with GALEX data.
The horizontal line separates the UV-deficit (top) and the UV-excess (bottom) objects.

Object	*Gaia* DR3 Source ID	Optical $T_{\rm eff}$ (K)	Optical + UV $T_{\rm eff}$ (K)	Spectral Type	Reference	Notes
PSO J018.6848+35.4095	321093335597030400	15369 ± 678	11872 ± 223	DA	Gentile Fusillo et al. (2015)	DA(He) LAMOST
PSO J032.2011+12.2256	73623921366683008	27516 ± 1379	21586 ± 476	DA	Kleinman et al. (2013)	
PSO J043.8655+02.6202	1559111783825792	8685 ± 254	7788 ± 117	DA	Kilic et al. (2020)	
PSO J056.0479+15.1626	42871199614383616	8503 ± 241	7548 ± 90	DA	Andrews et al. (2015)	
PSO J103.8966+29.6527	887758130788405504	19249 ± 849	15130 ± 168	DA	Kilic et al. (2020)	massive
PSO J130.7484+10.6677	598412403168328960	15748 ± 731	12139 ± 293	DAZ	Kepler et al. (2015)	DZA SDSS
PSO J132.2963+14.4454	608922974120358784	19793 ± 1038	11354 ± 226	DA	Gentile Fusillo et al. (2019)	
PSO J139.0499+34.9872	714469355877947136	23646 ± 1571	14667 ± 545	DA	Kleinman et al. (2013)	massive
PSO J151.1401+40.2417	803693216941983232	13881 ± 797	10816 ± 188	DA	Kepler et al. (2015)	DA(He) SDSS
PSO J158.8293+27.2510	728222390915647872	17876 ± 998	12484 ± 307	DA	Gentile Fusillo et al. (2019)	
PSO J159.5929+37.3533	751930335511863040	14891 ± 628	12383 ± 194	DA:DC:	Kleinman et al. (2013)	DAB SDSS
PSO J163.5943−02.7860	3801901270848297600	25209 ± 1429	15858 ± 522	DA	Croom et al. (2001)	massive
PSO J172.6518−00.3655	3797201653208863360	15198 ± 761	11058 ± 264	DA:Z	Kleinman et al. (2013)	DZA SDSS
PSO J180.6015+40.5822	4034928775942285184	16551 ± 835	11880 ± 377	DA	Kleinman et al. (2013)	DC: SDSS
PSO J196.7725+49.1045	1554826818838504576	14573 ± 736	11689 ± 225	DA:	Kleinman et al. (2013)	DA(He) SDSS
PSO J213.8277+31.9308	1477633195532154752	16960 ± 829	13040 ± 608	DAZ	Gentile Fusillo et al. (2019)	DZA SDSS
PSO J215.2971+38.9912	1484931581918492544	17743 ± 873	14159 ± 483	DA:	Kleinman et al. (2013)	DC: SDSS
PSO J231.8495+06.7581	1162614902197098624	16792 ± 1013	12897 ± 411	DA	Carter et al. (2013)	massive
PSO J249.3471+53.9644	1426634650780861184	16315 ± 761	12321 ± 257	DAZ	Kepler et al. (2016)	
PSO J309.1036+77.8178	2290767158609770240	28040 ± 1427	21372 ± 486	DA	Bédard et al. (2020)	

Table 3.4.3 (cont'd)

Object	*Gaia* DR3 Source ID	Optical $T_{\rm eff}$ (K)	Optical + UV $T_{\rm eff}$ (K)	Spectral Type	Reference	Notes
PSO J324.1725+01.0846	2688259922223271296	16404 ± 937	12078 ± 389	DA	Vidrih et al. (2007)	
PSO J338.5445+25.1894	1877374842678152704	16838 ± 892	11787 ± 266	DA	Gentile Fusillo et al. (2019)	DA(He) SDSS
PSO J342.5363+22.7580	2836800855054851456	26580 ± 1279	20752 ± 605	DA	Bédard et al. (2020)	
PSO J348.7601+22.1674	2838958711048617856	26837 ± 1327	19773 ± 571	DA	Kleinman et al. (2013)	
PSO J003.9449−30.1015	2320237751020937728	9768 ± 375	13816 ± 408	DA	Vennes et al. (2002)	
PSO J009.0492−17.5443	2364297204875140224	13479 ± 1408	21203 ± 437	DA	Gianninas et al. (2011)	
PSO J015.0435−28.1077	5033974938207807488	13023 ± 1105	17630 ± 337	DA	Croom et al. (2004)	
PSO J019.3103+24.6726	294062563782633216	12160 ± 1007	17090 ± 490	DA	Kleinman et al. (2013)	
PSO J021.9568+73.4798	535482641132742400	6422 ± 190	7259 ± 75	DA	Limoges et al. (2015)	
PSO J023.0575−28.1766	5035296654263954304	12745 ± 931	17999 ± 527	DA	Croom et al. (2004)	
PSO J029.9572−27.8589	5024390701506507648	11176 ± 562	14449 ± 337	DA	Croom et al. (2004)	
PSO J041.4724−12.7058	5158731712247303040	9493 ± 307	24634 ± 504	DA	Kilkenny et al. (2016)	DAM?
PSO J051.6792+69.4045	494644717692834944	13855 ± 1393	19565 ± 343	DA	Gianninas et al. (2011)	
PSO J052.0294+52.9603	443375555640546944	10729 ± 467	13492 ± 282	DA	Verbeek et al. (2012)	
PSO J052.2834+52.7335	443274778529615232	10363 ± 382	12680 ± 249	DA	Verbeek et al. (2012)	
PSO J102.2271+38.4434	944388335442133888	13883 ± 1606	21741 ± 901	DA	Kleinman et al. (2013)	
PSO J125.7399+57.8364	1034975243028553600	18178 ± 2420	31076 ± 1012	DA	Bédard et al. (2020)	
PSO J143.4929+17.7146	632864633657062400	13811 ± 1864	24486 ± 883	DA	Bédard et al. (2020)	DAM?
PSO J143.5436+22.4702	644043544469790720	14268 ± 1613	20245 ± 465	DA	Kleinman et al. (2013)	DAM?
PSO J146.2852+62.7948	1063508669280315776	9623 ± 370	12604 ± 502	DA	Kleinman et al. (2013)	DAM?

Table 3.4.3 (cont'd)

Object	*Gaia* DR3 Source ID	Optical $T_{\rm eff}$ (K)	Optical + UV $T_{\rm eff}$ (K)	Spectral Type	Reference	Notes
PSO J149.4751+85.4946	1147853241336105344	28499 ± 4417	50953 ± 4975	DA	Gianninas et al. (2011)	
PSO J150.3866+01.5162	3835962526168788608	22704 ± 1127	27966 ± 821	DA	Kepler et al. (2015)	
PSO J167.1417+31.8979	757803896562843392	14778 ± 1760	21458 ± 382	DA	Gianninas et al. (2011)	
PSO J192.2894+24.0266	3957635410611476096	10266 ± 381	12108 ± 291	DA	Kleinman et al. (2013)	
PSO J200.6206+01.0147	3688065808367722368	9383 ± 291	11459 ± 371	DA	Croom et al. (2004)	DAM?
PSO J211.4189+74.6498	1712016196599965312	8237 ± 305	11420 ± 77	DA	Mickaelian (2008)	resolved DAM
PSO J218.2047+01.7710	3655853106971493760	10341 ± 329	11793 ± 97	DA	Kleinman et al. (2013)	
PSO J221.4238+41.2449	1489712503290614912	9786 ± 396	19274 ± 1067	DA	Bédard et al. (2020)	DAM?
PSO J223.4269+46.9171	1590342178286505216	12174 ± 851	19440 ± 593	DA	Kleinman et al. (2013)	
PSO J240.6992+43.8100	1384551977098980608	10070 ± 352	12113 ± 369	DA	Kleinman et al. (2013)	resolved DAM?
PSO J240.8660+19.6618	1203265358904378880	10085 ± 401	15880 ± 632	DA	Kleinman et al. (2013)	DAM?
PSO J244.6129+20.5911	1202035422006406400	9808 ± 394	12191 ± 410	DA	Kleinman et al. (2013)	resolved DAM?
PSO J259.6449+01.9471	4387171623850187648	10215 ± 438	12685 ± 84	DA	McCleery et al. (2020)	
PSO J263.1394+32.8366	4601788317833882240	9790 ± 353	11747 ± 336	DA	Kepler et al. (2015)	DAM?
PSO J276.0344+35.2718	2095603539740855296	11063 ± 653	22229 ± 415	DA	Mickaelian (2008)	DAM?
PSO J334.7157−29.4534	6615258025441899776	10838 ± 624	17254 ± 376	DA	Croom et al. (2004)	DAM?
PSO J346.5586−28.0099	6606686198432918656	11516 ± 779	23961 ± 485	DA	Croom et al. (2004)	resolved DAM?
PSO J352.1333−30.0610	2329285662270302976	12190 ± 1555	23284 ± 616	DA	Vennes et al. (2002)	
PSO J355.9551+38.5749	1919325605029184000	10573 ± 344	12004 ± 78	DA	Kleinman et al. (2013)	

photometry is contaminated by a companion (see also Bédard et al., 2017), and the small temperature differences between the different solutions favor a white dwarf companion rather than a cool, late-type M dwarf star. Follow-up spectroscopy of these three systems, as well as the rest of the UV-excess sample would be helpful for constraining the nature of these objects and identifying additional double white dwarf binaries.

3.5. Results from UV Magnitude Comparison

The optical/UV temperature comparison method presented in the previous section provides an excellent method to identify sources with grossly different temperatures. However, it may miss some sources with unusual UV fluxes. Those model fits rely on three (gri) to six ($ugrizy$) optical filters versus one or two GALEX UV filters, hence the UV data have a lesser weight in constraining the temperatures.

To search for additional outliers that were potentially missed by the temperature comparison method, here we use model fits to the optical photometry plus *Gaia* parallaxes to predict the brightness of each star in the GALEX filters, and search for significant outliers using FUV and NUV data. To obtain the best constraints on the predicted FUV and NUV brightnesses of each source, we further require our stars to have photometry in the SDSS u filter as well as all of the Pan-STARRS filters. Our final magnitude comparison sample contains 10049 DA white dwarfs with photometry in at least one of the GALEX filters, the SDSS u, and the Pan-STARRS $grizy$ filters.

Figure 3.5.1 shows a comparison of the observed and predicted FUV (top) and NUV (bottom panel) magnitudes of the 10049 DA white dwarfs in our magnitude comparison sample. The blue dashed line is the 1:1 correlation between observed and model magnitudes. The green diamonds are previously known DAB white dwarfs while the green triangles are DA white dwarfs that have significant amounts of helium in their atmospheres, making the use of pure hydrogen atmosphere models inappropriate. The yellow diamonds are previously known magnetic white dwarfs and the black triangles are previously known DA + M dwarf systems. The blue diamonds are white dwarfs with uncertain (e.g., DA:) classifications.

As with the temperature comparison sample, blending and contamination from background sources is an issue for some sources. We checked the Pan-STARRS stacked images for each of these outliers to identify nearby sources that could impact GALEX, SDSS, or Pan-STARRS photometry measurements. The outliers that were affected by contamination are marked by blue triangles in Figure 3.5.1. The red squares are 30 newly identified 3σ outliers. Table 3.5.1 presents this list along with their photometric and spectroscopic temperatures based on the optical data.

Figure 3.5.2 displays the spectral energy distributions for four of these outliers. Outliers with UV-excesses, such as PSO J226.4550+11.0849 shown in the top right panel of Figure 3.5.2, are likely binaries. Outliers with UV-deficits, such as PSO J253.3655+27.5061 shown in the bottom

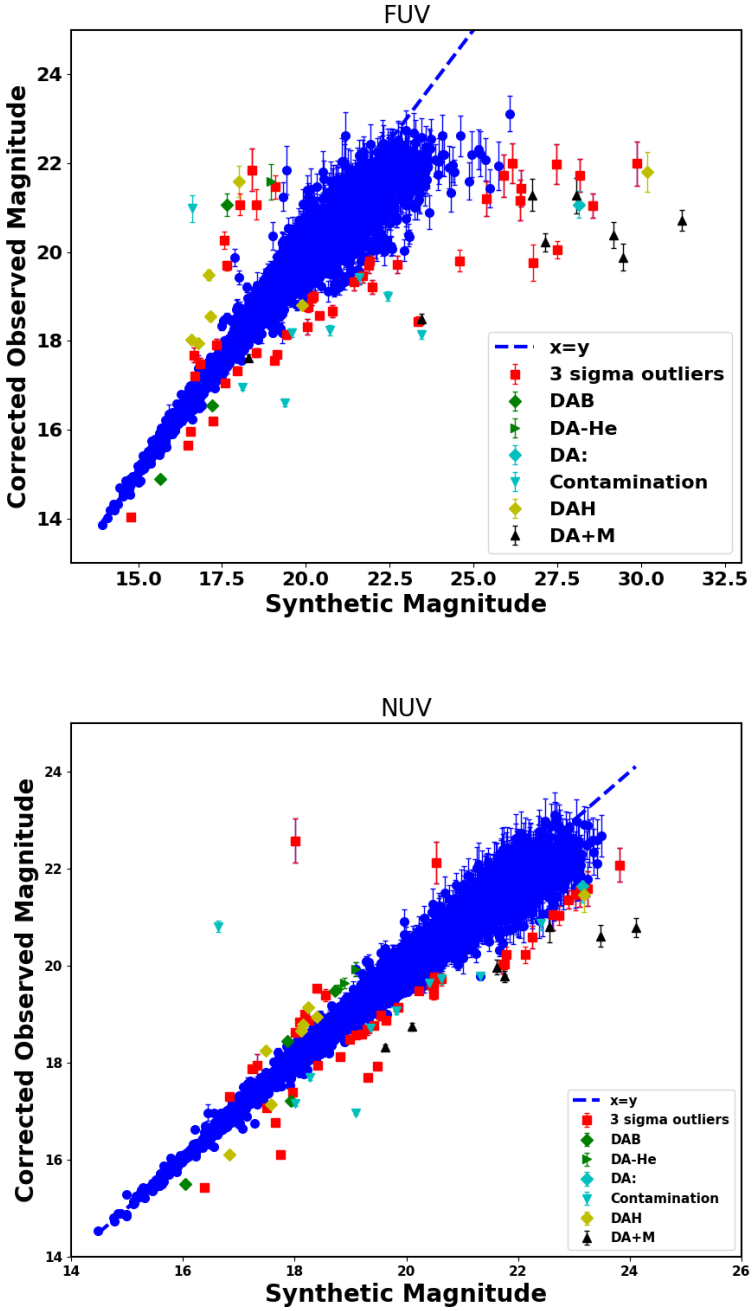

Figure 3.5.1: Comparison between observed and model FUV (top) and NUV (bottom) magnitudes. The blue dashed line is the 1:1 correlation. The green diamonds are previously known DAB white dwarfs, the green triangles are previously known DA-He white dwarfs, the cyan diamonds are white dwarfs with uncertain classifications, the cyan triangles are objects with contaminated photometry, and the yellow diamonds are previously known magnetic white dwarfs. Previously unknown 3σ outliers are plotted as red squares.

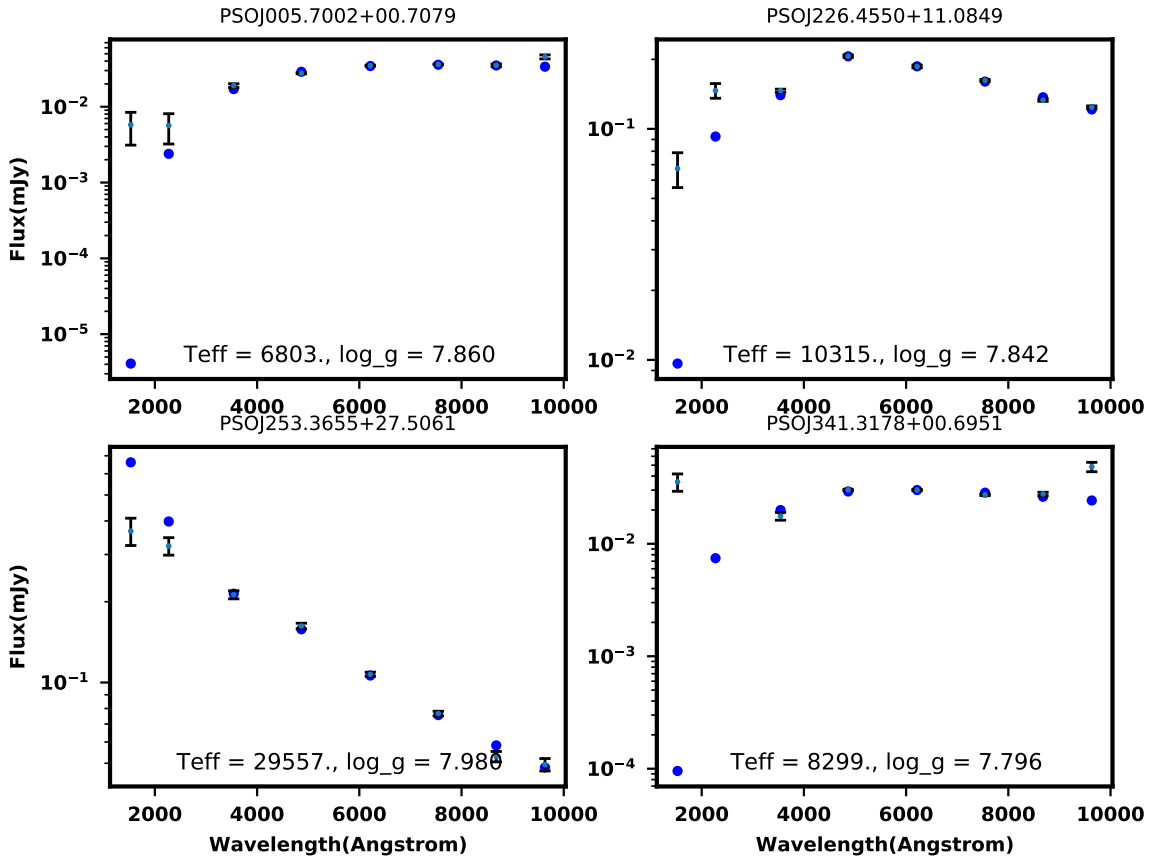

Figure 3.5.2: Spectral energy distributions of four newly identified outliers in the magnitude comparison sample. The filled dots are the model fluxes and the error bars are the observed photometry.

Table 3.5.1. Additional outliers identified through a comparison of the observed and predicted UV magnitudes.

Object	*Gaia* DR3 Source ID	Photometric $T_{\rm eff}$ (K)	Spectroscopic $T_{\rm eff}$ (K)	Spectral Type	Reference	Notes
PSO J001.0830+23.8334	2849729771768028544	27453	34738	DA	Kepler et al. (2016)	
PSO J004.9372+33.6842	2864011530163554816	7513	8982	DA	Kepler et al. (2016)	
PSO J005.7002+00.7079	2546893650655427840	6803	6992	DA	Kleinman et al. (2013)	DAM?
PSO J021.8549+27.6214	296372465914661248	6823	6723	DA	Kepler et al. (2016)	
PSO J056.0308-05.2121	3244802712151826048	10331	12371	DA	Kleinman et al. (2013)	DAM?
PSO J118.9063+21.1283	673549759340742272	9270	9941	DA	Kleinman et al. (2013)	DAM?
PSO J126.3419+17.4310	662102679359467648	7867	7838	DA	Kleinman et al. (2013)	
PSO J137.9380+35.5266	714377928911156992	14027	19527	DA	Kleinman et al. (2013)	
PSO J149.4951+57.6078	1046386971133757184	10292	11288	DA	Kleinman et al. (2013)	DAM?
PSO J152.4806+00.1622	3831830527112439936	10569	10513	DA	Kleinman et al. (2013)	
PSO J176.3500+24.1592	4004972723377902592	7188	7403	DA	Kepler et al. (2016)	
PSO J189.9978+33.1080	1514768341766532992	10348	10957	DA	Kleinman et al. (2013)	DAM?
PSO J204.9827+60.1751	1662524184641472640	7888	9463	DA	Kleinman et al. (2013)	
PSO J205.8897+23.2339	1443624343108905216	9516	10373	DA	Kleinman et al. (2013)	
PSO J210.9347+37.1660	1483513830393895680	8703	11040	DA	Kepler et al. (2015)	DAM?
PSO J213.9910+62.5129	1666750569898974208	9593	10114	DA	Kleinman et al. (2013)	
PSO J226.4550+11.0849	1180520345976350208	10315	11354	DA	Kleinman et al. (2013)	
PSO J226.6089+06.6459	1160300056558791168	9500	10670	DA	Farihi et al. (2012)	

Table 3.5.1 (cont'd)

Object	*Gaia* DR3 Source ID	Photometric $T_{\rm eff}$ (K)	Spectroscopic $T_{\rm eff}$ (K)	Spectral Type	Reference	Notes
PSO J227.2923+37.1129	1292306146987734784	8264	8526	DA	Kepler et al. (2015)	
PSO J244.4451+40.3379	1380686815769537920	7600	13013	DA	Kepler et al. (2015)	DAM?
PSO J248.9274+26.3827	1304383217063475968	30346	34544	DA	Kleinman et al. (2013)	
PSO J249.2986+12.8853	4459617994029737216	7824	7904	DA	Kepler et al. (2015)	DAM?
PSO J250.5693+22.9411	1299405148103896832	11188	12763	DA	Kleinman et al. (2013)	
PSO J251.3785+41.0348	1356243233471452288	7884	8068	DA	Kepler et al. (2015)	
PSO J253.3655+27.5061	1306991499163308160	29557	30472	DA	Kleinman et al. (2013)	
PSO J328.6059-00.6697	2680152673235328768	17608	20257	DA	Kleinman et al. (2013)	
PSO J331.0859+24.2120	1795394701659196032	6847	6873	DA	Kepler et al. (2015)	DAM?
PSO J341.3178+00.6951	2653703714870987648	8299	9611	DA	Kleinman et al. (2013)	DAM?
PSO J349.8567+07.6224	2664938112366990080	7394	8519	DA	Kepler et al. (2016)	
PSO J358.8416+16.8000	2773308246143281920	7149	7066	DA	Kepler et al. (2016)	

left of Figure 3.5.2, do not fit the expectations from pure hydrogen atmosphere models in the UV. Their atmospheres might be dominated by helium or might contain metals, making the use of pure hydrogen models inappropriate. Alternatively, they could also be magnetic. Further observations are needed to confirm the nature of these UV-excess and UV-deficit objects.

3.6. Conclusions

We analyzed the UV to optical spectral energy distributions of 14001 DA white dwarfs from the Montreal White Dwarf Database, taking advantage of the GALEX FUV and NUV data and *Gaia* DR3 parallaxes. Using the 100 pc sample where extinction is negligible, we demonstrated that there are no major systematic differences between the best-fit parameters derived from optical only data and the optical + UV photometry. The effective temperatures derived from optical and UV + optical data differ by only 50^{+215}_{-71} K. The addition of GALEX FUV and NUV data in the model atmosphere analysis helps improve the statistical errors in the fits, especially for hot white dwarfs.

We used two different methods to identify UV-excess or UV-deficit objects. In the first method, we compared the temperatures obtained from fitting the optical data with those obtained from fitting optical + UV data. We identified 111 significant outliers with this method, including 52 outliers that were previously known to be unusual. These include DA white dwarfs with helium dominated atmospheres, magnetic white dwarfs, double white dwarfs, and white dwarf + M dwarf systems. Out of the 59 newly identified systems, 35 are UV-excess and 24 are UV-deficit objects. In the second method, we used the optical photometry to predict the FUV and NUV magnitudes for each source, and classified sources with 3σ discrepant FUV and/or NUV photometry as outliers. Using this method, we identified 30 additional outliers.

Combining these two methods, our final sample includes 89 newly identified outliers. The nature of these outliers cannot be constrained by our analysis alone. Many of the UV-excess objects are likely binaries, including double degenerates and white dwarfs with late-type stellar companions. Follow-up spectroscopy and infrared observations of these outliers would help constrain their nature.

Acknowledgements

This work is supported by NASA under grant 80NSSC22K0479, the NSERC Canada, the Fund FRQ-NT (Québec), and by NSF under grants AST-1906379 and AST-2205736. The Apache Point Observatory 3.5-meter telescope is owned and operated by the Astrophysical Research Consortium.

This work has made use of data from the European Space Agency (ESA) mission *Gaia* (https://www.cosmos.esa.int/Gaia), processed by the *Gaia* Data Processing and Analysis Consortium (DPAC, https://www.cosmos.esa.int/web//dpac/consortium). Funding for the DPAC has been provided by national institutions, in particular the institutions participating in the *Gaia* Multilateral Agreement.

CHAPTER 4

Conclusions

4.1. Chapter Summaries

In this dissertation, I have presented our work on the study of DA white dwarfs using GALEX photometry. Here I will give a brief summary of that work.

4.1.1. Chapter 2

In chapter 2, I presented our work deriving corrections for local nonlinearity in GALEX data as well as our derivation of empirical extinction coefficients for the GALEX FUV and NUV bands. We had an initial sample of 1837 DA white dwarfs that were observed by both SDSS and GALEX. We first considered our $d < 100$ pc sample, for which extinction is not an issue, for improving the corrections for local nonlinearity originally presented in Camarota & Holberg (2014). We found that our sample lacked white dwarfs brighter than 14th magnitude, so we combined our 100 pc sample with the bright white dwarf samples form Camarota & Holberg (2014) and Gianninas et al. (2011). Using this combined sample, we determined an improved linearity correction to the GALEX data. We determined that our linearity corrections are only necessary for objects brighter than 15.95 mag and 16.95 mag for the FUV and NUV bands, respectively.

We then turned our attention to our $d > 250$ pc sample, which suffers from full extinction, for the derivation of empirical extinction coefficients. Before beginning our derivations, we used our improved linearity corrections on the bright stars in our sample. We calculated the R values for each star and then took the weighted mean. Our final extinction coefficients for the GALEX bands are $R_{\rm FUV} = 8.01 \pm 0.07$ and $R_{\rm NUV} = 6.79 \pm 0.04$. These white dwarfs currently provide the best constraints on the linearity corrections and extinction coefficients for GALEX data.

We used our improved linearity corrections and extinction coefficients to search for unusual white dwarfs within our sample. We identified seven previously known objects and five previously unknown objects. The UV-excesses of two of the previously unknown objects (WD 0846+335, SDSS J083029.77+085014.20) can be explained by contaminating background sources. The UV-excesses of SDSS J212411.99−072648.70 can be explained by an inaccurate photometric solution. The remaining two outliers, SDSS J091145.12+353135.60 and SDSS J060255.98+632304.80, require follow-up spectroscopy to verify their nature. SDSS J060255.98+632304.80 is likely to be a previously unknown ZZ Ceti as it's $T_{\rm eff}$ and $\log g$ measurements lie within the ZZ Ceti instability strip.

4.1.2. Chapter 3

In chapter 3, I presented our work on DA white dwarfs from the Montreal White Dwarf Database. Taking advantage of the GALEX FUV and NUV data and *Gaia* DR3 parallaxes, we analyzed the UV to optical spectral energy distributions of 14001 DA white dwarfs. We performed two sets of fits on our sample. In the first we used only optical data and in the second we used both the optical and UV data. Using the 100 pc sample where extinction is negligible, we demonstrated that there are no major systematic differences between the best-fit parameters derived from optical only data and the optical + UV photometry. However, the addition of GALEX FUV and NUV data in the model atmosphere analysis does help improve the statistical errors in the fits, especially for hot white dwarfs.

We used two different methods to identify UV-excess or UV-deficit objects. In the first method, we compared the temperatures obtained from fitting the optical data with those obtained from fitting optical + UV data. Using this temperature comparison method, we identified 111 significant outliers. 52 of these outliers were previously known to be unusual. These include DA white dwarfs with helium dominated atmospheres, magnetic white dwarfs, double white dwarfs, and white dwarf + M dwarf systems. Only four out of the 52 previously known outliers are confirmed or suspected double white dwarfs. The majority of the 52 previously known outliers are either magnetic white dwarfs (20 outliers) or have an unusual atmospheric composition (21 outliers). Out of the 59 newly identified systems, 35 are UV-excess and 24 are UV-deficit objects. Our analysis of the spectra of the 24 UV-deficit outliers indicates that, although they are classified as DA white dwarfs in the literature, they have unusual atmospheres. For example, PSO J018.6848+35.4095, J151.1401+40.2417, and J338.5445+25.1894, whose model fits are shown in figure 3.4.7, have Balmer lines that are much weaker than expected given their temperatures. This indicates that these white dwarfs have helium dominated atmospheres. Of the 35 newly identified UV-excess objects, 14 are likely to be DA + M dwarf systems.

In the second method, we used the optical photometry to predict the FUV and NUV magnitudes for each source and compared the predicted GALEX magnitudes to the observed GALEX magnitudes. This magnitude comparison method was used to supplement the temperature comparison method since the UV data, of which there are one or two filters, have a lesser weight in constraining the temperatures than the optical data , of which there are three to six filters. We classified sources with 3σ discrepant FUV and/or NUV photometry as outliers. Using this magnitude comparison method, we identified 30 additional outliers. 10 of these outliers are likely to be DA + M dwarf systems.

Combining the results of the two methods used to identify UV-excess and UV-deficit objects, our final sample includes 89 newly identified outliers. The nature of these outliers cannot be

constrained by our analysis alone. Many of the UV-excess objects are likely binaries, including double degenerates and white dwarfs with late-type stellar companions. Based on our analysis alone, it is likely that 24 of these objects are DA + M dwarf systems. Follow-up spectroscopy and infrared observations of these outliers would help constrain their nature.

4.2. Future Work

There is still a lot of valuable information that GALEX has to offer. In GUVcat alone there are 82,992,086 unique objects covering 24,790 square degrees of the sky. There are many data archives, such as the Montreal White Dwarf Database, containing DA white dwarfs that can be cross matched with GUVcat. The updated linearity correction along with the new empirical GALEX extinction coefficients derived in chapter 2 can be used to accurately study the UV photometry of white dwarfs beyond 100 pc, such as the 758 white dwarfs with distances between 100 pc and 250 pc from our initial sample in chapter 2. This will greatly expand the sample size of white dwarfs that can be studied in the UV.

There are several current and upcoming surveys that are specifically targeting large numbers of white dwarfs spectroscopically. For example, the Dark Energy Spectroscopic Instrument Data Release 1 is expected to contain spectra for over 47000 white dwarf candidates (Manser et al., 2023). There is also the new multi-object survey spectrograph, WEAVE, on the 4.2 m William Herschel Telescope. This spectrograph allows astronomers to take optical spectra of up to ≈1000 objects over a 2 degree field of view in a single exposure. DA white dwarfs make up the majority of the white dwarf population. Hence, the number of spectroscopically confirmed DA white dwarfs will increase significantly in the near future. In addition to these spectroscopic surveys, *Gaia*'s EDR3 contains 259,687 high probability white dwarfs ($P_{\rm WD} > 0.7$) with relatively warm temperatures ($T_{\rm eff} \geq 6500$ K) (Gentile Fusillo et al., 2021). These white dwarfs should be detected by the Ultraviolet Transient Astronomy Satellite (ULTRASAT, Ben-Ami et al., 2022).

4.2.1. ULTRASAT

ULTRASAT will perform an all-sky survey during the first 6 months of the mission to a limiting magnitude of 23 to 23.5 in its 230-290 nm NUV passband. This survey will be about an order of magnitude deeper than GALEX. Using the data from the ULTRASAT all-sky survey in combination with *Gaia* DR3 parallaxes and ground- and space-based optical and infrared photometry, we will be able to constrain the masses, temperatures, and cooling ages of a much larger sample of DA white dwarfs. In addition to characterizing the physical parameters of these white dwarfs, the temperature and magnitude comparison methods from chapter 3 can be used to identify unusual objects among the DA white dwarf population.

ULTRASAT will also perform a high-cadence survey. It will observe 2 fields for 6 months with

continuous 300 s exposures. This data can be used to perform a study of the UV variability of a large number of white dwarfs. Using *Kepler* data, Maoz, Mazeh, & McQuillan (2015) found that about half of their white dwarf sample show low-level periodic photometric modulations. These modulations have periods ranging from 1 hr to 10 days. So, ULTRASAT's high-cadence survey will reveal a large number of photometrically varying white dwarfs within the solar neighborhood. This study can reveal several different phenomena.

4.2.2. Binaries

In binary systems, photometric variability can be caused by a number of affects: relativistic beaming, ellipsoidal variations, eclipses, and reflection or re-radiation of the primary white dwarfs light by the secondary companion. These secondary companions can be stellar or sub-stellar, including planetary mass objects.

For stellar or sub-stellar companions, short period binary systems are of particular interest. If the secondary is also a white dwarf, the binary system could be the progenitor of a type Ia supernova, as well as a gravitational wave source for the upcoming *LISA* mission.

For planetary companions, the fate of planetary systems after their host star evolves has long been a question in astronomy. In recent years, several interesting planetary mass objects have been discovered around white dwarfs. Vanderburg et al. (2015) discovered a disintegrating planetesimal around WD 1145+017. Vanderburg et al. (2020) discovered a giant planet candidate around WD 1856+534. A large scale variability survey such as ULTRASAT's high-cadence survey could find other planetary companions around white dwarfs. It can also help to constrain the frequency of planetary mass objects around white dwarfs.

4.2.3. Pulsations

For single white dwarfs, the most common forms of variability are rotation and pulsations. The amplitude of pulsations is significantly higher in the UV, so ULTRASAT will be a very sensitive instrument for detecting DAV and DBV white dwarfs. The 6 month long light curves produced by ULTRASAT's high-cadence survey will provide an excellent opportunity to put constraints on white dwarf pulsation modes and physical parameters, e.g., core composition and surface H layer thickness (Fontaine & Brassard, 2008; Winget & Kepler, 2008; Córsico et al., 2019).

4.2.4. Beyond DA white dwarfs

Although DA white dwarfs make up the majority of the white dwarf population, they are not the only type of white dwarfs. There are thousands of other types of spectroscopically confirmed white dwarfs in the MWDD and the SDSS archives. For example, using a cross-match between the MWDD, *Gaia* DR3, GUVcat, and Pan-STARRS, we found 1445 spectroscopically confirmed white

dwarfs from the MWDD with GALEX FUV and NUV data, Pan-STARRS optical photometry, and 3σ significant parallax measurements from *Gaia*. Methods similar to those used in this dissertation can be used to study non-DA white dwarfs using GALEX data and, in the future, ULTRASAT data. There is a wealth of information yet to be unearthed in the GALEX archive and many future opportunities to further the study of white dwarfs in the UV.

References

Andrews J. J., Agüeros M. A., Gianninas A., Kilic M., Dhital S., Anderson S. F., 2015, ApJ, 815, 63

Badenes C., Mullally F., Thompson S. E., Lupton R. H., 2009, ApJ, 707, 971. doi:10.1088/0004-637X/707/2/971

Bailer-Jones C. A. L., Rybizki J., Fouesneau M., Demleitner M., Andrae R., 2021, AJ, 161, 147

Baxter R. B., Dobbie P. D., Parker Q. A., Casewell S. L., Lodieu N., Burleigh M. R., Lawrie K. A., et al., 2014, MNRAS, 440, 3184. doi:10.1093/mnras/stu464

Bédard A., Bergeron P., Fontaine G., 2017, ApJ, 848, 11

Bédard A., Bergeron P., Brassard P., Fontaine G., 2020, ApJ, 901, 93

Ben-Ami S., et al., 2022, in den Herder J.-W. A., Nikzad S., Nakazawa K., eds, Society of Photo-Optical Instrumentation Engineers (SPIE) Conference Series Vol. 12181, Space Telescopes and Instrumentation 2022: Ultraviolet to Gamma Ray. p. 1218105 (arXiv:2208.00159), doi:10.1117/12.2629850

Bergeron P., Saffer R. A., Liebert J., 1992, ApJ, 394, 228. doi:10.1086/171575

Bergeron P., Saumon D., Wesemael F., 1995, ApJ, 443, 764. doi:10.1086/175566

Bergeron P., Wesemael F., Lamontagne R., Fontaine G., Saffer R. A., Allard N. F., 1995, ApJ, 449, 258. doi:10.1086/176053

Bergeron P., Ruiz M. T., Leggett S. K., 1997, ApJS, 108, 339. doi:10.1086/312955

Bergeron P., Leggett S. K., Ruiz M. T., 2001, ApJS, 133, 413. doi:10.1086/320356

Bergeron P., Fontaine G., Billères M., Boudreault S., Green E. M., 2004, ApJ, 600, 404. doi:10.1086/379808

Bergeron P., Dufour P., Fontaine G., Coutu S., Blouin S., Genest-Beaulieu C., Bédard A., Rolland B., 2019, ApJ, 876, 67

Bianchi L., 2011, Ap&SS, 335, 51. doi:10.1007/s10509-011-0612-2

Bianchi L., Shiao B., Thilker D., 2017, ApJS, 230, 24

Bohlin R. C., Dickinson M. E., Calzetti D., 2001, AJ, 122, 2118. doi:10.1086/323137

Bohlin R. C., Koester D., 2008, AJ, 135, 1092. doi:10.1088/0004-6256/135/3/1092

Bours M. C. P., Marsh T. R., Gänsicke B. T., Tauris T. M., Istrate A. G., Badenes C., Dhillon V. S., et al., 2015, MNRAS, 450, 3966. doi:10.1093/mnras/stv889

Bragaglia A., Renzini A., Bergeron P., 1995, ApJ, 443, 735. doi:10.1086/175564

Brown W. R., Kilic M., Gianninas A., 2017, ApJ, 839, 23. doi:10.3847/1538-4357/aa67e4

Camarota L., Holberg J. B., 2014, MNRAS, 438, 3111. doi:10.1093/mnras/stt2422

Cardelli J. A., Clayton G. C., Mathis J. S., 1989, IAUS, 135, 5

Carter P. J., et al., 2013, MNRAS, 429, 2143

Chandrasekhar S., 1931, ApJ, 74, 81. doi:10.1086/143324

Córsico A. H., Althaus L. G., Miller Bertolami M. M., Kepler S. O., 2019, A&ARv, 27, 7. doi:10.1007/s00159-019-0118-4

Croom S. M., Smith R. J., Boyle B. J., Shanks T., Loaring N. S., Miller L., Lewis I. J., 2001, MNRAS, 322, L29

Croom S. M., Smith R. J., Boyle B. J., Shanks T., Miller L., Outram P. J., Loaring N. S., 2004, MNRAS, 349, 1397

Dufour P., Blouin S., Coutu S., Fortin-Archambault M., Thibeault C., Bergeron P., Fontaine G., 2017, in Tremblay P. E., Gaensicke B., Marsh T., eds, Astronomical Society of the Pacific Conference Series Vol. 509, 20th European White Dwarf Workshop. p. 3 (arXiv:1610.00986)

Eisenstein D. J., et al., 2006, ApJS, 167, 40

Farihi J., Becklin E. E., Zuckerman B., 2005, ApJS, 161, 394. doi:10.1086/444362

Farihi J., Hoard D. W., Wachter S., 2010, ApJS, 190, 275

Farihi J., Gänsicke B. T., Steele P. R., Girven J., Burleigh M. R., Breedt E., Koester D., 2012, MNRAS, 421, 1635. doi:10.1111/j.1365-2966.2012.20421.x

Fitzpatrick E. L., 1999, PASP, 111, 63. doi:10.1086/316293

Fontaine G., Brassard P., Bergeron P., 2001, PASP, 113, 409. doi:10.1086/319535

Fontaine G., Brassard P., 2008, PASP, 120, 1043. doi:10.1086/592788

Foreman-Mackey D., Hogg D. W., Lang D., Goodman J., 2013, PASP, 125, 306. doi:10.1086/670067

Genest-Beaulieu C., Bergeron P., 2019, ApJ, 882, 106

Gentile Fusillo N. P., et al., 2015, MNRAS, 452, 765

Gentile Fusillo N. P., Gänsicke B. T., Farihi J., Koester D., Schreiber M. R., Pala A. F., 2017, MNRAS, 468, 971

Gentile Fusillo N. P., et al., 2019, MNRAS, 482, 4570

Gentile Fusillo N. P., et al., 2021, MNRAS, 504, 2707

Gentile Fusillo N. P., Tremblay P.-E., Cukanovaite E., Vorontseva A., Lallement R., Hollands M., Gänsicke B. T., et al., 2021, MNRAS, 508, 3877. doi:10.1093/mnras/stab2672

Gianninas A., Bergeron P., Ruiz M. T., 2011, ApJ, 743, 138

Green R. F., Liebert J., 1981, PASP, 93, 105

Harris H. C., et al., 2006, AJ, 131, 571

Holberg J. B., Bergeron P., 2006, AJ, 132, 1221. doi:10.1086/505938

Kawka A., Vennes S., Dupuis J., Chayer P., Lanz T., 2008, ApJ, 675, 1518. doi:10.1086/526411

Kepler S. O., et al., 2015, MNRAS, 446, 4078

Kepler S. O., et al., 2016, MNRAS, 455, 3413

Kilic M., Bergeron P., Kosakowski A., Brown W. R., Agüeros M. A., Blouin S., 2020, ApJ, 898, 84

Kilkenny D., Worters H. L., O'Donoghue D., Koen C., Koen T., Hambly N., MacGillivray H., Stobie R. S., 2016, MNRAS, 459, 4343

Kleinman S. J., et al., 2013, ApJS, 204, 5

Koester D., Voss B., Napiwotzki R., Christlieb N., Homeier D., Lisker T., Reimers D., et al., 2009, A&A, 505, 441. doi:10.1051/0004-6361/200912531

Koester D., Gänsicke B. T., Farihi J., 2014, A&A, 566, A34. doi:10.1051/0004-6361/201423691

Kong X., Luo A. L., Li X.-R., 2019, Research in Astronomy and Astrophysics, 19, 088

Korol V., Rossi E. M., Groot P. J., Nelemans G., Toonen S., Brown A. G. A., 2017, MNRAS, 470, 1894. doi:10.1093/mnras/stx1285

Korol V., Rossi E. M., Barausse E., 2019, MNRAS, 483, 5518. doi:10.1093/mnras/sty3440

Kowalski P. M., Saumon D., 2006, ApJL, 651, L137. doi:10.1086/509723

Kulkarni S. R., van Kerkwijk M. H., 2010, ApJ, 719, 1123. doi:10.1088/0004-637X/719/2/1123

Lajoie C.-P., Bergeron P., 2007, ApJ, 667, 1126. doi:10.1086/520926

Lallement R., Welsh B. Y., Vergely J. L., Crifo F., Sfeir D., 2003, A&A, 411, 447. doi:10.1051/0004-6361:20031214

Lamberts A., Blunt S., Littenberg T. B., Garrison-Kimmel S., Kupfer T., Sanderson R. E., 2019, MNRAS, 490, 5888. doi:10.1093/mnras/stz2834

Lawrence A., Warren S. J., Almaini O., Edge A. C., Hambly N. C., Jameson R. F., Lucas P., et al., 2007, MNRAS, 379, 1599. doi:10.1111/j.1365-2966.2007.12040.x

Liebert J., Dahn C. C., Monet D. G., 1988, ApJ, 332, 891. doi:10.1086/166699

Limoges M. M., Bergeron P., 2010, ApJ, 714, 1037

Limoges M. M., Bergeron P., Lépine S., 2015, ApJS, 219, 19

Magnier E. A., et al., 2013, ApJS, 205, 20

Manser C. J., et al., 2023, MNRAS,

Maoz D., Mazeh T., McQuillan A., 2015, MNRAS, 447, 1749. doi:10.1093/mnras/stu2577

Marsh T. R., Duck S. R., 1996, MNRAS, 278, 565

Marsh T. R., Gänsicke B. T., Steeghs D., Southworth J., Koester D., Harris V., Merry L., 2011, ApJ, 736, 95. doi:10.1088/0004-637X/736/2/95

Martin D. C., Fanson J., Schiminovich D., Morrissey P., Friedman P. G., Barlow T. A., Conrow T., et al., 2005, ApJL, 619, L1. doi:10.1086/426387

Martin D. C., GALEX Science Team, 2005, AAS

McCleery J., et al., 2020, MNRAS, 499, 1890

Mestel L., 1952, MNRAS, 112, 583. doi:10.1093/mnras/112.6.583

Mickaelian A. M., 2008, AJ, 136, 946

Morrissey P., GALEX Science Team, 2005, AAS

Morrissey P., Schiminovich D., Barlow T. A., Martin D. C., Blakkolb B., Conrow T., Cooke B., et al., 2005, ApJL, 619, L7. doi:10.1086/424734

Morrissey P., et al., 2007, ApJS, 173, 682

Napiwotzki R., et al., 2020, A&A, 638, A131

Nelemans G., Yungelson L. R., Portegies Zwart S. F., 2001, A&A, 375, 890. doi:10.1051/0004-6361:20010683

Nissanke S., Vallisneri M., Nelemans G., Prince T. A., 2012, ApJ, 758, 131. doi:10.1088/0004-637X/758/2/131

O'Donnell J. E., 1994, ApJ, 422, 158. doi:10.1086/173713

Press W. H., Flannery B. P., Teukolsky S. A., 1986, Numerical recipes. The art of scientific computing

Rebassa-Mansergas A., et al., 2016, MNRAS, 463, 1137

Rebassa-Mansergas A., Toonen S., Korol V., Torres S., 2019, MNRAS, 482, 3656

Redfield S., 2006, ASPC, 352, 79. doi:10.48550/arXiv.astro-ph/0601117

Reid I. N., 1996, AJ, 111, 2000. doi:10.1086/117936

Schlafly E. F., Finkbeiner D. P., 2011, ApJ, 737, 103. doi:10.1088/0004-637X/737/2/103

Schlegel D. J., Finkbeiner D. P., Davis M., 1998, ApJ, 500, 525. doi:10.1086/305772

Schmidt G. D., West S. C., Liebert J., Green R. F., Stockman H. S., 1986, ApJ, 309, 218

Stecher T. P., 1965, ApJ, 142, 1683. doi:10.1086/148462

Tremblay P. E., Bergeron P., Gianninas A., 2011, ApJ, 730, 128

Vanderburg A., Johnson J. A., Rappaport S., Bieryla A., Irwin J., Lewis J. A., Kipping D., et al., 2015, Natur, 526, 546. doi:10.1038/nature15527

Vanderburg A., Rappaport S. A., Xu S., Crossfield I. J. M., Becker J. C., Gary B., Murgas F., et al., 2020, Natur, 585, 363. doi:10.1038/s41586-020-2713-y

Vennes S., Smith R. J., Boyle B. J., Croom S. M., Kawka A., Shanks T., Miller L., Loaring N., 2002, MNRAS, 335, 673

Verbeek K., et al., 2012, MNRAS, 426, 1235

Vidrih S., et al., 2007, MNRAS, 382, 515

Vincent O., Bergeron P., Dufour P., 2023, arXiv, arXiv:2301.05209. doi:10.48550/arXiv.2301.05209

Wall R. E., Kilic M., Bergeron P., Rolland B., Genest-Beaulieu C., Gianninas A., 2019, MNRAS, 489, 5046

Wesemael F., Greenstein J. L., Liebert J., Lamontagne R., Fontaine G., Bergeron P., Glaspey J. W., 1993, PASP, 105, 761

Wheeler J. C., 2000, coca.book, 304

Winget D. E., Hansen C. J., Liebert J., van Horn H. M., Fontaine G., Nather R. E., Kepler S. O., et al., 1987, ApJL, 315, L77. doi:10.1086/184864

Winget D. E., Kepler S. O., 2008, ARA&A, 46, 157. doi:10.1146/annurev.astro.46.060407.145250

Yuan H. B., Liu X. W., Xiang M. S., 2013, MNRAS, 430, 2188. doi:10.1093/mnras/stt039